Smoothed Particle Hydrodynamic simulations of expanding HII regions

Thomas G. Bisbas

A Thesis submitted to
Cardiff University
for the degree of
Doctor of Philosophy

September 2009

Declaration

This work has not previously been accepted in substance for any degree and is not concurrently submitted in candidature for any degree.

Signed: _____
Candidate

Date: _____

Statement 1

This thesis is being submitted in partial fulfillment of the requirements for the degree of PhD.

Signed: _____
Candidate

Date: _____

Statement 2

This thesis is the result of my own independent work/investigation, except where otherwise stated. Other sources are acknowledged by explicit references.

Signed: _____
Candidate

Date: _____

Statement 3

hereby give consent for my thesis, if accepted, to be available for photocopying and for inter-library loan, and for the title and summary to be made available to outside organisations.

Signed: _____
Candidate

Date: _____

To my father

Acknowledgements

First and foremost, I would like to express my gratitude to my supervisor Anthony Whitworth for giving me the opportunity to implement this PhD Thesis and for guiding me through it during the past 4 years. I have to thank him for his patience in correcting the drafts of this thesis and for making useful comments on the language. His methodic work, excellent mathematical approach in problems of this Thesis, and good sense of humour have certainly helped me to finish the present work. Ant, thank you!

I would like to thank all my family for their love and support during the past 4 years. Especially I would like to thank my mother $\Xi\alpha\nu\vartheta\acute{\eta}$, and my father $\Gamma\iota\acute{\omega}\rho\gamma o\varsigma$ – to whom this Thesis is dedicated to. Without their support this Thesis would not have been possible. Many thanks go also to my sister $A\nu\nu\alpha$, and my brother $H\lambda\acute{\iota}\alpha\varsigma$.

I would like to acknowledge Richard Wünsch for his useful and helpful comments throughout this Thesis. Also, I would like to thank David Hubber for his assistance in performing the simulations of the present work, and to Andrew McLeod for debugging parts of the algorithm. Many thanks go to the rest of the members of the group and especially to Steffi Walch, and Dimitris Stamatellos. It was very pleasant to share my everyday time in the office with them. Richard, David, Andrew, Steffi, Dimitris, thank you all!

Last but not least, I would like to thank my flatmate $\Lambda\varepsilon\omega\nu\acute{\iota}\delta\alpha\varsigma$ for all the time I shared with him and all the useful not-just-scientific conversations we had during the last two years. Many thanks go also to all my friends Isabel, Pete, Vanessa, George, Sofia, and many others. The time I spent with them is unforgettable!

Abstract

This thesis deals with numerical simulations of expanding ionized regions, known as HII regions. We implement a new three dimensional algorithm in Smoothed Particle Hydrodynamics for including the dynamical effects of the interaction between ionizing radiation and the interstellar medium. This interaction plays a crucial role in star formation at all epochs.

We study the influence of ionizing radiation in spherically symmetric clouds. In particular, we study the spherically symmetric expansion of an HII region inside a uniform-density, non–self-gravitating cloud. We examine the ability of our algorithm to reproduce the known theoretical solution and we find that the agreement is very good. We also study the spherically symmetric expansion inside a uniform-density, self-gravitating cloud. We propose a new differential equation of motion for the expanding shell that includes the effects of gravity. Comparing its numerical solution with the simulations, we find that the equation predicts the position of the shell accurately.

We also study the expansion of an off-centre HII region inside a uniform-density, non–self-gravitating cloud. This results in an evolution known as the rocket effect, where the ionizing radiation pushes and accelerates the cloud away from the exciting star leading to its dispersal. During this evolution, cometary knots appear as a result of Rayleigh-Taylor and Vishniac instabilities. The knots are composed of a dense head with a conic tail behind them, a structure that points towards the ionizing source. Our simulations show that these knots are very reminiscent of the observed structures in planetary nebula, such as in the Helix nebula.

The last part of this thesis is dedicated to the study of cores ionized by an exciting source which is placed outside and far away from them. The evolution of these cores is known as radiation driven compression (or implosion). We perform simulations and compare our findings with results of other workers and we find that they agree very well. Using stable Bonnor-Ebert spheres, we extend our study to modelling triggered star formation within these cores as they are overrun and compressed by the incident ionizing flux. We construct a parameter space diagram and we map regions where star formation is expected to be observed.

All the above results indicate that the algorithm presented in this thesis works well for treating the propagation of ionizing radiation. This new algorithm provides the means to explore and evaluate the role of ionizing radiation in regulating the efficiency and statistics of star formation.

Statement

The simulations of the present Thesis are a result of collaboration between the members of the Star Formation group at Cardiff University. The author used the SEREN SPH code originally written by David Hubber, Chris Batty, and Andrew McLeod. The subroutine for the numerical treatment of the propagation of the ionizing radiation (fully described in Chapter 4) is a result of the authors own work.

Publications

Smoothed Particle Hydrodynamic simulations of expanding HII regions: I. Numerical Method and applications. T. G. Bisbas, R. Wünsch, A. P. Whitworth and D. A. Hubber, 2009, A&A, 497, 649.

Radiative transfer and the energy equation in SPH simulations of star formation. D. Stamatellos, A.P. Whitworth, T. Bisbas and S. Goodwin, 2007, A&A, 475, 37.

Talks

- September, 2009. The birth and influence of massive stars. CONSTELLATION Work Package 2 - Interim Meeting. Prague, Czech Republic. *SPH simulations of star formation triggered by expanding* HII *regions.*
- March, 2009. Observatoire de Paris. Paris, France. *SPH simulations of expanding* HII *regions.*
- February, 2009. University Observatory Munich. Munich, Germany. *SPH simulations of expanding* HII *regions.*
- January, 2009. Numerical Astrophysics and its role in Star formation. CONSTELLATION school. Cardiff, Wales, United Kingdom. *SPH simulations of expanding* HII *regions.*
- January, 2009. Aristotle University of Thessaloniki. Thessaloniki, Greece. *SPH simulations of expanding* HII *regions.*
- September, 2008. Astronomical Institute of the Academy of Sciences of the Czech Republic. Prague, Czech Republic. *SPH simulations of expanding* HII *regions.*
- August, 2008. Instituto Venezolano de Investigaciones Cientificas. Caracas, Venezuela. *SPH simulations of expanding* HII *regions.*

Poster

- December, 2007. Massive Stars as Cosmic Engines, Kauai, USA. *SPH simulations of star formation triggered by expanding* HII *regions.*

Contents

List of Figures

1 Introduction

Star formation is the field of Astronomy which examines the processes that result in the formation of a new star. One of these processes is the interaction between ionizing ultraviolet radiation and regions of neutral gas existing between stars. This thesis examines the physics and the evolution of this interaction, and studies its impact on star formation. In particular, a new three dimensional algorithm is presented for including the dynamical effects of ionizing radiation using Smoothed Particle Hydrodynamics. Several examples are shown of how the algorithm can be applied to problems involving this process, and how it can lead to star formation.

This chapter reviews the most important processes involved in the relation between star formation and ionized regions.

1.1 Interstellar medium and star formation

The gaseous matter that pervades the space between stars in our galaxy is called the *interstellar medium* (ISM). About 99% of this material is in the gas phase, while about 1% is dust. Hydrogen and helium are the two most abundant elements in the ISM. The remainder of it consists of other heavier elements, such as oxygen, carbon and nitrogen. A typical composition is $\sim 70\%$ hydrogen, $\sim 28\%$ helium and $\sim 2\%$ heavier elements. However, these numbers may change in different regions of our Galaxy. The density and temperature of the interstellar medium span many orders of magnitude and cause these elements to appear in many different forms, from molecular to ionized. This thesis only accounts for the chemical form of hydrogen, and in particular its

ionized form, so the discussion will be limited to this element. Molecular hydrogen exists in *giant molecular clouds* which are vast regions with temperatures $\sim 10-20\,\mathrm{K}$ and number densities $\sim 10^2-10^4\,\mathrm{cm}^{-3}$. The molecule of hydrogen cannot be detected directly as it is too cold to radiate at visible wavelengths, and is also difficult to be observed at infrared and radio wavelengths. Instead the presence of CO is used to determine its presence (Stahler & Palla 2005).

In regions with higher temperature, such as the *cold neutral medium* ($\sim 50-100\,\mathrm{K}$, $\sim 20-50\,\mathrm{cm}^{-3}$), or the *warm neutral medium* ($\gg 100\,\mathrm{K}$, $< 1\,\mathrm{cm}^{-3}$), hydrogen molecules tend to be dissociated and the hydrogen is mainly atomic. When a region of the interstellar medium is close to a source of ionization, it tends to be very hot ($\sim 10^4\,\mathrm{K}$) and ionized. These regions are commonly known as HII regions or more generally as *nebulae*. However, observational surveys show that the ISM contains even hotter and more rarefied regions ($> 10^6\,\mathrm{K}$, $\ll 1\,\mathrm{cm}^{-3}$), where metals are also highly ionized. These regions exist where supernova explosions occur, which in turn release huge amounts of energy.

The above properties of the ISM can be divided into categories of 'phases'. Pioneering work by Field et al. (1969), and later by McKee & Ostriker (1977), set the basis for describing these phases and defining the connection between them. In particular, McKee & Ostriker (1977) introduced the three-phase model where attention is drawn to the importance of supernova explosions. These are a dominant factor in balancing the energy of the interstellar medium and in determining the locations of different phases of the ISM. Based on this model, they conclude that $\sim 70\%$ of the volume of the interstellar medium is occupied by hot gas.

The interstellar medium is the birthplace of new stars. In general, a star is produced by the contraction of a dense core. The contraction begins when sufficiently dense regions become gravitationally unstable (Jeans 1902) creating the *protostar* or *young stellar object* (YSO). During its evolution to form a new star, the protostar passes through different phases (known as Class 0,I,II,III – for a review see André et al. 2000 and references therein), where an accretion disk of material forms around it and channels gas and dust onto the star. It is widely accepted that this process forms stars with masses up to $8\,\mathrm{M}_\odot$.

Stars with $M > 8\,\mathrm{M}_\odot$ emit large quantities of radiation (Krumholz & Bonnell, 2007). This radiation acts to prevent the infall of material and thus halts the accretion onto the massive protostar. At present, there is no consensus of the principle mode

of high-mass star formation. However, recently Krumholz et al. (2009) proposed that the radiation pressure of a massive star can escape through channels created by Rayleigh-Taylor and gravitational instabilities.

1.2 Categories of nebulae

Nebulae are regions consisting of ionized gas, particularly of hydrogen. The source of ionization is usually a single or multiple massive stars. Other sources, such as cosmic rays, can also ionize the interstellar medium but their interaction will not be included in the present thesis. Massive stars emit ultraviolet radiation with photons carrying more energy than the ionization potential of hydrogen (13.6 eV). When an ionizing photon interacts with a hydrogen atom, it is absorbed resulting in a free proton and a free electron. These photo-electrons may recombine with other free protons directly to the ground state creating a new energetic photon. This photon is able to ionize a nearby hydrogen atom diffusively. If a photo-electron does not recombine directly to the ground state, it cannot create a photon capable to ionize a hydrogen atom and is therefore lost.

A characteristic feature of all nebulae is that the temperature in the ionized gas tends to be much higher than the temparature in the surrounding neutral gas. These two gas states are separated by a thin slice known as the *ionization front*. In this slice, the temperature decreases abruptly. The difference between the temperatures of the hot ionized and cold neutral gas tends to result in pressure-driven expansion of the nebulae (Kahn 1954; Spitzer 1978). The ionization front moves initially at high supersonic speed relative to the sound speed in the neutral gas, and therefore it is preceded by a shock front which sweeps up a dense shell of neutral gas. The shell is bounded on its inside by the ionization front and on its outside by the *shock front*.

Nebulae can be divided into three categories (Osterbrock 1974) according to their origin and physical characteristics: a) diffuse nebulae, b) planetary nebulae, and c) supernova remnants.

1.2.1 DIFFUSE NEBULAE

Diffuse nebulae are extended regions of gas and dust where there are usually embedded stars. If these stars emit ultraviolet radiation, they ionize their surroundings creating HII regions. These HII regions are known as *emission nebulae*. Typical number densities in these regions are 10 to $10^2\,\mathrm{cm}^{-3}$, although they may span more orders of magnitude. If the embedded stars are very luminous but do not emit ionizing photons, then they illuminate the surrounding gas and dust creating a *reflection nebula*.

An emission nebula is a possible site of star formation as discussed in §1.3. A famous and well studied emission nebula is the Orion Nebula (M42 or NGC1976, see Fig. 1.1). In this high-mass star forming region, newly ionized gas found in the borders of the HII region flows into the main area of the nebula (Balick et al. 1974). The Orion Nebula Cluster is the closest massive star formation region to the Earth and is thus best studied. Recently, Menten et al. (2007) calculated this distance to be $414 \pm 7\,\mathrm{pc}$ using VLBA observations. This accurancy impact on a more detailed study on the luminosity and age profile of the young stars. They claim that most of the massive stars have already pass through the main sequence. In addition Gordon et al. (2000) using Chandra X-ray Observatory found ~ 1000 sources emitting X-rays. The mass sources span from $0.05\,\mathrm{M}_\odot - 50\,\mathrm{M}_\odot$, indicating that this area is the richest in X-rays ever observed.

1.2.2 PLANETARY NEBULAE

Planetary nebulae are formed during the latter evolutionary stages of a star with mass $1\,\mathrm{M}_\odot < M < 8\,\mathrm{M}_\odot$ (Salpeter 1971; Osterbrock 1974; Kwok et al. 1978; Schönberner 1981). The dying star expands and its outer parts are ejected into the interstellar medium. The remnant core, emits highly energetic radiation and ionizes this material. An expanding bubble is the result of this process (Balick 1987). Inside the ionized region of the bubble, a plethora of cometary knots exists, which are dense clumps surviving the strong ultraviolet radiation. The life time of such a nebula is of order of a few tens of thousand of years. One of the ongoing topics in studies of planetary nebulae is the origin of the wide range of their shapes (Balick & Frank 2002). Blackman et al. (2001) showed that a star on the symptotic giant branch is able to create a magnetic field in a dynamo located at the core-envelope interface.

Figure 1.1: The Orion Nebula is an expanding HII region and the birthplace of young stars. This high-mass star forming region is the closest to the Earth and is thus the best studied.

This magnetic field is strong enough to create bipolar or elliptical shapes, as they are widely observed.

The Helix nebula (NGC7293, see Fig. 1.2) is a well known and well studied planetary nebula (Leene & Pottasch 1987; Henry et al. 1999; Meaburn et al. 2005). At its centre there is a white dwarf, the remaining core of the initial star, which ionizes a spheroidal region around it. This region has a radius of $2.5 - 3\,\mathrm{pc}$ and contains thousands of photo-evaporating cometary knots (López-Martín et al. 2001). These knots consist of a dense head with an extended – relative to the size of the head – cometary tail. It has been suggested that their origin is due to instabilities in the expanding shock front, which are amplified by the ultraviolet radiation (O'Dell & Burkert 1996; O'Dell & Handron 1996; Meaburn et al. 1998; O'Dell et al. 2004). Hora et al. (2004) presented IRAC images and IRS spectra of the Helix nebula and

tis cometary knots. They found that the emission in these images is dominated by the rotational lines of H_2. Recently, Matsuura et al. (2009) presented high resolution images of the cometary knots showing their irregular structure.

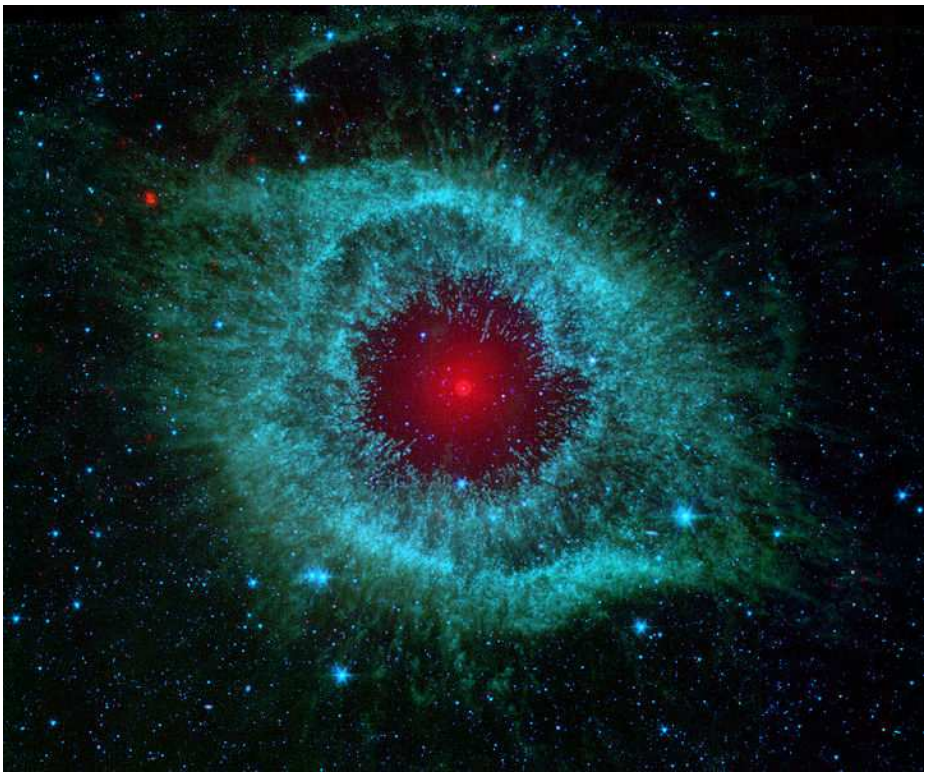

Figure 1.2: This image taken by the Spitzer Telescope shows the Helix Nebula. In the centre of this nebula a white dwarf exists, the remnant of the progenitor star core. Inside the ionized region, thousands of cometary knots are visible.

1.2.3 SUPERNOVAE REMNANTS

Supernovae remnants (SNR) are the remains of the explosion of a massive star (for a review see Weiler & Sramek 1988). When a massive star (with $M > 8\,M_\odot$) approaches its final stages of life, it ejects huge amounts of its initial material into the surrounding medium. This material is expanding at high speeds sweeping up the undisturbed interstellar gas and creating a strong shock front. They are extremely important for understanding the formation and evolution of our Galaxy. They heat up the interstellar medium, distribute heavy elements throughout the Galaxy, and accelerate cosmic rays.

Supernovae are divided into two main categories: type I and type II. Type I supernovae are characterized by sharp maxima in their light curves which die away gradually. This class can be subdivided into type Iα which exhibit a strong absorption line due to ionized silicon, and type Iβ which lack of this line. On the other hand, type II supernovae are distinguished from type I by the presence of hydrogen lines in their spectra. The mass of this progenitor should be at least $\sim 8\,\mathrm{M}_{\odot}$.

A famous SNR is the Crab Nebula (Fig. 1.3). This nebula is the remnant of a supernova explosion observed with the naked eye by Chinese and Arab astronomers in 1054 AD. The mass of the progenitor star is believed to have been about $M \sim 9 - 11\,\mathrm{M}_{\odot}$ (Davidson & Fesen 1985; MacAlpine & Satterfield 2008). At the centre of the Nebula there is a fast rotating pulsar, the remnant of the progenitor star (Burn 1973). The inner dynamics of the nebula has been recently studied by Hester et al. (2002) using Hubble Space Telescope and Chandra observations. In addition, Lyubarsky (2002) reported that the shock shape in this inner region is highly non-spherical because the energy flux in the pulsar wind decreases towards the axis. On the other hand, the overall structure of this nebula appears to be filamentary due to the Rayleigh-Taylor instability (Hester et al. 1996a).

1.3 Star formation triggered by expanding Hii regions

The influence of ionizing photons emitted by a massive star, or by a small group of massive stars, in the interstellar medium is of great interest. Many past and recent observations show that Hii regions are the birthplace of stars. Elmegreen (1998) reviews the basic mechanisms that trigger star formation, which include cloud collisions and interaction of the neutral material with expanding Hii regions. Deharveng et al. (2005) emphasize the importance of Hii regions in triggering star formation and summarize possible processes in this regard. In addition, Hester & Desch (2005) propose an evolutionary scenario of low mass star formation in an ionized environment providing evidence that our own solar system was formed in the vicinity of a massive star. It is interesting to note that it is impossible just by observing the star forming region to claim if the stars have been triggered or not.

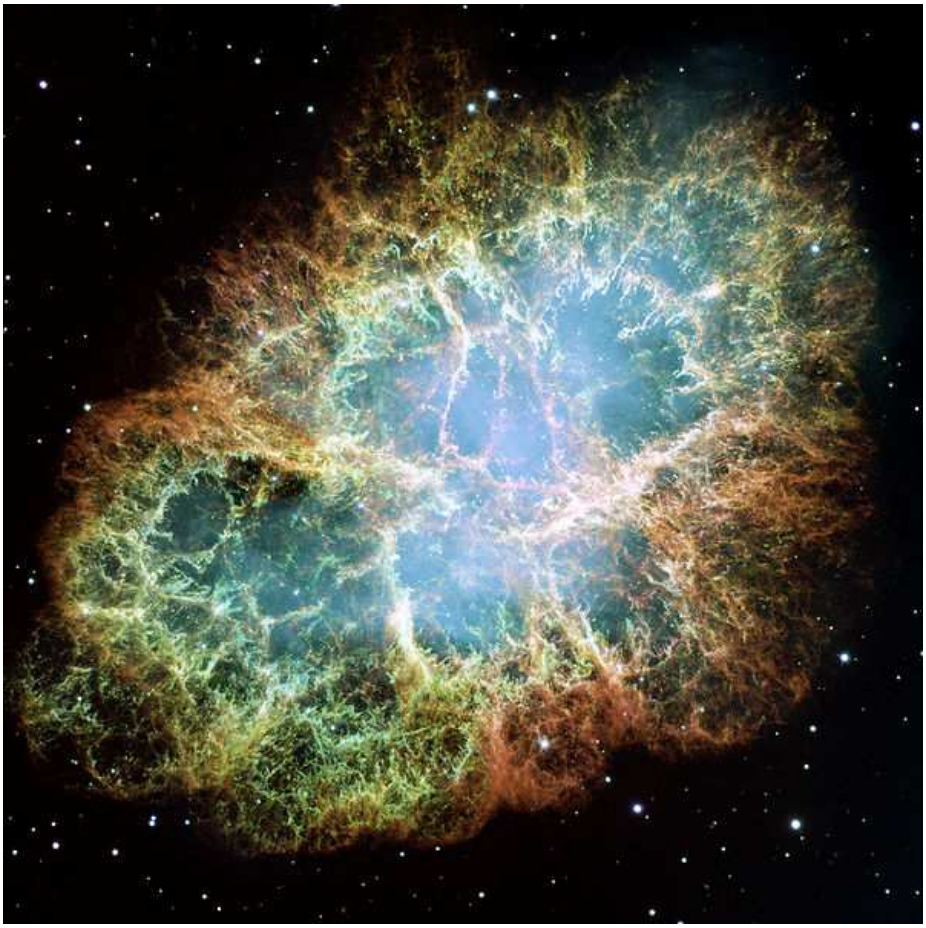

Figure 1.3: The Crab Nebula. The remnant of a supernova explosion observed in 1054 AD. In the heart of the nebula is a pulsar. It has a strong magnetic field and rotates extremely fast. The filamentary structure is the result of Rayleigh-Taylor instability.

Three of the most dominant mechanisms widely believed to be responsible for triggering star formation in HII regions will be presented in this section.

1.3.1 PRE-EXISTING NEUTRAL CLUMPS INSIDE AN HII REGION

The structure of the interstellar medium is observed to be extremely irregular and to contain many clouds. As an HII region expands, it may overrun and compress pre-existing nearby clouds, causing them to collapse. As they contract, their internal thermal pressure increases and this may lead to re-expansion. After the re-expansion, a cometary tail is formed pointing away from the exciting star (see Fig. 1.4). In the head of the cometary structure there is a dense region which, if sufficiently dense, forms stars. These structures are known as *cometary globules*, around which a *bright*

rim of ionized gas exists. This mechanism is called *Radiation Driven Compression*[1] (RDC).

Various observations prove the existence of these cometary globules as well as the fact that they are potential sites of star formation. Sugitani et al. (1999) examined 89 bright-rimmed clouds and revealed that 44 of them are associated with small young clusters or aggregations. Lefloch & Lazareff (1995) report observations of CG7S, a globule undergoing the first stages of collapse and cometary tail formation. In addition, Lefloch et al. (1997) argue that in the cometary globule CG5 there is evidence of star formation triggered by the Hii region IC1848. Recently, Morgan et al. (2008) examined 44 bright rimmed clouds with a view to determining their evolutionary state. Using submillimetre observations they found that 42 dense cores are embedded in these clouds and that they host star formation.

Several workers have tried to simulate the RDC mechanism. Some of these simulations (Sandford et al. 1982; Bertoldi 1989; Lefloch & Lazareff 1994; Miao et al. 2006; Henney et al. 2008) concentrate on the morphology of the resulting bright-rimmed clouds. In contrast, Peters et al. (2008) address the possibility that the flow of ionized gas off an irradiated cloud might be an important source of turbulence; and Kessel-Deynet & Burkert (2003), Dale et al. (2005), Gritschneder et al. (2009), and Miao et al. (2009) explore the possibility that the collapse of a bright-rimmed cloud might sometimes lead to triggered star formation. These simulations show that it is possible to reproduce the observed morphologies of bright-rimmed cloud. However, the evolution of bright-rimmed clouds and the role of expanding Hii regions in triggering star formation, are still poorly understood. For example, Dale et al. (2007) argue that the main effect of an expanding Hii region may simply be to expose stars that would have formed anyway.

1.3.2 Pre-existing dense clumps in the neutral gas

Suppose there is a dense clump embedded in a region consisting of neutral gas and that an exciting star is placed nearby emitting ionizing photons. The ionizing photons penetrate the dense area more slowly than its surroundings. As the ionization front overruns a dense region, a conic cometary tail develops, pointing away from

[1]It may also be referred to in the literature as "Radiation Driven Implosion" (RDI)

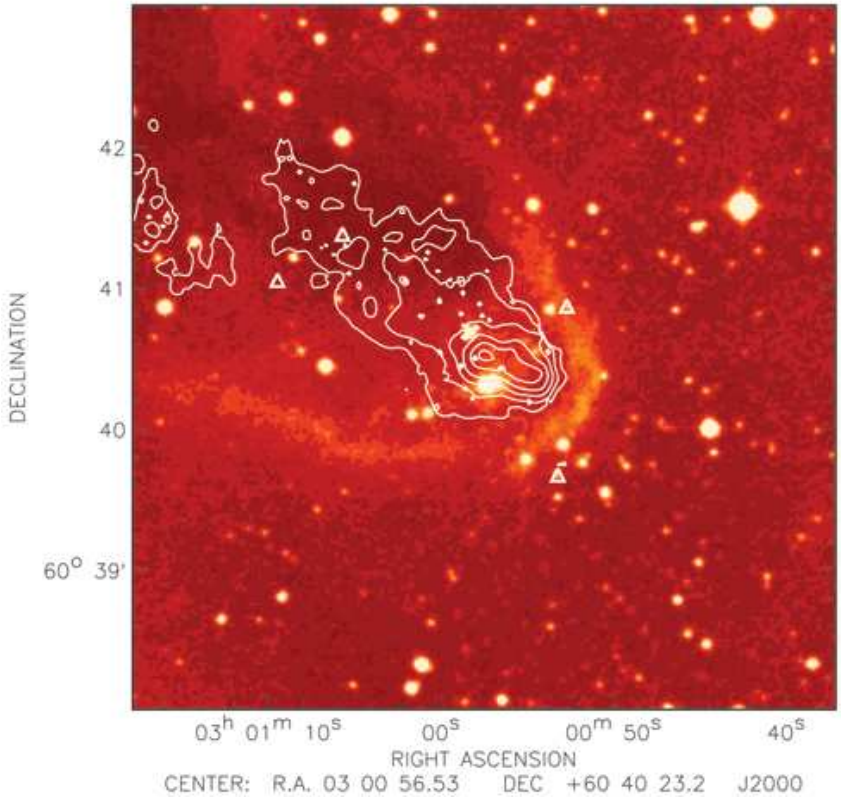

Figure 1.4: This figure shows a SCUBA observation of a bright rimmed cloud (taken from Morgan et al. 2008). The wavelength is 850μm and contours start at 6σ and increase in increments of 20% of the peak flux. Triangles indicate sources that have been identified as young stellar objects (YSOs).

the ionizing star, as a result of shadowing behind the clump. This structure is commonly referred to in the literature as an *elephant's trunk*, and the dense clump as an *Evaporating Gaseous Globule* (EGG). If it is sufficiently dense, an EGG can be the birthplace of an YSO. Hester et al. (1996b) were the first to report the existence of EGGs. While observing the Eagle Nebula (M16 or NGC6611), they discovered a population of EGGs associated with YSOs. Various observations followed (i.e. McCaughrean & Andersen 2002; Linsky et al. 2007; Indebetouw et al. 2007) providing clear evidence of star formation in the EGGs of the Eagle Nebula. In addition, Whitworth & Zinnecker (2004) conclude that in the central regions of large clusters, free-floating brown dwarfs and planetary-mass objects may form when more massive pre-existing cores are overrun by HII regions.

The cometary tail is eroded from its sides due to the diffuse radiation of the HII region. If the EGG is sufficiently dense (which is likely the case if it contains an

YSO), it will become detached from the rest of the elephant trunk and survive well embedded in the HII region. These objects are known as *proplyds* (abbreviation of "proto-planetary disks"), and are best seen in the Orion Nebula (O'Dell et al. 1993). De Marco et al. (2006) analyzed images of the Hubble Space Telescope and found proplyds in various other HII regions, although only a small fraction of them contains a new star. Figure 1.5 shows the evolutionary sequence of the above scenario.

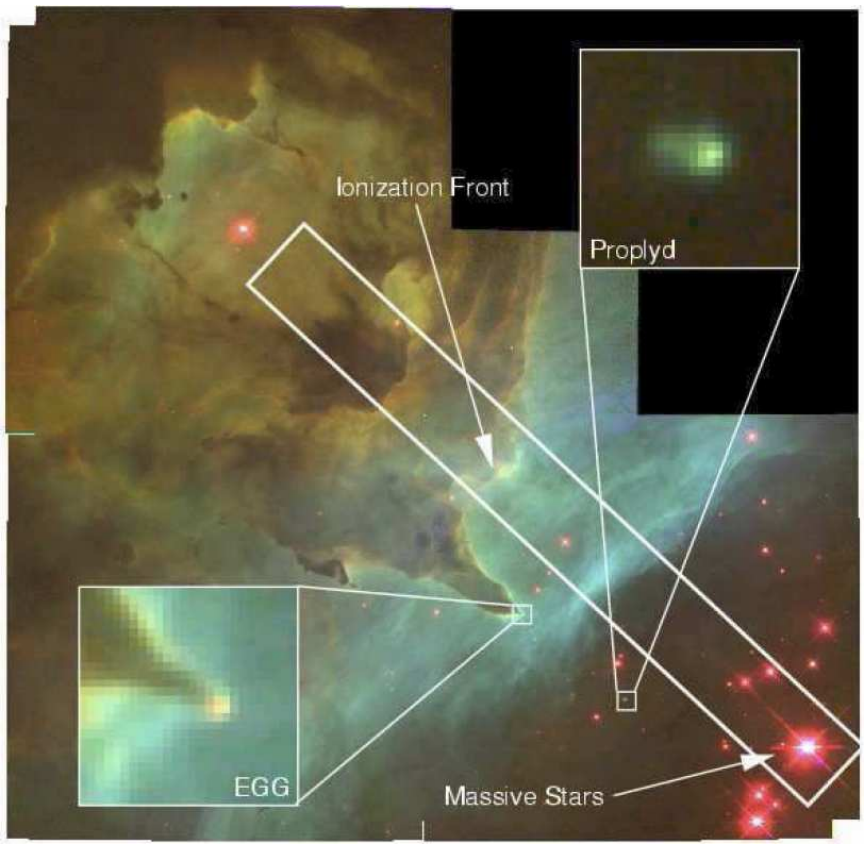

Figure 1.5: In this Hubble Space Telescope figure of NGC 6357, we see almost the entire evolutionary sequence described in §1.3.2 (image taken from Hester & Desch 2005). Massive stars emit ultraviolet radiation which causes the HII region to expand. During the expansion, the ionization front may overrun dense regions which protude into the interior of the ionized region creating elephant trunks. In the heads of these elephant trunks, EGGs exist and if they are sufficiently dense, they are detached creating the proplyds, where stars are likely to form.

1.3.3 Expanding dense shells

A spherically symmetric expanding HII region is surrounded by a dense shell, bounded on its inner edge by the ionization front and on its outer edge by a shock front. As

the shell sweeps up neutral material during its expansion, its surface density increases with time. It is therefore likely to be prone to gravitational instability (e.g. Elmegreen 1994). This may trigger fragmentation and if the fragments become sufficiently dense they can form stars. This mode of star formation is usually referred to as the *collect and collapse* mechanism, first proposed by Elmegreen & Lada (1977) and later on studied by Whitworth et al. (1994a,b) and others.

There are various other observations showing that the collect and collapse mechanism appears to be operating. Deharveng et al. (2005) proposed seventeen candidate regions where massive fragments are regularly spaced along the ionization front, as the mechanism predicts. In addition, Zavagno et al. (2006) examined the expanding HII region RCW 79 (see Fig. 1.6) and they found that the massive star formation observed in the borders of this region has been triggered by the expansion of the HII region. Recently, Deharveng et al. (2008) studied the star formation in the periphery of Sh212 and found strong evidence for the collect and collapse mechanism.

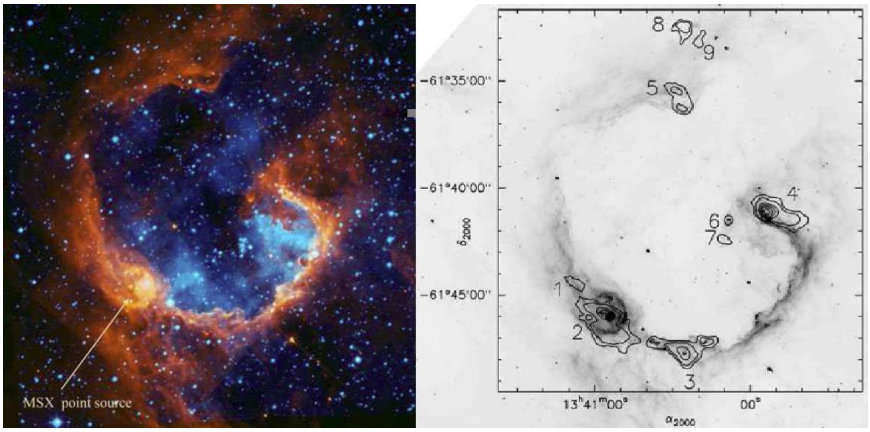

Figure 1.6: This figure (taken from Zavagno et al. 2006) shows an image of the RCW 79 region (left) and a map (right) of 9 dense fragments of the shock front. The collect and collapse mechanism can explain their existence.

1.4 PLAN OF THE THESIS

This thesis is organized as follows.

In Chapter 2, a brief overview of the physics behind HII regions is given. The expansion of a spherical symmetric HII region is analyzed and a new semi-analytical

approximation for the propagation of the shock front is presented. A short discussion of the most dominant hydrodynamical instabilities observed in an expanding HII region closes this chapter.

In Chapter 3, the fundamentals of Smoothed Particle Hydrodynamics are discussed and the basic equations that regulate this numerical method are described.

In Chapter 4, the new three dimensional algorithm which treats the ionizing radiation is presented. It is shown how this algorithm creates rays emanating from the ionizing star along which the photons propagate and how the position of the ionization front is located at the boundary of the HII region.

In Chapter 5, test applications are presented to compare the results of this new algorithm with the theoretical predictions of Chapter 2. In particular, convergence tests are performed and examples of expanding HII regions in a uniform density spherical cloud are shown

In Chapter 6, technical tests are presented in order to see how numerical noise affects the evolution of the physical quantities of a clump ionized by an external source. These tests are performed in order to explore the capabilities of the new algorithm in modelling triggered star formation in the radiation driven compression mechanism. In addition, the properties of Bonnor-Ebert spheres and the barotropic equation of state are discussed.

In Chapter 7, we present various astrophysical simulations. These include expansion of an HII region in a fractal medium, and an off-centre expansion in a uniform-density spherical cloud. A particular attention is drawn on the Radiation Driven Compression mechanism where we examine physical parameters to see when these cores form stars triggered by the incident ionizing flux.

In Chapter 8, the main conclusions of the present thesis and the capabilities of the algorithm are summarized. Possible future simulations of expanding HII regions and associated star formation are discussed.

2 The Physics of HII regions

In this chapter we discuss the basic physics that regulates HII *regions. We begin by describing the typical properties of neutral interstellar gas before it is ionized (§2.1) as well as the ionization equilibrium (§2.2) inside an* HII *region. Once an* HII *region is fully ionized, it will expand due to the pressure difference between the hot ionized gas and the surrounding cold neutral gas. (§2.3). We close this chapter with a brief discussion of Vishniac (§2.4.1) and Rayleigh-Taylor (§2.4.2) instabilities, which are important in understanding the fragmentation of the dense shells swept up by expanding* HII *regions.*

2.1 THERMODYNAMICS

Let us suppose that there is a cosmic gas which consists of a fraction X of hydrogen (by mass) and Y of helium. At a fixed density, as the temperature increases, the molecular hydrogen (H_2) dissociates producing atomic hydrogen (HI), according to the reaction:

$$H_2 \longrightarrow 2HI - 4.5(eV) \tag{2.1}$$

At higher temperatures, HI is ionized according to:

$$HI \longrightarrow HII + e^- - 13.6(eV) \tag{2.2}$$

We do not consider the ionization balance of helium, but we do consider its contribution to the molecular weight, on the assumption that it is not ionized. The mean molecular weight μ is therefore given by (Black & Bodenheimer 1975):

$$\mu^{-1} = (1 + y + 2xy) \cdot \frac{X}{2} + \frac{Y}{4} \tag{2.3}$$

where y is the degree of dissociation of H_2 and x is the degree of ionization of H_I.

The isothermal sound speed is given by

$$c = \sqrt{\frac{k_B T}{\mu m_p}} \tag{2.4}$$

where k_B is the Boltzmann constant ($k_B \simeq 1.38 \times 10^{-16}\,\mathrm{g\,cm^2\,s^{-2}\,K^{-1}}$), T is the temperature of the gas, and m_p is the mass of the proton ($m_p \simeq 1.67 \times 10^{-24}\,\mathrm{g}$).

Example

A typical cosmic gas consists of $X = 0.7$ of molecular hydrogen (by mass) and $Y = 0.3$ of helium. The typical temperature for the interstellar molecular hydrogen is $T_n = 10\,\mathrm{K}$. Since in this phase $x = y = 0$, from Eqn.(2.3) the mean molecular weight is $\mu_n = 2.35$ and from Eqn.(2.4) the isothermal sound speed is $c_n = 0.187\,\mathrm{km\,s^{-1}}$.

On the other hand in the ionized phase we have $x = y = 1$, so $\mu_i = 0.678$. The temperature here is $T_i = 10^4\,\mathrm{K}$ so the sound speed is $c_i = 11\,\mathrm{km\,s^{-1}}$.

Below is a summary of the variables for the mean molecular weight and sound speed for different fractions of hydrogen and helium.

X	Y	$\mu_{\rm i}$	$c_{\rm i}$ [km/s]	$\mu_{\rm n}$	$c_{\rm n}$ [km/s]
1	0	0.5	12.8	1	0.2
0.7	0.3	0.678	11	2.35	0.19

2.2 THE PHOTOIONIZATION EQUATION

Consider an arbitrary density field $\rho(\mathbf{r})$ of neutral hydrogen. The corresponding number density of hydrogen nuclei in all forms is $n(\mathbf{r}) = \frac{X}{m_p}\rho(\mathbf{r})$. Suppose now that we switch on a star emitting Lyman continuum photons. The position of the star defines the centre of the coordinate system. The photons ionize the neutral medium producing $n_{\rm e}$ electrons and $n_{\rm p}$ protons. Since we are neglecting ionization of helium, we have $n_{\rm e} = n_{\rm p}$.

When the hydrogen is ionized, protons and electrons may recombine directly to the ground state. This procedure creates a photon which is able to ionize a nearby hydrogen atom. In order not to have to follow this diffuse component of the ionizing radiation, we invoke the *on-the-spot* (OTS) approximation (Osterbrock 1974) and use the recombination coefficient into excited stages only, $\alpha_{\rm B}$. The OTS assumes that the gas is ionized directly from the star at all times.

The recombination coefficient $\alpha_{\rm B}$ is given by

$$\alpha_{\rm B} \simeq 2.7 \times 10^{-10}\,{\rm cm}^3\,{\rm s}^{-1} \left(\frac{T_{\rm i}}{\rm K}\right)^{-3/4}. \tag{2.5}$$

where $T_{\rm i}$ is the temperature of the ionized hydrogen.

The recombination rate per unit volume is $\alpha_{\rm B} n_{\rm e} n_{\rm p}$, and assuming that inside the HII region the hydrogen is fully ionized, $\alpha_{\rm B} n_{\rm e} n_{\rm p} = \frac{\alpha_{\rm B}\rho(\mathbf{r})^2}{m^2}$, where $m = m_{\rm p}/X$. The mass m represents the mass associated with a hydrogen atom when account is taken of the contribution of helium.

Consider the element of volume defined by the infinitesimal solid angle $d^2\Omega$ about the unit vector $\hat{\mathbf{k}}$ (as seen from the star) and the infinitesimal range of radii $(r,\, r + dr)$,

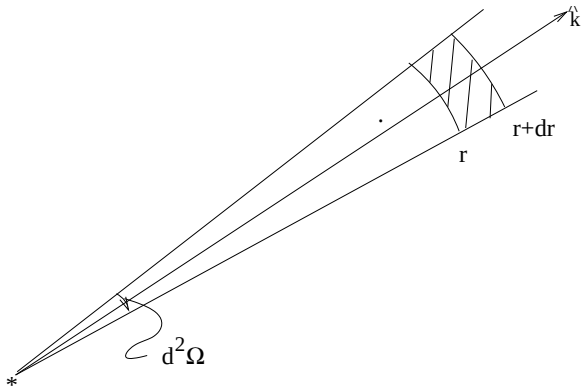

Figure 2.1: This figure shows the cone of solid angle $d^2\Omega$ through which the ionizing photons propagate. The shaded layer is the volume $r^2 d^2\Omega dr$.

as measured from the star. If the number flux of ionizing photons in the direction $\hat{\mathbf{k}}$ is $\dot{N}(r)$, then the equation of ionization balance gives

$$\dot{N}(r)r^2 d^2\Omega = \frac{\alpha_{\rm B}\rho^2(\mathbf{r})}{m^2} r^2 d^2\Omega dr + \dot{N}(r+dr)(r+dr)^2 d^2\Omega\,, \tag{2.6}$$

or if we cancel $d^2\Omega$,

$$\dot{N}(r)r^2 = \frac{\alpha_{\rm B}\rho^2(\mathbf{r})}{m^2} r^2 dr + \dot{N}(r+dr)(r+dr)^2\,. \tag{2.7}$$

From the above equation we obtain

$$\dot{N}(r+dr)(r+dr)^2 - \dot{N}(r)r^2 = -\frac{\alpha_{\rm B}\rho^2(\mathbf{r})}{m^2} r^2 dr\,. \tag{2.8}$$

The lefthand side of the above equation is $\dot{N}(r+dr)(r+dr)^2 - \dot{N}(r)r^2 = \frac{d}{dr}\left\{\dot{N}(r)r^2\right\} dr$, so if we replace the latter in Eqn.(2.8) we obtain

$$\frac{d}{dr}\left\{\dot{N}(r)r^2\right\} dr = -\frac{\alpha_{\rm B}\rho^2(\mathbf{r})}{m^2} r^2 dr\,. \tag{2.9}$$

If we cancel dr from both sides and integrate we obtain

$$\dot{N}(r)r^2 = \frac{\dot{\mathcal{N}}_{\rm LyC}}{4\pi} - \frac{\alpha_{\rm B}}{m^2}\int_{r'=0}^{r'=r} \rho(\mathbf{r}')^2 r'^2 dr'\,, \tag{2.10}$$

where $\frac{\dot{\mathcal{N}}_{\rm LyC}}{4\pi}$ is the constant of integration, and $\dot{\mathcal{N}}_{\rm LyC}$ is the total emission rate of the star. Equation 2.10 describes the photoionization equilibrium inside an HII region.

Let us consider $R_{\rm IF}$ to be the position of the ionization front (IF), where the flux of the arriving ionizing photons is zero ($\dot{N}_{\rm tot}(R_{\rm IF}) = 0$). The ionization front is the moving edge of the Hii region. Then Eqn.(2.10) is

$$\int_{r=0}^{r=R_{\rm IF}} \rho(\mathbf{r})^2 r^2 dr = \frac{\dot{\mathcal{N}}_{\rm LyC} m^2}{4\pi\alpha_{\rm B}} \,. \tag{2.11}$$

where we have made the assumption that the material inside the Hii region is fully ionized. If the density field is uniform ($\rho(\mathbf{r}) = \rho_{\rm o}$) then Eqn.(2.11) becomes $\frac{\rho_{\rm o}^2 R_{\rm IF}^3}{3} = \frac{\dot{\mathcal{N}}_{\rm LyC} m^2}{4\pi\alpha_{\rm B}}$ and so the resultant Hii region is spherical with radius

$$R_{\rm St} \equiv R_{\rm IF} \;\; = \;\; \left(\frac{3\dot{\mathcal{N}}_{\rm LyC} m^2}{4\pi\alpha_{\rm B}\rho_{\rm o}^2} \right)^{1/3} \tag{2.12}$$

where $R_{\rm St}$ is the Strømgren radius.

Strømgren (1939) was the first to show that the transition from a state of almost completely ionized material to a state of almost completely neutral material occurs in a very short distance compared with the dimensions of the Hii region. Thus we may treat the front as a sharp discontinuity. The distance over which the degree of ionization changes from 90 % to 10 % is given by

$$\Delta R_{\rm St} \;\; \simeq \;\; \frac{20\, m}{\rho_{\rm o}\, \bar{\sigma}} \simeq 2 \times 10^{-4}\,{\rm pc} \left(\frac{\rho_{\rm o}}{10^{-20}\,{\rm g\,cm^{-3}}} \right)^{-1} \tag{2.13}$$

(Whitworth 2000). Here $\bar{\sigma} = 7 \times 10^{-18}\,{\rm cm}^2$ is the mean photoionization cross section presented by a hydrogen atom to Lyman continuum photons from an OB star.

2.3 Expansion of an Hii region

Kahn (1954) was the first to study the propagation of an ionization front into a neutral medium when an ionizing star suddenly switches on. At early times most of the Lyman continuum photons ionize additional gas beyond the instantaneous position of the ionization front. Thus the Hii region expands rapidly at highly supersonic speed. In this first phase the ionization front is called "R-type" (R=Rarefied) and is terminated once the ionization front reaches the Strømgren radius, creating the

Strømgren sphere. The timescale for this first phase is of order

$$\frac{m}{\alpha_{\rm B}\rho_{\rm o}} \simeq 30\,{\rm yrs}\left(\frac{\rho_{\rm o}}{10^{-20}\,{\rm g\,cm^{-3}}}\right)^{-1}. \tag{2.14}$$

The newly formed HII region has temperature $T_{\rm i} \simeq 10^4\,{\rm K}$, whereas the surrounding neutral region has $T_{\rm n} \simeq 10\,{\rm K}$. This in turn results in large difference in thermal pressure, and the HII region expands. In this second phase the ionization front is called "D-type" (D=Dense) and it propagates at subsonic speed relative to the ionized gas, but supersonic speed relative to the neutral gas, creating a dense shock front ahead of it.

This thesis is concerned with the role played by this shock front in triggering star formation. Since we simulate the D-type expansion of the HII region, our discussion will be limited to this second phase.

2.3.1 THE SPITZER SOLUTION

The thermal pressure $P_{\rm i}(t)$ of the ionized gas in an expanding HII region is

$$P_{\rm i}(t) = \rho_{\rm i}(t)c_{\rm i}^2\,. \tag{2.15}$$

This matches approximately with the thermal pressure $P_{\rm n}(t)$ of the neutral gas in the shell between the ionization front and the shock front. The pressure of the neutral gas in the shell is equal to the ram pressure of the undisturbed neutral gas as it is swept up by the shock front (see Fig. 2.2). From Spitzer (1978)[1] $P_{\rm n}(t)$ is given by

$$P_{\rm n}(t) = \rho_{\rm o}\left(\frac{dR_{\rm IF}(t)}{dt}\right)^2, \tag{2.16}$$

where $\rho_{\rm o}$ is the density of the undisturbed neutral gas, $R_{\rm IF}(t)$ is the function describing the position of the ionization front in time, and $dR_{\rm IF}(t)/dt$ describes the velocity of propagation of the ionization front.

[1]It is recommended for the reader to see also Shu (1992) and Appendix F of Stahler & Palla (2005)

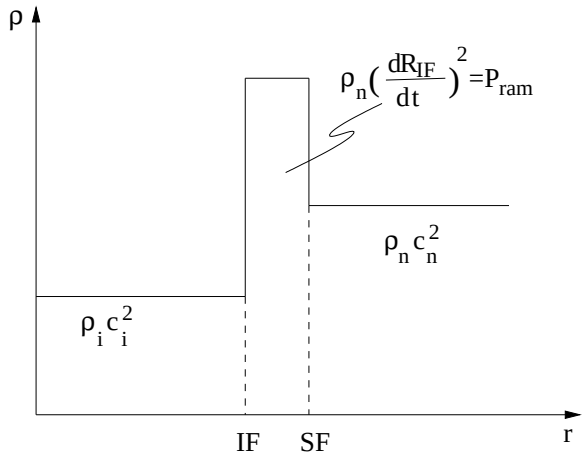

Figure 2.2: This figure shows the density profile of an HII region versus the distance from the star. The pressure of the shell is equal to the thermal pressure of the ionized gas and equal to the ram pressure of the undisturbed neutral gas.

Using Eqn.(2.12), at t the radius of the HII region is

$$R_{\rm IF}(t) = \left(\frac{3\dot{\mathcal{N}}_{\rm LyC} m^2}{4\pi\alpha_{\rm B}\rho_{\rm i}(t)^2} \right)^{1/3} \tag{2.17}$$

or

$$\rho_{\rm i}(t) = \left(\frac{3\dot{\mathcal{N}}_{\rm LyC} m^2}{4\pi\alpha_{\rm B} R_{\rm IF}(t)^3} \right)^{1/2} . \tag{2.18}$$

Combining Eqn.(2.15) & Eqn.(2.16) and using Eqn.(2.18) we obtain

$$\begin{aligned} \rho_{\rm o} \left(\frac{dR_{\rm IF}(t)}{dt} \right)^2 &= \left(\frac{3\dot{\mathcal{N}}_{\rm LyC} m^2}{4\pi\alpha_{\rm B} R_{\rm IF}(t)^3} \right) c_{\rm i}^2 \Rightarrow \\ \Rightarrow \frac{dR_{\rm IF}(t)}{dt} &= \left(\frac{R_{\rm St}}{R_{\rm IF}(t)} \right)^{3/4} c_{\rm i} \end{aligned} \tag{2.19}$$

At $t = 0 \Rightarrow R_{\rm IF}(0) = R_{\rm St}$, so

$$\int_{R_{\rm St}}^{R_{\rm IF}(t)} R_{\rm IF}^{3/4} dR_{\rm IF} = R_{\rm St}^{3/4} c_{\rm i} \int_0^t dt \tag{2.20}$$

and therefore

$$R_{\rm IF}(t) \;=\; R_{\rm St}\left(1+\frac{7}{4}\frac{c_{\rm i}t}{R_{\rm St}}\right)^{4/7}. \tag{2.21}$$

Eqn.(2.21) is known as the "Spitzer solution" (Spitzer 1978). Thus the velocity of propagation $V_{\rm IF}(t)$ of the ionization front is

$$V_{\rm IF}(t) = c_{\rm i}\left(1+\frac{7}{4}\frac{c_{\rm i}t}{R_{St}}\right)^{-3/7}; \tag{2.22}$$

the density of the ionized gas is

$$\rho_{\rm i} = \rho_{\rm o}\left(1+\frac{7}{4}\frac{c_{\rm i}t}{R_{\rm St}}\right)^{-6/7}; \tag{2.23}$$

and the mass of ionized gas is

$$M_{\rm i}(t) \;=\; \frac{m^2\,\dot{\mathcal{N}}_{\rm LyC}}{\alpha_{\rm B}\,\rho_{\rm o}}\left(1+\frac{7}{4}\frac{c_{\rm i}t}{R_{\rm St}}\right)^{6/7}. \tag{2.24}$$

Figure 2.3 shows a graphical display of the last four equations.

2.3.2 SEMI-ANALYTIC APPROXIMATION

We will now attempt to solve the equation of motion of the accreting thin shell accelerated by the thermal pressure of the HII region (Hosokawa & Inutsuka 2006). This approach includes the effects of gravity and is therefore of more general nature.

The equation of motion of the shell of mass $M_{\rm sh}$ and radius $R_{\rm sh}$ is

$$\frac{d}{dt}(M_{\rm sh}\dot{R}_{\rm sh}) = 4\pi R_{\rm sh}^2 P_{\rm i} - \frac{GM_{\rm sh}M_{\rm i}}{R_{\rm sh}^2} - \frac{GM_{\rm sh}^2}{2R_{\rm sh}^2} \tag{2.25}$$

where $P_{\rm i} = \rho_{\rm i}c_{\rm i}^2$, $M_{\rm i} = (4\pi R_{\rm sh}^3\rho_{\rm i})/3$ and $\rho_{\rm i} = \left(\frac{3m^2\dot{\mathcal{N}}_{\rm LyC}}{4\pi\alpha_{\rm B}R_{\rm sh}^3}\right)^{1/2}$ are the pressure, the mass and the density of the ionized gas, respectively. The second term on the right hand side represents the gravitational force due to the HII region mass, and the third term is the average gravitational force acting on the shell due to its own mass (it is zero at its inner edge and $GM_{\rm sh}^2/R_{\rm sh}^2$ at the outer one; see Whitworth & Francis 2002).

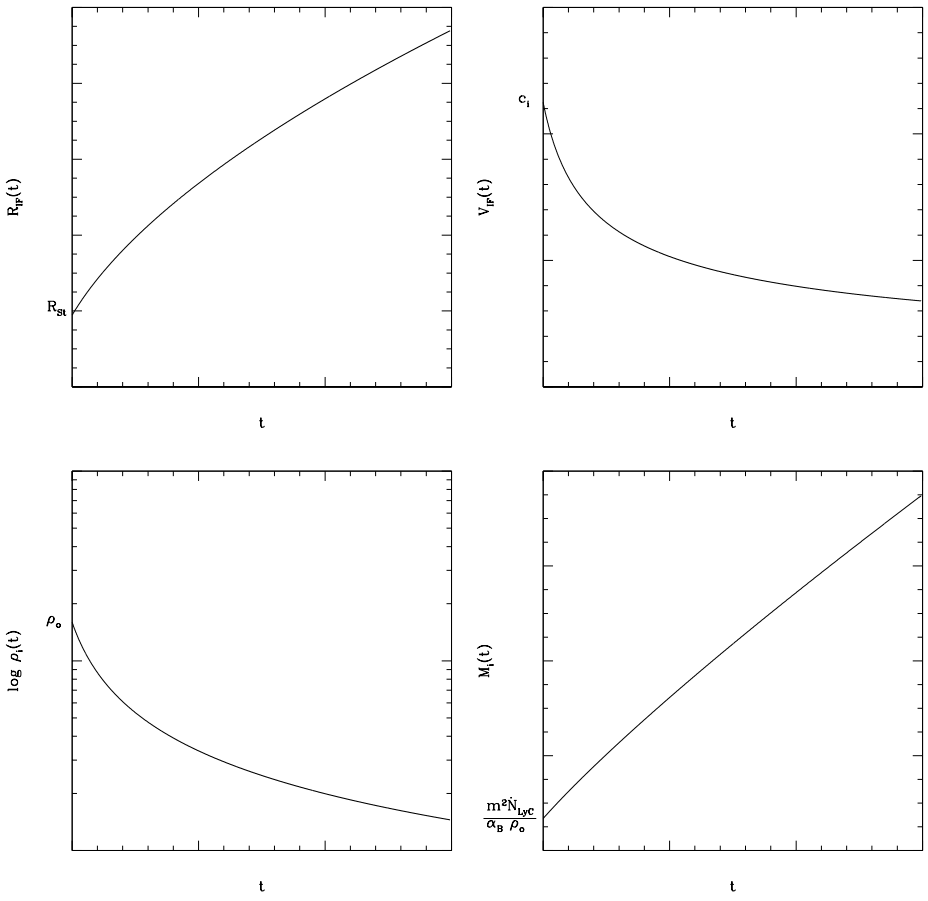

Figure 2.3: This figure shows the evolution in time for the position of ionization front (top left), the speed at which the ionization front propagates (top right), the density of the ionized gas (bottom left) and the mass of the ionized gas (bottom right).

The mass of the shell is the difference between the mass of the original neutral gas which occupies the sphere of radius $R_{\rm sh}$ and the mass of the Hii region

$$M_{\rm sh} = \frac{4\pi}{3} R_{\rm sh}^3 (\rho_{\rm o} - \rho_{\rm i}) \ . \tag{2.26}$$

Inserting (2.26) into (2.25) and using Eqn.(2.12) we obtain

$$\begin{aligned} \ddot{R}_{\rm sh}(R_{\rm sh}^3 - R_{\rm St}^{3/2} R_{\rm sh}^{3/2}) + 3\dot{R}_{\rm sh}^2 (R_{\rm sh}^2 - R_{\rm St}^{3/2} R_{\rm sh}^{1/2}) = \\ = 3c_{\rm i} R_{\rm St}^{3/2} R_{\rm sh}^{1/2} - \tfrac{2\pi}{3} G\rho_{\rm o} R_{\rm sh}^4 \left[1 - \left(\tfrac{R_{\rm St}}{R_{\rm sh}}\right)^3\right] \ . \end{aligned} \tag{2.27}$$

As we will see later in §5.2 and §5.3, this differential equation describes the position of the shock front.

Numerical solution

We solve this equation numerically using the subroutine `integrate.odeint` from the Scientific python library (Jones et al. 2001). Since the model assumes an infinitesimally thin shell, the shell radius $R_{\rm sh}$ can be compared to the average radius of the ionization front and the average radius of the shock front $R_{\rm SF}$ in the numerical simulations.

Figure 2.4 shows the numerical solution of Eqn.(2.27) for four different cloud masses. In each case the cloud has radius $R = 1\,{\rm pc}$, it consists of pure molecular hydrogen and the central ionizing star emits ionizing photons at a constant rate of $\dot{\mathcal{N}}_{\rm LyC} = 10^{49}\,{\rm s}^{-1}$. The masses of the clouds are $M = 3000\,{\rm M}_\odot$, $M = 5000\,{\rm M}_\odot$, $M = 8000\,{\rm M}_\odot$ and $M = 10000\,{\rm M}_\odot$. We see that when a cloud is sufficiently massive the gravitational force slows down the expansion and eventually the HII region may collapse.

Analytical solution

It is interesting to see if Eqn.(2.27) has an analytical solution. We may re-write Eqn.(2.27) in the following form:

$$\begin{aligned} \ddot{\xi}\left(\xi^3 - k_1^{3/2}\xi^{3/2}\right) + 3\dot{\xi}^2\left(\xi^2 - k_1^{3/2}\xi^{1/2}\right) = \\ = k_1^{3/2}k_2\xi^{1/2} - k_3\xi^4\left[1 - \left(\tfrac{k_1}{\xi}\right)^3\right] \,, \end{aligned} \tag{2.28}$$

where $\xi \equiv R_{\rm sh}$, $\dot{\xi} \equiv \dot{R}_{\rm sh}$, and $\ddot{\xi} \equiv \ddot{R}_{\rm sh}$. Equation 2.28 can be expressed as:

$$\ddot{\xi} + \frac{3}{\xi}\dot{\xi}^2 = \frac{k_1^{2/3}k_2\xi^{1/2} - k_3\xi^4\left[1 - \left(\tfrac{k_1}{\xi}\right)^3\right]}{\xi^3 - k_1^{3/2}\xi^{3/2}} \,, \tag{2.29}$$

where $k_1 = R_{\rm St}$, $k_2 = 3c_{\rm i}$, and $k_3 = \frac{2\pi}{3}G\rho_{\rm o}$. We also require $\xi \neq 0 \Rightarrow R_{\rm Sh} \neq 0$, which is true, and $\xi^3 \neq k_1^{3/2}\xi^{3/2} \Rightarrow \xi \neq k_1$ or $R_{\rm Sh} \neq R_{\rm St}$, which is always true since the HII region is in the D-type phase of expansion.

The Eqn.(2.29) is a second order differential equation. To solve it, we set $\dot{\xi} = \psi$ and

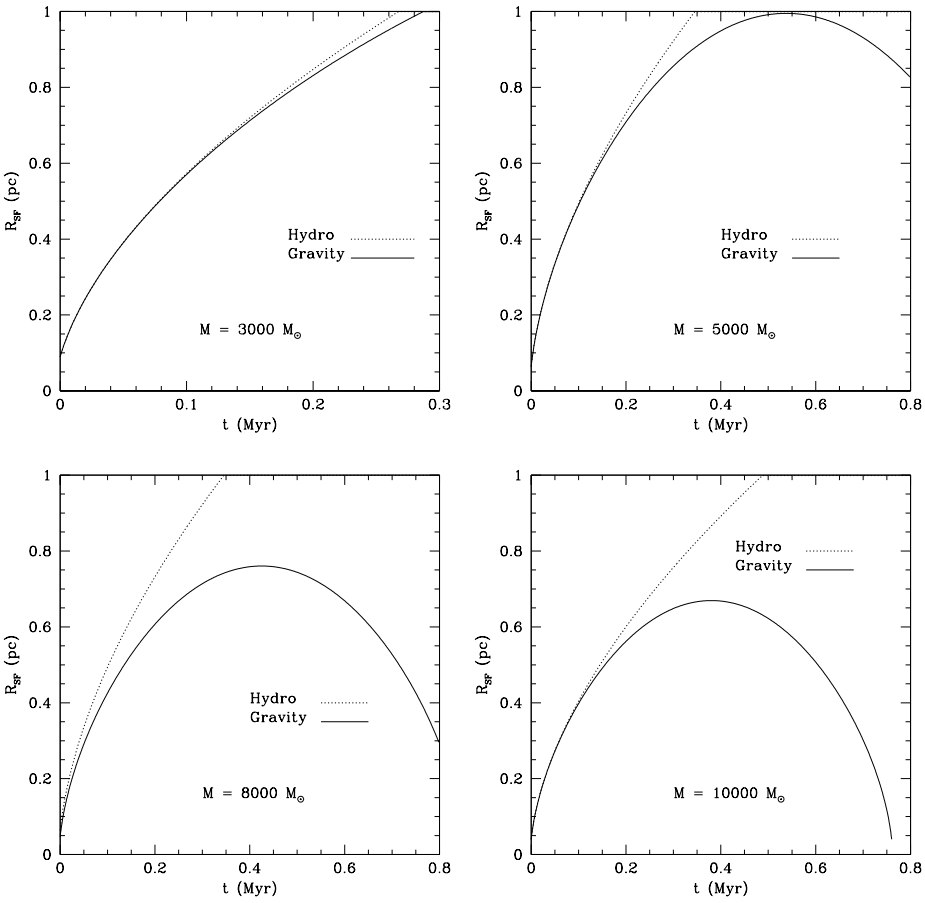

Figure 2.4: These figures show the evolution of the shock front for four different cloud masses without gravity (dotted line) and with gravity (solid line). In all cases the radius of the cloud is $R = 1\,\mathrm{pc}$. We see that when the cloud is sufficiently massive the HII region can collapse.

therefore

$$\ddot{\xi} = \psi \frac{d\psi}{d\xi} \equiv \psi\psi' \tag{2.30}$$

so we obtain

$$\psi\psi' + \psi^2 \frac{3}{\xi} = \frac{k_1^{2/3} k_2 \xi^{1/2} - k_3 \xi^4 \left[1 - \left(\frac{k_1}{\xi}\right)^3\right]}{\xi^3 - k_1^{3/2} \xi^{3/2}} \tag{2.31}$$

or

$$\psi' + \psi f(\xi) = g(\xi)\psi^{-1} \tag{2.32}$$

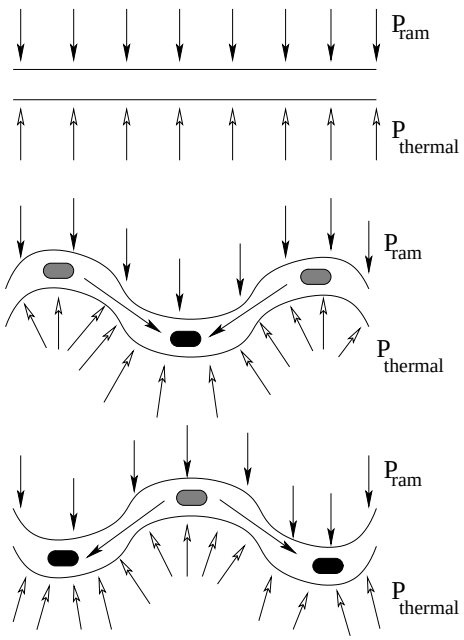

Figure 2.5: Graphical display of the Vishniac instability. The ram pressure is always parallel and opposite to the direction the expansion of the HII region while the thermal pressure of the ionized gas is perpendicular to the surface of the shell. This effect causes the formation an oscillating expanding shell.

where

$$f(\xi) = \frac{3}{\xi},\ g(\xi) = \frac{k_1^{2/3} k_2 \xi^{1/2} - k_3 \xi^4 \left[1 - \left(\frac{k_1}{\xi}\right)^3\right]}{\xi^3 - k_1^{3/2} \xi^{3/2}} \tag{2.33}$$

The latter first order differential equation (Eqn.2.32) is the Bernoulli differential equation. To solve it, let us suppose that $\nu = \psi^2$ and thus $\nu' = 2\psi\psi'$. Therefore, Eqn.(2.32) becomes

$$\nu' + 2f(\xi)\nu = 2g(\xi)\ . \tag{2.34}$$

This is a linear differential equation. To solve it, we consider an integrator multiplier

$$\mu(\xi) = e^{\int 2f(\xi)d\xi} = e^{6\int \frac{d\xi}{\xi}} = e^{6\ln|\xi|} = \xi^6 \tag{2.35}$$

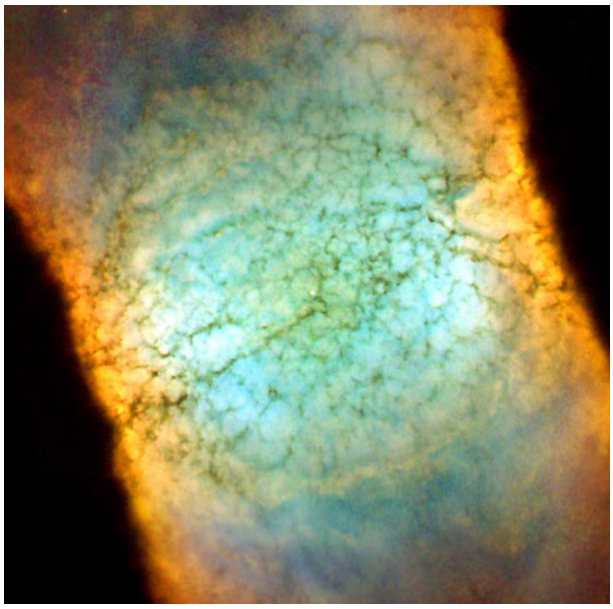

Figure 2.6: The planetary nebula Retina. The existence of the dark filamentary structures is believed to be a result of the Vishniac instability.

and

$$\nu(\xi) = \frac{\int \mu(\xi) 2g(\xi) d\xi + k_4}{\mu(\xi)} \ , \tag{2.36}$$

where k_4 is constant. The integral $I(\xi) = \int \mu(\xi) 2g(\xi) d\xi$ has as analytical solution

$$\begin{aligned} I(\xi) &= \int \mu(\xi) 2g(\xi) d\xi \\ &= \int \frac{2\xi^6 \left\{ k_1^{3/2} k_2 \xi^{1/2} - k_3 \xi^4 \left[1 - \left(\frac{k_1}{\xi} \right)^3 \right] \right\}}{\xi^3 - k_1^{3/2} \xi^{3/2}} d\xi \\ &= -\frac{k_3 \xi^8}{4} - \frac{4}{117} k_1^{3/2} \left(9k_3 \xi^2 - 13k_2 \right) \xi^{9/2} + \frac{2}{3} k_1^{3/2} k_2 \xi^3 + \\ &\quad + \frac{4}{3} k_1^{9/2} k_2 \xi^{3/2} + \frac{4}{3} k_1^6 k_2 \ln \left(\xi^{3/2} - k_1^{3/2} \right) \ . \end{aligned} \tag{2.37}$$

Here we need $\xi^{3/2} - k_1^{3/2} > 0 \Rightarrow \xi > k_1$ or $R_{\rm Sh} > R_{\rm St}$, which is always true.

Therefore, $\dot{R}_{\rm Sh} \equiv \dot{\xi} = \psi = \pm\sqrt{\nu(\xi)} = \pm\sqrt{\frac{I(\xi)+k_4}{\xi^6}}$. The positive sign denotes expansion and the minus sign collapse, so

$$\dot{R}_{\rm Sh} \equiv \dot{\xi} = \pm\sqrt{\frac{I(\xi)+k_4}{\xi^6}}\ . \tag{2.38}$$

This is the analytical solution for the speed of the expanding shell. It is not possible to integrate this to obtain $R_{\rm Sh}$.

2.4 INSTABILITIES

In an expanding HII region instabilities play an important role due to their contribution to the formation of fragments, which in turn might give birth to stars. Here we discuss two important instabilities; the Vishniac instability (Vishniac 1983) and the Rayleigh-Taylor instability.

2.4.1 VISHNIAC INSTABILITY

The Vishniac instability (Vishniac 1983) occurs in a decelerating pressure-driven shell. It has been suggested that this instability plays an important role in the fragmentation of the interstellar medium.

Consider an HII region expanding into a uniform density medium. A shock front forms ahead of the ionization front. The neutral material exerts a ram pressure $P_{\rm n}$ on the shell with direction opposite to the direction of expansion. On the other hand the HII region exerts a thermal pressure $P_{\rm i}$ with direction perpendicular to the surface of the shell. In a uniform shell these two pressures are opposite and parallel. If a perturbation appears, they are not parallel and irregularities will start to grow.

Eventually, the material inside the shell will start flowing creating locally dense and rarefied regions. Their velocities will be smaller and greater relative to the velocity of propagation of the HII region respectively, creating alternating and oscillating density concentrations and rarefractions (see Fig. 2.5).

Vishniac (1983) showed that the amplitude of these oscillations grows as $t^{1/2}$. Their

separation, which is the wavelength of the instability, is comparable with the thickness of the shell.

Observations in expanding HII regions such as the planetary nebula Retina (IC 4406, see Fig. 2.6) or in the emission nebula NGC 6820 (Garcia-Segura & Franco 1996) show the existence of structures with the morphologies predicted by the Vishniac instability.

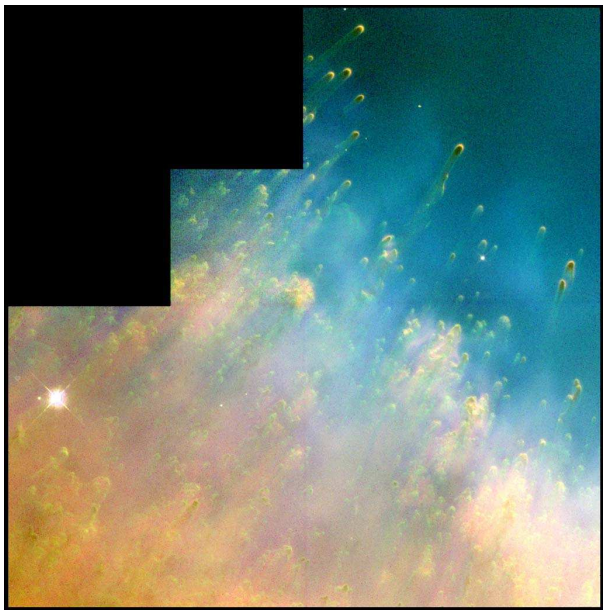

Figure 2.7: Detail of the Helix nebula. The ionizing star is located beyond the top righthand corner.

2.4.2 Rayleigh-Taylor instability

Of great importance in the astrophysical context is the Rayleigh-Taylor instability. It occurs when a lighter fluid is accelerating a heavier fluid. Small perturbations start to develop which magnify as a function of time.

Let us revisit the expanding HII region we described in §2.4.1. Suppose that the spherical cloud has radius $R_{\rm cl}$ and that beyond this distance there is vacuum. When the shock front reaches the edge of the cloud, the HII region will follow an accelerating expansion. Rayleigh-Taylor instability will create dense knots which are able to survive the passage of the ionization front. Behind these dense knots the material remains neutral creating morphologies which look like fingers pointing towards the

ionizing star. If the heads of these fingers are sufficiently dense they will undergo collapse and can give birth to new stars.

The Rayleigh-Taylor instability is commonly found in expanding HII regions, such as the Helix Nebula (NGC 7293, see Fig. 2.7) or the Eagle Nebula (NGC 6611).

2.5 CHAPTER SUMMARY

In this chapter we have described the basic thermodynamics of a gas consiting of hydrogen and helium. We have discussed the ionization balance in an HII region environment and we have shown how the Strømgren radius is obtained. We have studied the D-type expansion of an HII region, the Spitzer solution, and we described a new semi-analytical approximation of the equation of motion of an expanding shell. In the last section we discussed the basic concepts of the Vishniac instability, which occurs in a decelerating pressure-driven shell, and of the Rayleigh-Taylor instability, which occurs when a lighter fluid is accelerating a heavier fluid.

In the next chapter we will discuss about Smooth Particle Hydrodynamics.

3 Smoothed Particle Hydrodynamics

In this chapter we describe Smoothed Particle Hydrodynamics (SPH). SPH represents a fluid with discrete (but overlapping) particles and uses no grid. It is a proven and powerful tool to simulate star formation and fluid dynamics in general.

We begin our discussion with the fundamentals of SPH and we describe how the basic equations of fluid dynamics are constructed using this formalism. We then discuss the integration scheme used in SPH along with the time step used to advance the particles. We close this chapter by describing the use of a tree code and the use of sink particles in SPH which dramatically speed up the calculation process.

3.1 INTRODUCTION

In star formation and in astrophysics in general, the evolution of the interstellar gas is assumed to be described by the fluid equations. In the simple case of a non-magnetic, self-gravitating fluid, the hydrodynamical equations are as follows:

Continuity equation:

$$\frac{\mathrm{d}\rho(\mathbf{r})}{\mathrm{d}t} = -\rho(\mathbf{r})\nabla \cdot \mathbf{v}(\mathbf{r}) \tag{3.1}$$

where $\rho(\mathbf{r})$ is the density of the fluid and $\mathbf{v}(\mathbf{r})$ its velocity at position $\mathbf{r}$. The derivative $\mathrm{d}/\mathrm{d}t$ is the Lagragian time derivative, i.e. the rate of change experienced by an observer moving with the fluid:

$$\frac{\mathrm{d}}{\mathrm{d}t} = \frac{\partial}{\partial t} + \mathbf{v} \cdot \nabla.$$

Eqn.(3.1) describes the conservation of mass.

Momentum equation:

$$\frac{\mathrm{d}\mathbf{v}(\mathbf{r})}{\mathrm{d}t} = -\frac{\nabla P(\mathbf{r})}{\rho(\mathbf{r})} + \mathbf{a}_{\mathrm{grav}}(\mathbf{r}) + \mathbf{a}_{\mathrm{visc}}(\mathbf{r})\,, \tag{3.2}$$

where $P(\mathbf{r})$ is the pressure at position $\mathbf{r}$, $\mathbf{a}_{\mathrm{grav}}(\mathbf{r})$ is the gravitational acceleration and $\mathbf{a}_{\mathrm{visc}}(\mathbf{r})$ is the viscous acceleration. The firt term on the righthand side is the hydrostatic acceleration.

Energy equation:

$$\frac{\mathrm{d}u(\mathbf{r})}{\mathrm{d}t} = -\frac{P(\mathbf{r})}{\rho(\mathbf{r})}\nabla \cdot \mathbf{v}(\mathbf{r}) + \frac{\Gamma - \Lambda}{\rho(\mathbf{r})} + \mathcal{H}_{\mathrm{visc}}\,, \tag{3.3}$$

where $u(\mathbf{r})$ is the thermal energy per unit mass at position $\mathbf{r}$, Γ and Λ are respectively the heating and cooling rates per unit mass due to cosmic rays and electromagnetic radiation and $\mathcal{H}_{\mathrm{visc}}$ is the heating rate due to viscous forces.

By implementing a hydrodynamical algorithm to solve these equations, we are able to simulate the evolution of a given fluid.

3.2 FUNDAMENTALS OF SPH

Smoothed Particle Hydrodynamics (SPH) is a Lagrangian numerical method that describes a given fluid by dividing it into N elements (hereafter *particles*), where N is a large number. It was invented independently by Lucy (1977) and Gingold & Monaghan (1977) to simulate non-axisymmetric self-gravitating hydrodynamical problems in astrophysics. While it uses no grid to compute the overall properties of the fluid, SPH treats every particle not as a mathematical point, but as an extended region. Inside this region there is a constant number of neighbouring particles ($N_{\rm NEIB}$) overlapping each other. In addition, their properties (mass, velocity, position, density, temperature) are smoothed by a kernel function.

In particular, let us suppose that a quantity f is a function of position $\mathbf{r}$. Using Dirac's delta function, δ, we can write $f(\mathbf{r})$ as

$$f(\mathbf{r}) = \int \delta(|\mathbf{r} - \mathbf{r}'|) f(\mathbf{r}') d^3\mathbf{r}', \tag{3.4}$$

where the integral is over all space.

To approximate the above integral, consider any kernel function W satisfying the following two properties:

$$\int W(|\mathbf{r} - \mathbf{r}'|, h) d^3\mathbf{r}' = 1, \tag{3.5}$$

$$\lim_{h \to 0} W(|\mathbf{r} - \mathbf{r}'|, h) = \delta(|\mathbf{r} - \mathbf{r}'|), \tag{3.6}$$

where h is the characteristic length scale of the kernel function. Eqn.(3.5) ensures that W is normalized. Eqn.(3.6) ensures that as h tends to zero W tends to the Dirac δ-function. By substituting the δ function of Eqn.(3.6) into Eqn.(3.4) we obtain

$$f(\mathbf{r}) = \lim_{h \to 0} \int W(|\mathbf{r} - \mathbf{r}'|, h) f(\mathbf{r}') d^3\mathbf{r}', \tag{3.7}$$

and assuming that h is small we get the smoothed value of the quantity f:

$$\langle f(\mathbf{r}) \rangle = \int W(|\mathbf{r} - \mathbf{r}'|, h) f(\mathbf{r}') d^3\mathbf{r}'. \tag{3.8}$$

The latter equation can be written as

$$\langle f(\mathbf{r})\rangle = \int W(|\mathbf{r}-\mathbf{r}'|,h)\frac{f(\mathbf{r}')}{\rho(\mathbf{r}')}\rho(\mathbf{r}')d^3\mathbf{r}' \tag{3.9}$$

or, replacing the integral with a summation (Monaghan, 1992), as

$$\langle f(\mathbf{r})\rangle = \sum_{j=1}^{N} m_j \frac{f_j}{\rho_j} W(|\mathbf{r}-\mathbf{r}'_\mathbf{j}|,h)\,. \tag{3.10}$$

Here the particle j has mass m_j, position $\mathbf{r}_j$ and density ρ_j. Note that in Eqn.(3.10) m_j has replaced the mass element $\rho(\mathbf{r}')\mathrm{d}^3\mathbf{r}'$.

3.2.1 SMOOTHING LENGTH

The quantity h is known as the *smoothing length*. The quantity $2h$ is chosen to be the radius of influence of the kernel function which is by definition the size of an SPH particle. As mentioned above the number of neighbours, N_{NEIB}, is constant so h varies in regions where the fluid density varies. Therefore, the smoothing length is non universal and time varying as the fluid evolves during the simulation.

From the above it follows that the larger the total number of SPH particles, $\mathcal{N}_{\text{SPH}}$, the smaller the smoothing length. As a consequence, when $\mathcal{N}_{\text{SPH}} \to \infty$ then $h \to 0$ and $\langle f(\mathbf{r})\rangle \to f(\mathbf{r})$. Therefore, in the ideal case we treat each particle as a δ function.

3.2.2 SMOOTHING KERNEL

The smoothing kernel describes the extent of a particle's influence. The kernel that is widely used (Monaghan & Lattanzio, 1985) is

$$W(q) = \frac{\sigma}{h^d}\begin{cases} 1-\frac{3}{2}q^2+\frac{3}{4}q^3, & \text{if } 0\le q<1,\\ \frac{1}{4}(2-q)^3, & \text{if } 1\le q\le 2,\\ 0, & \text{if } q>2, \end{cases} \tag{3.11}$$

(see Fig. 3.1a). Here d is the number of dimensions, $q = |\mathbf{r}|/h$, and σ is a normalization factor. Its values for one, two and three dimensions are respectively:

$$\frac{2}{3},\ \frac{10}{7\pi},\ \frac{1}{\pi}.$$

The advantages of this kernel are that it has continuous first and second derivatives and for $r > 2h$ is exactly zero, so there is no influence from the particle beyond this distance. The first derivative of Eqn.(3.11) is

$$\frac{dW(q)}{dq} = -\frac{\sigma}{h^{d+1}} \begin{cases} 3q - \frac{9}{4}q^2, & \text{if } 0 \le q < 1, \\ \frac{3}{4}(2-q)^2, & \text{if } 1 \le q < 2, \\ 0, & \text{if } q \ge 2 \end{cases} \tag{3.12}$$

Note that for $q = \frac{2}{3}$ we have $\frac{d^2W(q)}{dq^2} = 0$ and $\frac{d^3W(q)}{dq^3} > 0$, so there is a local minimum. For $q < \frac{2}{3}$, $\frac{dW(q)}{dq} \to 0$ (for $q = 0$, $\frac{dW(q)}{dq} = 0$). For particles with $q < \frac{2}{3}$, Eqn.(3.11) eliminates the pair pressure leading to artificial particle clumping (Thomas & Couchman 1992).

To avoid this, Thomas & Couchman (1992) replaced the first derivative (Eqn.3.12) with

$$\frac{dW^\star(q)}{dq} = -\frac{\sigma}{h^{d+1}} \begin{cases} 1, & \text{if } 0 \le q < \frac{2}{3}, \\ 3q - \frac{9}{4}q^2, & \text{if } \frac{2}{3} \le q < 1, \\ \frac{3}{4}(2-q)^2, & \text{if } 1 \le q < 2, \\ 0, & \text{if } q \ge 2. \end{cases} \tag{3.13}$$

The difference between Eqn.(3.12) and Eqn.(3.13) is that in the latter for $q < \frac{2}{3}$, $\frac{dW(q)}{dq} = -\frac{\sigma}{h^{d+1}}$. Their tests suggest that using Eqn.(3.13) more accurate results can be obtained.

Figure 3.1 shows a graphical display of equations 3.11, 3.12 and 3.13

3.2.3 EXAMPLE

As an example we can take a uniform density fluid consisting of N particles, each of mass m. The density of each SPH particle is then

$$\rho = \frac{3N_{\text{NEIB}}m}{4\pi(2h)^3}, \tag{3.14}$$

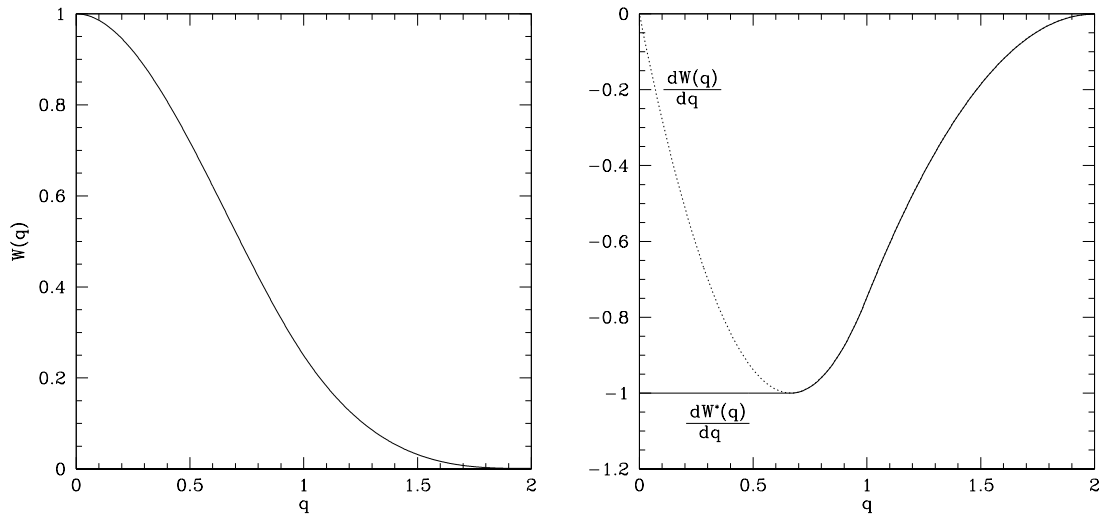

Figure 3.1: (a) Plot of the Monaghan & Lattanzio (1985) kernel. (b) Plot of the Thomas & Couchman (1992) derivative of the kernel (solid line) and the Monaghan & Lattanzio derivative (dotted line). The two curves differ for $q < 2/3$.

so the smoothing length is

$$h = \left(\frac{3 N_{\rm NEIB} m}{32 \pi \rho} \right)^{1/3} . \tag{3.15}$$

Assuming that $m = M/N$, where M is the total mass of the fluid, we get

$$h = \left(\frac{3 N_{\rm NEIB}}{32 \pi \rho} \frac{M}{N} \right)^{1/3} . \tag{3.16}$$

Note that h decreases with increasing N as $h \propto N^{-1/3}$.

3.3 BASIC EQUATIONS

In this section we describe the SPH formulation of the derivatives and its application to the continuity equation, to the momentum equation, and to the energy equation.

3.3.1 Derivatives

To obtain the derivatives of Eqn.(3.10) we use the equation

$$\nabla f(\mathbf{r}) = \int f(\mathbf{r}')\nabla W\left(|\mathbf{r}-\mathbf{r}'|, h\right) d^3\mathbf{r}'. \tag{3.17}$$

The summation approximation of the above is

$$\langle \nabla f(\mathbf{r}) \rangle_i = \sum_j m_j \frac{f_j}{\rho_j} \nabla_i W(|\mathbf{r_i} - \mathbf{r_j}|, h) \tag{3.18}$$

where ∇_i denotes the derivative taken with respect to the coordinates of the particle i. A more robust estimate of $\langle \nabla f(\mathbf{r}) \rangle_i$ can be obtained using the identity

$$\rho \nabla f = \nabla\left(\rho f\right) - f\nabla\rho \Rightarrow \nabla f = \frac{1}{\rho}\nabla\left(\rho f\right) - \frac{f}{\rho}\nabla\rho \tag{3.19}$$

This gives

$$\begin{aligned} \langle \nabla f \rangle_i = \frac{1}{\rho_i}\sum_j m_j f_j \nabla_i W(|\mathbf{r_i} - \mathbf{r_j}|, h) - \frac{f_i}{\rho_i}\sum_j m_j \nabla_i W(|\mathbf{r_i} - \mathbf{r_j}|, h) \Rightarrow \\ \langle \nabla f \rangle_i = \sum_j m_j \left(\frac{f_j - f_i}{\rho_i}\right) \nabla_i W(|\mathbf{r_i} - \mathbf{r_j}|, h), \end{aligned} \tag{3.20}$$

Alternative, we can use the identity

$$\nabla\left(\frac{f}{\rho}\right) = \frac{\nabla f}{\rho} - \frac{f}{\rho^2}\nabla\rho \Rightarrow \nabla f = \rho\nabla\left(\frac{f}{\rho}\right) + \frac{f}{\rho}\nabla\rho \tag{3.21}$$

As above, we have

$$\begin{aligned} \langle \nabla f \rangle_i = \rho_i \sum_j m_j \frac{f_j}{\rho_j^2} \nabla_i W(|\mathbf{r_i} - \mathbf{r_j}|, h) + \frac{f_i}{\rho_i}\sum_j m_j \nabla_i W(|\mathbf{r_i} - \mathbf{r_j}|, h) \Rightarrow \\ \langle \nabla f \rangle_i = \rho_i \sum_j m_j \left(\frac{f_j}{\rho_j^2} + \frac{f_i}{\rho_i^2}\right) \nabla_i W(|\mathbf{r_i} - \mathbf{r_j}|, h). \end{aligned} \tag{3.22}$$

The last approximation is used in the particular case of the pressure gradient. We could reach the same equations using the Taylor expansion approximation and omitting any factors greater than $\mathcal{O}\left(h^2\right)$. An extended discussion of the errors can be

found in Price (2005; PhD thesis).

3.3.2 CONTINUITY EQUATION

In Eqn.(3.10) we replace $f(\mathbf{r}')$ with $\rho(\mathbf{r}')$ and obtain

$$\rho_i = \sum_j m_j W(|\mathbf{r_i} - \mathbf{r_j}|, h). \tag{3.23}$$

This is the continuity equation which estimates the density ρ_i at the position $\mathbf{r_i}$ of particle i.

Monaghan (1992) proposed that the above equation can be replaced by

$$\frac{\mathrm{d}\rho_i}{\mathrm{d}t} = \sum_j m_j \mathbf{v_{ij}} W(|\mathbf{r_i} - \mathbf{r_j}|, h) \tag{3.24}$$

where $\mathbf{v_{ij}} = \mathbf{v_i} - \mathbf{v_j}$ is the difference in velocity vectors. The latter has advantages at fluid boundaries, and in shock simulations, but introduces errors in the conservation of mass.

3.3.3 MOMENTUM EQUATION

We approximate Eqn.(3.2) using the result of Eqn.(3.22) since the latter is symmetric. This means that the hydrodynamic pair forces between particles i and j are equal and opposite, and therefore conservation of momentum is promoted. This gives:

$$\frac{\mathrm{d}\mathbf{v}_i}{\mathrm{d}t} = -\sum_j m_j \left(\frac{P_j}{\rho_j^2} + \frac{P_i}{\rho_i^2}\right) \nabla_i W(|\mathbf{r_i} - \mathbf{r_j}|, h) + \mathbf{a}_{\mathrm{grav},i}(\mathbf{r}) + \mathbf{a}_{\mathrm{visc},i}(\mathbf{r}) \tag{3.25}$$

Here P_i and P_j are the pressures, and ρ_i and ρ_j the densities, of the i and j particles respectively.

The term $\mathbf{a}_{\mathrm{grav},i}(\mathbf{r}_i)$

The term $\mathbf{a}_{\mathrm{grav},i}(\mathbf{r}_i)$ describes the total gravitational acceleration of each particle i due to the contribution from all other particles, i.e. $j \in [1, N], j \neq i$. This gives:

$$\mathbf{a}_{\mathrm{grav},i}(\mathbf{r}_i) = \sum_{j=1, j\neq i}^{N} \frac{G m_j (\mathbf{r_j} - \mathbf{r_i})}{|\mathbf{r_i} - \mathbf{r_j}|^3}. \tag{3.26}$$

Thus we need $N(N-1) \sim N^2$ calculations to evaluate $\mathbf{a}_{\mathrm{grav},i}(\mathbf{r}_i)$. This means that the computational cost increases rapidly when N is increased. We discuss later on the use of tree codes to reduce the computational cost of estimating $\mathbf{a}_{\mathrm{grav},i}(\mathbf{r}_i)$.

The term $\mathbf{a}_{\mathrm{visc},i}(\mathbf{r}_i)$

The term $\mathbf{a}_{\mathrm{visc},i}(\mathbf{r}_i)$ describes the acceleration of particle i due to the viscous forces.

In SPH the standard form for $\mathbf{a}_{\mathrm{visc},i}(\mathbf{r}_i)$ is:

$$\mathbf{a}_{\mathrm{visc},i}(\mathbf{r}_i) = \sum_j m_j \Pi_{ij} \nabla_i W(|\mathbf{r_i} - \mathbf{r_j}|, h), \tag{3.27}$$

where Π_{ij} is the viscosity parameter, and is given by (Monaghan, 1992)

$$\Pi_{ij} = \begin{cases} \frac{-\alpha \bar{c}_{ij} \mu_{ij} + \beta \mu_{ij}^2}{\bar{\rho}_{ij}}, & \mathbf{v_{ij}} \cdot \mathbf{r_{ij}} < 0\,; \\ 0, & \mathbf{v_{ij}} \cdot \mathbf{r_{ij}} > 0\,; \end{cases} \tag{3.28}$$

and

$$\mu_{ij} = \frac{h_{ij} \mathbf{v_{ij}} \cdot \mathbf{r_{ij}}}{\mathbf{r_{ij}}^2 + \eta^2}. \tag{3.29}$$

Here, $\mathbf{r_{ij}} = \mathbf{r_i} - \mathbf{r_j}$, $\bar{\rho}_{ij} = (\rho_i + \rho_j)/2$, $h_{ij} = (h_i + h_j)/2$ and $\bar{c}_{ij} = (c_i + c_j)/2$, where c_i is the sound speed of particle i. The term η^2 acts as a safety factor to prevent a numerical singularity when $|\mathbf{r_{ij}}|$ becomes very small. The values $\alpha = 1$, $\beta = 2$ and $\eta^2 = 0.01h^2$ give good results, and are widely used. In Eqn.(3.28) the term $-\alpha \bar{c}_{ij} \mu_{ij}$ is linear and produces a bulk viscosity while $\beta \mu_{ij}^2$ is a quadratic term and is included to prevent particle penetration.

We call this kind of viscosity *artificial viscosity* since it is not informed by physical

considerations, and we include it to prevent inter-penetration of converging particle streams. Without this term, post shock oscillations may occur, when simulating shock fronts, and particles may pass through the shock rather than decelerating.

We now combine Eqn.(3.27) with Eqn.(3.25) to obtain

$$\frac{\mathrm{d}\mathbf{v}_i}{\mathrm{d}t} = -\sum_j m_j \left(\frac{P_j}{\rho_j^2} + \frac{P_i}{\rho_i^2} + \Pi_{ij} \right) \nabla_i W(|\mathbf{r_i} - \mathbf{r_j}|, h) + \mathbf{a}_{\mathrm{grav},i}(\mathbf{r}) \tag{3.30}$$

This is the SPH form of the momentum equation.

3.3.4 ENERGY EQUATION

As in the momentum equation, we use Eqn.(3.22) to write the energy equation (Eqn.3.3) in the form

$$\frac{\mathrm{d}u_i}{\mathrm{d}t} = -\frac{1}{2}\sum_j m_j \left(\frac{P_j}{\rho_j^2} + \frac{P_i}{\rho_i^2} + \Pi_{ij} \right) \mathbf{v_{ij}} \nabla_i W(|\mathbf{r_i} - \mathbf{r_j}|, h) + \frac{\Gamma_i - \Lambda_i}{\rho_i}. \tag{3.31}$$

We have used the viscosity parameter Π_{ij} to take into account heating due to the artificial viscous forces. We do not need to solve Eqn.(3.31), if we invoke a barotropic equation of state, $P = P(\rho)$, or a positional temperature dependence $T = T(\mathbf{r})$.

3.4 CONSERVATION OF QUANTITIES

From the above section we see that in SPH physical quantities such as the mass and the momentum are conserved. Price (2005; PhD Thesis) shows that angular momentum is well conserved with this formalism. This is a consequence of the Lagragian nature that SPH is based on. Monaghan (2002) introduce the 'grad-h' SPH method where attention is drawn on the conservation of energy. In the present Thesis all simulations performed are using this latter formalism to ensure conservation of energy.

3.5 Integration schemes

SPH codes use a variety of integration schemes, such as the first-order Euler scheme, the second-order leapfrog scheme, the second-order Runge-Kutta scheme, the second-order predictor-corrector scheme, and other alternative schemes. For example the first-order Euler method for the position $\mathbf{r}$ and the velocity $\mathbf{v}$ of a given particle is simply:

$$\mathbf{r}_{k+1} = \mathbf{r}_k + \mathbf{v}_k \Delta t \tag{3.32}$$

$$\mathbf{v}_{k+1} = \mathbf{v}_k + \mathbf{a}_k \Delta t \tag{3.33}$$

where $\mathbf{a}$ is its acceleration, k is an integer number to denote the iteration step, and Δt is the time step. A discussion on the calculation of the time step follows in §3.6.

Due to the large errors introduced by the above first-order scheme, second-order schemes are more commonly used. These use a mid-point "half-step" between t and $t + \Delta t$ to calculate the accelerations. As an example, the leapfrog scheme (which is used in all the simulations presented here) evaluates the last set of equations as:

$$\mathbf{r}_{k+1} = \mathbf{r}_k + \mathbf{v}_{k+1/2} \Delta t \tag{3.34}$$

$$\mathbf{v}_{k+1/2} = \mathbf{v}_{k-1/2} + \mathbf{a}_k \Delta t. \tag{3.35}$$

Here, the positions $\mathbf{r}$ and the accelerations $\mathbf{a}$ are evaluated in each full step, while the velocities $\mathbf{v}$ are evaluated in each half-step.

We can reduce the numerical errors still further by using higher order schemes (e.g. fourth-order Runge-Kutta), but at the expense of computational cost.

3.6 Time step

As mentioned in §3.5 the time step Δt is used to integrate the SPH equations 3.34 and 3.35. For a given particle, Δt must be chosen to ensure that the relative positions and velocities of its neighbouring particles do not change by a large amount in one time step. The calculation of the time step is therefore of great importance. Δt is determined by the acceleration of the given particle, and the Courant condition (Courant et al. 1967) combined with the viscous diffusion term (Monaghan 1992). A

third term is added when we solve the energy equation explicitly. The condition to evaluate the time step is:

$$\Delta t_{\rm i} = \gamma \mathrm{MIN}\left\{\Delta t^{\rm i}_{\rm acc}, \Delta t^{\rm i}_{\rm courant}, \Delta t^{\rm i}_{\rm energy}\right\} \tag{3.36}$$

where γ is a time multiplication constant (in the simulations presented here we set $\gamma \sim 0.1$). The first term

$$\Delta t^{\rm i}_{\rm acc} = \sqrt{\frac{h_{\rm i}}{|\mathbf{a}_{\rm i}| + \eta_{\rm acc}}}, \tag{3.37}$$

is to ensure that the particle moves less than a distance $h_{\rm i}$ in one time step. The term $\eta_{\rm acc}$ is a small acceleration, added to avoid division by zero. The second term

$$\Delta t^{\rm i}_{\rm courant} = \frac{h_{\rm i}}{(1+1.2\alpha)c_{\rm i} + (1+1.2\beta)h_{\rm i}|\nabla \mathbf{v}_{\rm i}|} \tag{3.38}$$

is the modified Courant condition. The values α and β were given in §3.3.3. The third term is

$$\Delta t^{\rm i}_{\rm energy} = \frac{u_{\rm i}}{|du_{\rm i}/dt| + \eta_{\rm enrg}} \tag{3.39}$$

and limits the fractional change in the internal energy. Here $\eta_{\rm enrg}$ is a small rate of change of energy, added to avoid division by zero.

Thus Eqn.(3.36) determines the time step $\Delta t_{\rm i}$ for the SPH particle i. For a simulation consisting of N SPH particles, we can use a universal time step,

$$\Delta t_{\rm SIM} = \mathrm{MIN}\left\{\Delta t_{\rm i}\right\},\ i = 1, N. \tag{3.40}$$

However, a universal time step slows down the calculations; in a simulation there will be particles which have time step greater than $\Delta t_{\rm SIM}$. Treating those particles with a time step smaller than required increases the computational cost. To avoid this, a multiple time stepping scheme is implemented, which ensures that the code only treats the detailed evolution of a particle when this is necessary.

3.7 Tree code

As we saw in §3.3.3 the calculation of the gravitational acceleration $\mathbf{a}_{\mathrm{grav},i}(\mathbf{r})$ increases dramatically the computational cost of a simulation with large N, since it is of order $\mathcal{O}(N^2)$. Barnes & Hut (1986) implemented a method for reducing the computational time from $\mathcal{O}(N^2)$ to $\mathcal{O}(N \log N)$. It is commonly used in SPH codes.

In this method an initial cubical cell is considered to contain all the SPH particles of the main computational domain. This cell is known as the "root cell". The root cell is divided into subdivisions called octans. Each octan is an individual cell. In each subdivision, the child cell has half the edge of the parent cell. This process continues until each cell contains a few SPH particles. In the simulations presented here we stop the subdivisions once 8 SPH particles or less are enclosed in the same cell.

After the tree is built we follow a "tree walking" scheme to calculate the gravitational forces. If we consider any particle i, this scheme examines the position of the particle i with respect to the centre of each child cell of the root cell. If the cell is too close, we subdivide (open) it further as described above. The gravitational forces from the closest particles to particle i are calculated using a direct sum (Eqn.3.26). If a cell is far away, we treat its particles as a cluster. The condition to subdivide a cell is

$$\frac{\ell}{d} > \theta_{\mathrm{max}}$$

where ℓ is the size of the cell, d its distance from the position of particle i and θ_{max} is a fixed tolerance parameter.

For $\theta_{\mathrm{max}} = 1$ the tree code calculates the acceleration with $\sim 1\%$ error (Hernquist, 1987). More accurate estimation is obtained with $\theta_{\mathrm{max}} = 0.577$ (Salmon, Warren & Winckelmans, 1994). In the simulations presented here we use $\theta_{\mathrm{max}} = 0.447$.

3.8 Sink particles

From the discussion in §3.6 we see that in a simulation where dense regions develop, which in turn have small smoothing lengths, the time step reduces dramatically and the overall simulation can become prohibitively long. To avoid this, Bate et al (1995) implemented a method which replaces the densest regions with sink particles.

In this method, a dense region with density ρ above a threshold density $\rho_{\rm SINK}$ is considered to be dominated by gravitational forces. Eventually, it will undergo collapse and a star will form. We call as *seed* particle the SPH particle that triggers the formation of a sink particle. A sink particle interacts gravitationally with all other sink and SPH particles, but does not interact hydrodynamically with any other objects. It has a finite radius $r_{\rm SINK} = R_{\rm K} h_s$, with h_s the smoothing length of the seed particle, and $R_{\rm K}$ a user-defined number. In the simulations presented here we have set $R_{\rm K} = 2$ at all times.

There are several diagnostic criteria followed for an SPH particle to be replaced by a sink particle (Hubber et al. 2009, in prep.):

- the SPH density of the seed particle and all its neighbours should be greater than $\rho_{\rm SINK} = (\sim 10^{-11}\,{\rm g\,cm^{-3}})$;
- there should be no other sink particle within $2r_{\rm SINK}$;
- the SPH velocity divergence of the seed particle is negative $(\nabla \mathbf{v})_{\mathbf{s}} < \mathbf{0}$ (this ensures that the particles going into the sink are condensing, and not being sheared apart);
- the SPH acceleration divergence of the seed particle is negative $(\nabla \mathbf{a})_{\mathbf{s}} < \mathbf{0}$ (this ensures that the condensation in not being torn apart by tidal forces);
- the total mechanical energy of the seed particle and its neighbours (kinetic plus gravitational potential energy in the centre-of-mass frame) is negative.

At the moment of formation, the initial mass of the sink will be therefore $m_{\rm SINK,0} \sim \mathcal{N}_{\rm NEIB} m$, where m is the mass of an SPH particle. Once a sink is formed two further criteria are applied in order for an SPH particle i in the vicinity of the sink to be accreted:

- the SPH particle lies inside the sink-particle's radius, $|\mathbf{r_i} - \mathbf{r_s}| < \mathbf{ler}_{\rm SINK}$,
- the kinetic plus gravitational energy of the tw-body system comprising the sink-particle and the SPH-particle is negative.

The above technique significantly speeds up the computational speed, since it prevents the time step from having very small values.

3.9 The SEREN SPH code

We use the SPH code SEREN, which has been designed to investigate star and planet formation problems, and extensively tested on a wide range of standard problems, as described in Hubber et al. (2009; in press) and on the SEREN webpage[1]. SEREN offers a number of user-defined options. In the present Thesis we use standard SPH (Monaghan 1992), and standard artificial viscosity with no switches. The SPH equations of motion are solved with a second-order Leapfrog integrator, in conjunction with a block time-stepping scheme. Gravitational forces are calculated using an octal-spatial tree (Barnes & Hut 1986), with monopole and quadrupole terms and a standard geometric opening-angle criterion. The tree is also used to facilitate the generation of neighbour lists.

3.10 Chapter summary

In this chapter we have described Smoothed Particle Hydrodynamics. SPH treats every particle as an extended region whose size is defined by the smoothing length. Inside this region there is a constant number of neighbouring particles. All properties of these particles are smoothed by a kernel function. SPH uses a variety of integration schemes to calculate the accelerations of the particles. For the integrations, a time step criterion is used which is chosen to ensure that the relative positions and velocities of the neighbouring particles do not change by a large amount. In addition, in order to calculate the gravitational accelerations a tree code is used which reduces dramaticaly the computational cost. Finally, if an SPH particle exceeds a critical density value, we replace it and its neighbours with a sink particle since it will inevitably undergo gravitational collapse and will form a star.

In the next chapter we will discuss the numerical treatment of the propagation of ionizing radiation.

[1] http://www.astro.group.shef.ac.uk/seren

4 Numerical Treatment

In this chapter we describe how we treat numerically the transport of ionizing radiation, in order to simulate the evolution of an HII *region. The algorithm creates a set of rays emanating from the ionizing source, along which the ionizing photons propagate into the interstellar medium. The ray casting scheme we follow is described in §4.1. We split the rays as they spread away from the source, in order to achieve good resolution at low computational cost. In §4.2 we discuss the ray splitting criterion and how this results in an hierarchy of rays covering all possible directions. In §4.3 we discuss how we avoid numerical artifacts due to discretization in angle.*

Once we have built the hierarchy of rays around the source, we set temperatures of the SPH particles. This is described in §4.4. In §4.5 we show how we locate the position of the ionization front along each ray. Due to the small thickness of the ionization front compared with the HII *region, we smooth the transition between the ionized and the neutral material; the technique for doing this is discussed in §4.6. Finally, in §4.7 we give the basic technical parameters of the algorithm used in the present Thesis.*

4.1 RAY CASTING

In order to determine the overall shape of the ionization front we consider many different directions, each characterized by a unit vector $\hat{\mathbf{e}}$. These directions are chosen using the HEALPix algorithm (Górski et al. 2005). HEALPix generates a set of $\mathcal{N}_{\rm RAYS} = 12 \times 4^{\ell}$ directions (hereafter 'rays'), where ℓ is the level of refinement and $\ell = 0$ is the lowest level. The rays of level ℓ are distributed uniformly over the celestial sphere, as seen from the ionizing star. Each ray on level ℓ intersects the celestial sphere at the centre of an approximately square element of solid angle

$$\Delta\Omega_{\ell} = \frac{4\pi}{\mathcal{N}_{\rm RAYS}} \text{ steradians} = \frac{\pi}{3 \times 4^{\ell}} \text{ steradians.}$$

Therefore, the angle between neighbouring rays is of order

$$\Delta\theta_{\ell} \simeq (\Delta\Omega_{\ell})^{1/2} \simeq 2^{-\ell} \text{ radians.}$$

When HEALPix goes to a higher level, ℓ, the angular resolution is increased by splitting each of the rays at the previous level, $\ell - 1$, into four rays (see §4.2).

The integral on the left-hand side of Eqn.(2.11) must be evaluated numerically along each ray until it equals $I_{\rm MAX}$, where

$$I_{\rm MAX} = \frac{\dot{\mathcal{N}}_{\rm LyC} m^2}{4\pi\alpha_{\rm B}} \,. \tag{4.1}$$

To perform this integration we define a set of discrete evaluation points along each ray. At each evaluation point, j, we determine the density ρ_j using an SPH summation over the $\mathcal{N}_{\rm NEIB}$ nearest SPH particles, k,

$$\rho_j = \sum_k \left\{ \frac{m_k}{h_j^3} W\left(\frac{|\mathbf{r}_k - \mathbf{r}_j|}{h_j} \right) \right\} . \tag{4.2}$$

The integral in Eqn.(2.11) is then evaluated using the trapezium method

$$\begin{aligned} I(r_j) &= \int_{r=0}^{r=r_j} \rho^2 \left(r\hat{\mathbf{e}}\right) r^2 \mathrm{d}r \\ &\simeq \sum_{j'=1}^{j'=j} \left\{ \left(\frac{\rho_{j'-1}^2 r_{j'-1}^2 + \rho_{j'}^2 r_{j'}^2}{2} \right) f_1 h_{j'-1} \right\} , \end{aligned} \tag{4.3}$$

where f_1 is a dimensionless tolerance parameter of order unity controlling the integration step, and $h_{j'}$ is the smoothing length of evaluation point j'. The identifier $j' = 1$ denotes the evaluation point placed at the position of the star, and consecutive evaluation points are then located according to

$$\mathbf{r}_{j'+1} = \mathbf{r}_{j'} + f_1 h_{j'} \hat{\mathbf{e}} \,. \tag{4.4}$$

Thus $f_1 h_{j'}$ represents the adaptive step along the line of sight from the ionizing star towards the ionization front. Figure 4.1 shows a representation of the method. Acceptable accuracy is obtained with $f_1 = 0.25$.

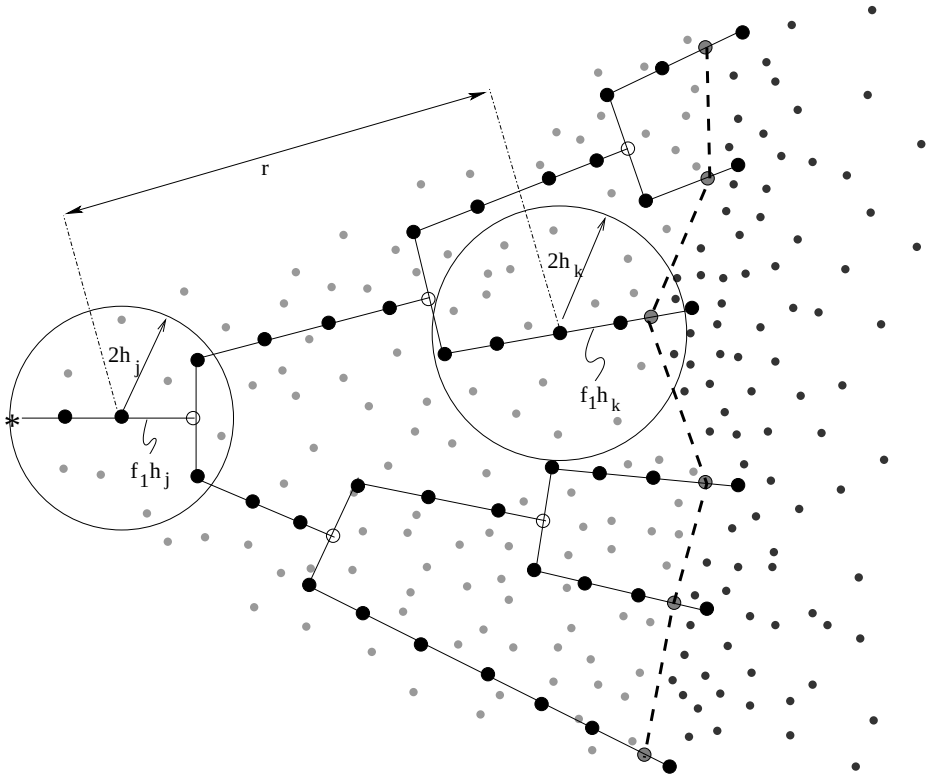

Figure 4.1: This figure shows the evaluation points (big black dots) along a family of rays (solid lines), starting from the ionizing star. To reduce confusion, the ray casting is plotted in 2-D. A ray is split as soon as its linear separation from neighbouring rays, $r_j \Delta\theta_\ell$, exceeds $f_2 h_j$, where h_j is the smoothing length of the local evaluation point. Evaluation points where rays are split have been marked with open circles to indicate that they make no contribution to the summation in Eqn.(4.3). A binary chop subroutine is used to locate the position of the ionization front (see §4.5).

4.2 RAY SPLITTING

The use of ray splitting allows us to maintain good resolution while achieving significant speed-up in comparison with uniform ray tracing (cf. Abel & Wandelt 2002). In our scheme a ray is split into four child-rays as soon as its linear separation from neighbouring rays, $r_j \Delta\theta_\ell$, exceeds $f_2 h_j$. Here r_j is the distance from the ionizing star to evaluation point j, f_2 is a dimensionless parameter controlling the angular resolution of the ensemble of rays representing the ionizing radiation, and h_j is the smoothing length of the local evaluation point j. Hence we require

$$\ell \geq \log_2 \left(\frac{r_j}{f_2 h_j} \right) . \tag{4.5}$$

Acceptable results are obtained with f_2 in the range $(1.0, 1.3)$. A smaller f_2 gives greater accuracy, but at the expense of more HEALPix rays. As one moves outwards away from the central star, rays are only ever split, they are never merged.

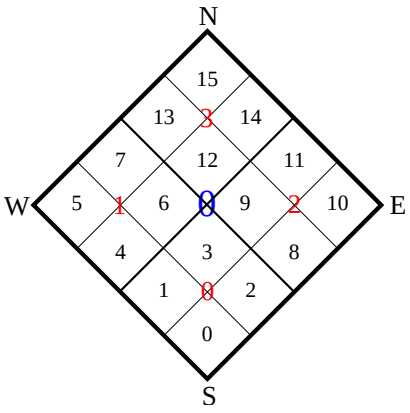

Figure 4.2: Illustration of the scheme used for splitting a ray using HEALPix's `NESTED` scheme. This map shows the tessellation of the celestial sphere corresponding to three successive levels of HEALPix. Each tessera has a ray at its centre. The big bold tessera represents the solid angle $\Delta\theta_\ell$ of a single ray at level ℓ. The four intermediate tesserae represent the solid angles of its child-rays at level $\ell + 1$. And the sixteen smallest tesserae represent the solid angles of its grandchild-rays at level $\ell + 2$.

The `NESTED` version of HEALPix allocates identifiers to rays according to the scheme illustrated in Fig. 4.2, which shows a small patch on the celestial sphere. Here the mother-ray, m of ray m' has ID

$$m = \mathrm{INT} \left(\frac{m'}{4} \right) \tag{4.6}$$

and the four child-rays of ray m' have IDs

$$m'' = 4m' + n, \text{ with } n = 0, 1, 2, 3 \tag{4.7}$$

Here $n = 0$ corresponds to the child-ray to the South, $n = 1$ corresponds to the child-ray to the West, $n = 2$ corresponds to the child-ray to the East and $n = 3$ corresponds to the child-ray to the North. This numbering scheme makes it very simple to trace a ray back to the star at the origin, provided we know the ID of the ray *and* its level.

4.3 Ray rotation

To avoid numerical artifacts due to the discretization in the directions of rays, we rotate the ensemble of HEALPix rays through three random angles (about the $z-$, $x'-$, and $z''-$ axes), each time we build the ensemble. This process is necessary to prevent the formation of artificial corrugations in the ionization front, as explained in detail in Krumholz et al. (2007).

The ensemble of rays is rotated according to the following matrix

$$A = \begin{pmatrix} a_{11} & a_{12} & a_{13} \\ a_{21} & a_{22} & a_{23} \\ a_{31} & a_{32} & a_{33} \end{pmatrix},$$

where

$$\begin{aligned}
a_{11} &= \cos\theta_1 \cos\theta_3 - \sin\theta_1 \cos\theta_2 \sin\theta_3 \\
a_{21} &= -\sin\theta_1 \cos\theta_3 - \sin\theta_3 \cos\theta_1 \cos\theta_2 \\
a_{31} &= \sin\theta_2 \sin\theta_3 \\
a_{12} &= \cos\theta_1 \sin\theta_3 + \sin\theta_1 \cos\theta_2 \cos\theta_3 \\
a_{22} &= -\sin\theta_1 \sin\theta_3 + \cos\theta_1 \cos\theta_2 \cos\theta_3 \\
a_{32} &= -\sin\theta_2 \cos\theta_3 \\
a_{13} &= \sin\theta_2 \sin\theta_1 \\
a_{23} &= \cos\theta_1 \sin\theta_2 \\
a_{33} &= \cos\theta_2
\end{aligned}$$

Here $\theta_1 \in [0, 2\pi]$, $\theta_2 \in [0, \pi]$, $\theta_3 \in [0, 2\pi]$ are the random angles about the $z-$, $x'-$, and $z''-$ axes respectively.

4.4 SETTING TEMPERATURES

At each evaluation point we estimate the value of $I(r_j)$ using Eqn.(4.3). If the calculation returns $I(r_j) < I_{\rm MAX}$, then the evaluation point lies in the interior of the HII region . Therefore, some of the particles that belong to its neighbour list should be ionized. We flag a particle as ionized, if it passes the following two tests: (a) its coordinates are inside the solid angle of the ray; and (b) its distance from the star is smaller than the distance of the evaluation point (r_j). If a particle is ionized, it is given a temperature $T = T_{\rm i}$. Otherwise it remains neutral with temperature $T = T_{\rm n}$. Figure 4.3 illustrates the location of the neighbours of evaluation point j, and the ones which pass these tests.

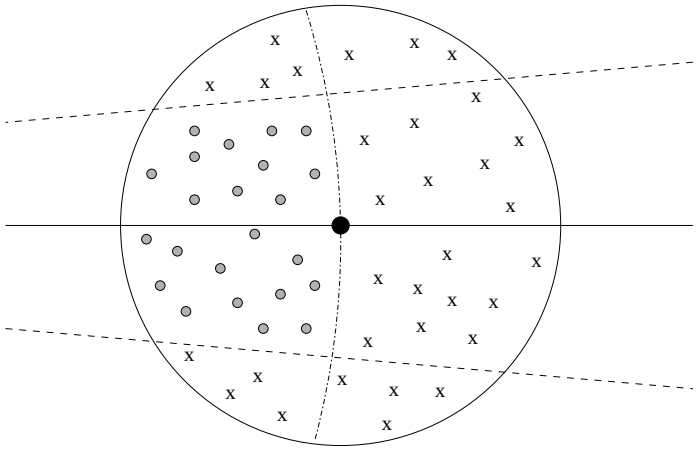

Figure 4.3: This figure shows a single ray (solid line) along with the boundaries of its solid angle (dash lines); the star lies on the left hand side and the ionization front on the right. The big black dot is the evaluation point j, and the circle is its smoothing region. The dot dashed line shows the position where the distance from the star is the same as that of the evaluation point. Small grey dots are particles which are flagged as being ionized, and the crosses are particles which are - for the time being - flagged as being neutral.

4.5 Location of the ionization front

We store in memory the value of the integral in Eqn.(4.3) and the coordinates of the evaluation point at the end of a given ray segment. The distance $R_{\rm IF}$ of the ionization front from the star along a given ray is given by the condition $I\left(R_{\rm IF}\right) = I_{\rm MAX}$. It is determined using a binary chop algorithm between the last two evaluation points r_{j-1} and r_j for which $I\left(r_{j-1}\right) < I_{\rm MAX} < I\left(r_j\right)$.

At each step of the binary chop loop we compare the new value $I\left(r_j\right)$ of the integral with the maximum $I_{\rm MAX}$. If the difference between these two values is smaller than $10^{-3}h_{j-1}$ we exit the binary chop subroutine and the position of the evaluation point in the last loop defines the position of the ionization front. However, as the HII region evoles, the high density jump in the shock front acts to prevent convergence of the integral $I\left(r\right)$ towards $I_{\rm MAX}$. At this stage we exit the binary chop subroutine after 10 iterations which ensures that the precision is of order $10^{-3}h_{j-1}$.

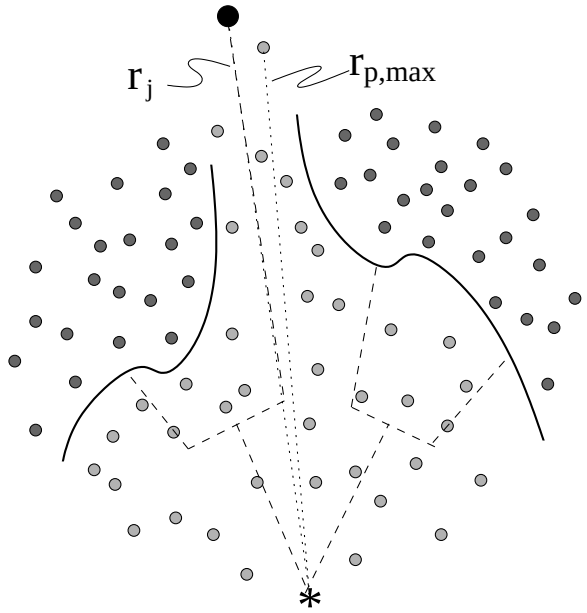

Figure 4.4: This figure shows how a ray penetrates the borders of the cloud. Once it finds no more neutral material to ionize along its line of sight, it is characterized as *open*.

If the material of the cloud along the line of sight of a ray is sufficiently rarefied, $I\left(r\right)$ may never reach $I_{\rm MAX}$ within the computational domain. We therefore estimate the maximum distance $r_{p,\rm max}$ of all gas particles and if $r_j > r_{p,\rm max}$ we stop calculating the sum. Any ray that satisfies this condition is characterized as *open* and the position

of the ionization front is not determined along such rays (see Fig. 4.4).

4.6 TEMPERATURE SMOOTHING

It is not feasible to resolve the ionization front in a standard SPH simulation of an evolving HII region. For example, consider an HII region having uniform density $\rho_{\rm i}$. The SPH particles have a universal mass $m_{\rm SPH}$. If each SPH particle has $\mathcal{N}_{\rm NEIB}$ neighbours, then the diameter, d, of an SPH particle (i.e. the diameter of its smoothing kernel) is given by

$$\begin{aligned} \frac{\pi\, d^3\, \rho_{\rm i}}{6} &= \mathcal{N}_{\rm NEIB}\, m_{\rm SPH}\,, \\ d &= \left(\frac{6\, \mathcal{N}_{\rm NEIB}\, m_{\rm SPH}}{\pi\, \rho_{\rm i}} \right)^{1/3}\,. \end{aligned} \tag{4.8}$$

Since d is in effect the resolution of the simulation, the ionization front can only be resolved if $d \lesssim \Delta R_{\rm IF}$. Using Eqn.(2.13), this requirement reduces to

$$m_{\rm SPH} \lesssim \frac{\pi\, (20)^3\, m^3}{6\, \mathcal{N}_{\rm NEIB}\, \rho_{\rm i}^2\, \bar{\sigma}^3}\,. \tag{4.9}$$

Combining Eqn.(2.24) and Eqn.(2.23), we see that the mass of the HII region is given by

$$M_{\rm i} = \frac{m^2\, \dot{\mathcal{N}}_{\rm LyC}}{\alpha_{\rm B}\, \rho_{\rm i}}\,. \tag{4.10}$$

The number of SPH particles required to model the HII region and resolve the ionization front is therefore

$$\mathcal{N}_{\rm i} = \frac{M_{\rm i}}{m_{\rm SPH}} \tag{4.11}$$

$$\gtrsim \frac{6\, \bar{\sigma}^{\,3}\, \mathcal{N}_{\rm NEIB}\, \dot{\mathcal{N}}_{\rm LyC}\, \rho_{\rm i}}{(20)^3\, \pi\, \alpha_{\rm B}\, m} \tag{4.12}$$

$$\gtrsim 5 \times 10^{11} \left(\frac{\mathcal{N}_{\rm NEIB}}{50} \right) \left(\frac{\dot{\mathcal{N}}_{\rm LyC}}{10^{49}\,{\rm s}^{-1}} \right) \left(\frac{\rho_{\rm i}}{10^{-20}\,{\rm g\,cm}^{-3}} \right)\,. \tag{4.13}$$

Evidently this is a prohibitive requirement on $\mathcal{N}_{\rm i}$, all the more so when one allows that the mass of neutral gas is likely to be even greater than the mass of ionized gas,

and so this will require additional SPH particles. Consequently we have to smooth the temperature gradient artificially across the ionization front. To demonstrate why this is necessary, we model a uniform density spherical cloud consisting of 10^6 pre-settled SPH particles. The total mass of the cloud is $M = 1000\mathrm{M}_\odot$, and the radius is $R = 1\mathrm{pc}$. At the centre of the cloud there is a single star emitting $\dot{\mathcal{N}}_{\mathrm{LyC}} = 10^{49}$ ionizing photons per second. There are no gravitational forces. We simulate this system in two ways: in Case A, the temperature gradient is unsmoothed; and in Case B, the temperature gradient is smoothed.

In Case A, the temperatures of the SPH particles are set as described in §4.4, and therefore there is an abrupt decrease in temperature across the ionization front. The simulation is terminated once the ionization front reaches the edge of the cloud. In Fig. 4.5a the smoothing lengths of all SPH particles are plotted against their distance from the ionizing source at time $t = 0.14\,\mathrm{Myr}$. Due to the abrupt temperature and pressure change across the ionization front, a gap is formed between the ionized and neutral regions. This gap prevents the ionization of new material from the neutral region during the expansion, and therefore the mass of the HII region does not increase (see Fig. 4.6a). This in turn alters the evolution of the radius of the HII region, as shown in Fig. 4.6b.

In Case B, the temperature gradient across the ionization front is smoothed. Well inside the HII region, and well outside the ionization front, we set the temperatures of the SPH particles as described in §4.4. However, in a layer of thickness $2h_{\mathrm{IF}}$ across the ionization front we linearly interpolate between the temperatures in the ionized and neutral regimes, i.e.

$$T(r) \;=\; \frac{1}{2}\left(T_{\mathrm{n}} + T_{\mathrm{i}}\right) + \frac{r - r_{\mathrm{IF}}}{2h_{\mathrm{IF}}}\left(T_{\mathrm{n}} - T_{\mathrm{i}}\right),\ |\mathbf{r} - \mathbf{r}_{\mathrm{IF}}| < h_{\mathrm{IF}}. \tag{4.14}$$

Here h_{IF} is the smoothing length of the local evaluation point on the ionization front, and r_{IF} is its radius. In this case, the transition between the two temperature regimes is continuous (see Fig. 4.5b). Crucially, this allows new neutral material to be ionized (see Fig. 4.6a), and the expansion of the HII region now follows the analytical solution (Eqn.2.25) rather closely.

We chose linear interpolation for the sake of simplicity. As we see in the test simulations of Chapter 5, the code predicts the known analytical solutions accurately, and

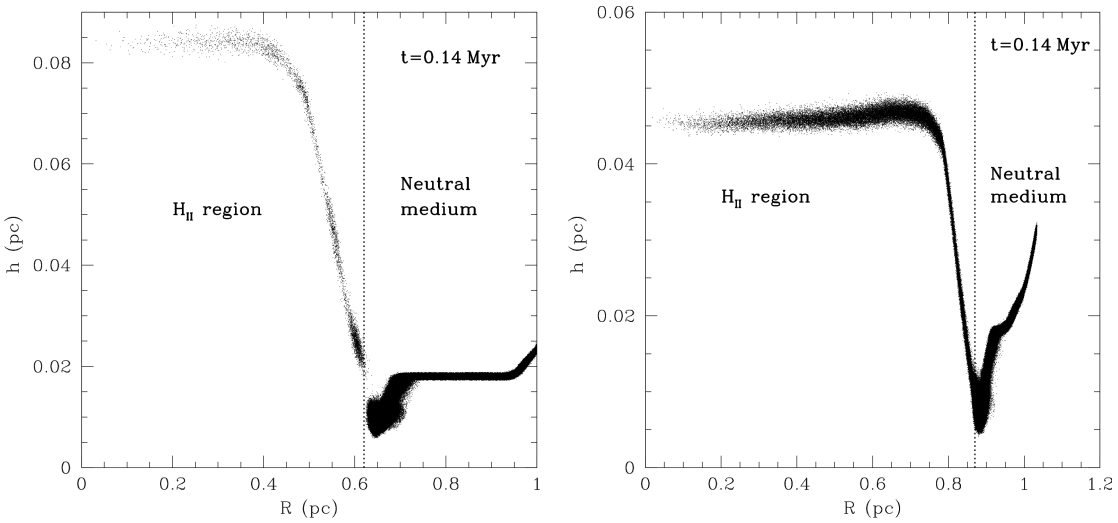

Figure 4.5: (*a*) The smoothing length of all 10^6 particles are plotted as a function of their distance from the star at $t = 0.14\,\mathrm{Myr}$ for Case A. Each point represents an individual SPH particle. The ionization front is located at $r_{\mathrm{IF}} \sim 0.63\,\mathrm{pc}$ away from the star. A gap between the ionized and neutral regimes is formed due to the discontinuous transition in temperature. (*b*) The smoothing lengths of the particles are plotted as a function of their distance from the star for Case B. Although the snapshot is taken at the same time ($t = 0.14\,\mathrm{Myr}$), the position of the ionization front is further from the star, at $r_{\mathrm{IF}} \sim 0.87\,\mathrm{pc}$. The transition between the two regimes is continuous now.

therefore we can demonstrate that using another function for temperature interpolation will not alter the results.

Several other authors have encountered the same problem in the past. Kessel-Deynet & Burkert (2000) smooth the ionization fraction over a distance of the order of one local smoothing length at the position where the ionization front is located. Krumholz et al. (2007) considers the same problem and constructs a region in which a similar procedure is followed.

4.7 TECHNICAL PARAMETERS

In the applications presented in this Thesis, we call the routine described in this chapter every 8 times the smallest timestep of the simulation (as discussed in §3.6). We find that this calling frequency compromises both the overall speed of each simulation and the accuracy of the results.

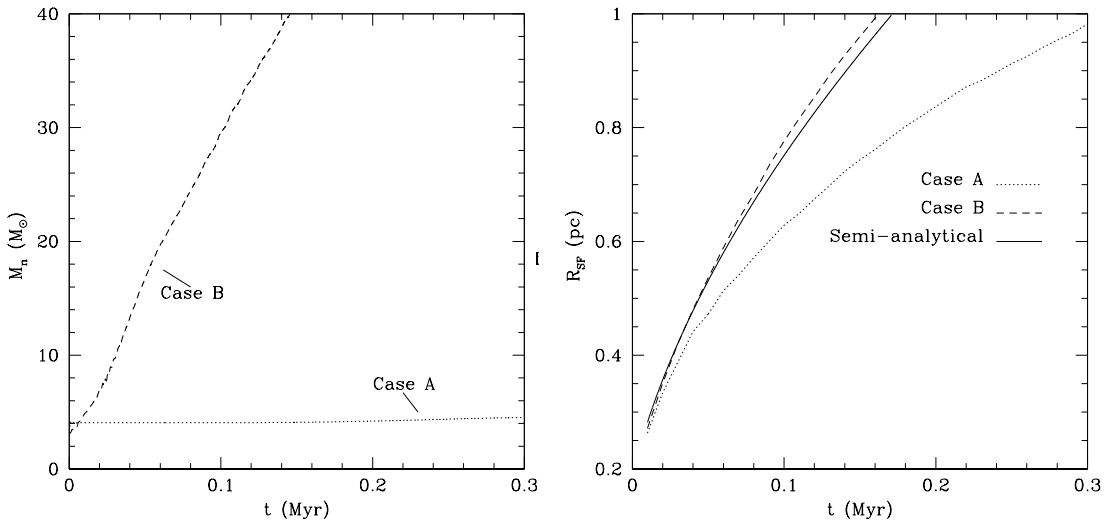

Figure 4.6: (a) Growth of mass of the HII region against time. In both cases we measure the mass of the gas that is completely ionized ($T_{\rm i} = 10^4\,{\rm K}$). Clearly in Case B new mass is ionized while in Case A the mass is almost constant. (b) The radius of the shell is plotted against time, for both cases A and B along with the semi-analytical solution (Eqn.2.27). The evolution of the HII region in Case A is in substantial disagreement with Eqn.(2.27), while in Case B the HII region expands according to Eqn.(2.27).

Furthermore, spherically symmetric tests showed convergence with $\ell_{\rm MAX}$ as low as 7. Higher level of accuracy can be used in more complicated cloud structures. The architecture of the algorithm allows rays to split up instantly to more than one level of refinement (i.e. a ray at $\ell = 4$ may split up directly to $\ell = 7$). This ensures that no clumps are left undetected, even in very irregular cases such as in applications of the Radiation Driven Compression and the expansion of an HII region in a fractal medium (Chapter 7). In addition, the original HEALPix routine is implemented to allow up to $\ell_{\rm MAX} = 13$ levels of refinement, but we find that for $\ell_{\rm MAX} > 11$ the memory cost is very high.

4.8 Chapter summary

In this chapter we have described the ray casting scheme we use in order to simulate the propagation of the ionizing radiation. This scheme uses HEALPix which generates uniformly distributed rays and we split them to higher levels of refinement as they emanate from the ionizing star. With this technique we create families of rays, along which we define a set of discrete evaluation points. At these evaluation points we

calculate the integral of Eqn.(2.11) using the trapezium method. We rotate the entire ensemble to reduce numerical artifacts due to the discretization in directions of rays, and we apply a binary chop routine in order to determine accurately the position of the ionization front. We smooth the temperature gradient artificially across the ionization front to avoid large pressure gradient differencies.

In the next chapter we will present test applications of this new algorithm.

5 Test applications

In this chapter we present the results of four different test applications in order to demonstrate the capabilities of the algorithm. In §5.1 we describe the initial conditions we use to perform the simulations. In §5.2 we simulate a spherically symmetric, uniform-density non – self - gravitating cloud with an ionizing star at its centre; we perform this simulation with different total numbers of SPH particles in order to test convergence. In §5.3, we repeat this simulation with a much more massive cloud, and include the effect of self-gravity. The evolution is now well described by the semi-analytic solution derived in Chapter 2 (see Eqn.2.27). These applications show that the algorithm is able to reproduce the known analytical solutions. In §5.4 we show an example of the Vishniac and the Rayleigh-Taylor instability in a spherically symmetric expanding HII *region.*

5.1 INITIAL CONDITIONS

In all simulations presented in this chapter, the SPH particles are initially positioned randomly, and then settled to produce a uniform-density "glass". We do this in order to reduce the numerical noise in calculating the density of the cloud. For example, in Fig. 5.1 we plot the density profiles of a uniform-density spherical cloud with mass $M = 1000\,\mathrm{M}_\odot$ and radius $R = 1\,\mathrm{pc}$. Thus the density of this cloud is $\rho = 1.616 \times 10^{-20}\,\mathrm{g\,cm^{-3}}$. Figure 5.1a shows the density profile of the sphere with particles randomly distributed, while fig.5.1b shows the density profile of the glass sphere. The density is much better defined after settling.

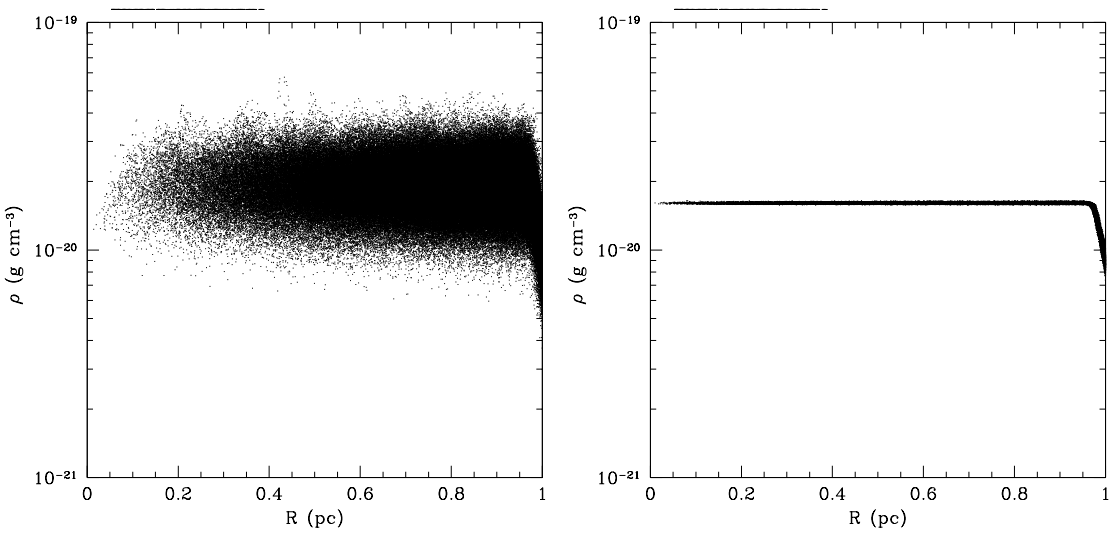

Figure 5.1: Density profiles of a sphere consisting of particles with randomly distributed positions (left) and a sphere consisting of particles settled to produce a "glass" (right). In both cases the density drops near the edge of the cloud due to the increase of the smoothing length h in finding the $\mathcal{N}_{\mathrm{NEIB}}$ neighbouring particles.

The temperature of the ionized gas is set to $T_{\mathrm{i}} = 10^4\,\mathrm{K}$. As we mentioned in §4.6, in a boundary layer between the ionized and neutral extremes, we smooth the temperature. The recombination coefficient into excited states only is taken to be $\alpha_{\mathrm{B}} = 2.7 \times 10^{-13}\,\mathrm{cm^3\,s^{-1}}$. The volume occupied by the ionizing star is neglected.

The parameters of all simulations are listed in Table 5.1. In this table, the first column gives the subsection in which the simulation is discussed, M is the mass of the cloud, R is its radius, T_{n} is the temperature of the neutral medium, X and Y are the fractions by mass of hydrogen and helium, respectively, μ_{n} and μ_{i} are the mean

molecular weights of the neutral medium and the ionized medium, respectively, $\dot{\mathcal{N}}_{\rm LyC}$ is the rate of emission of hydrogen ionizing photons from the exciting star, D is the distance of the exciting star from the centre of the cloud, $R_{\rm St}$ is the initial Strømgren radius, $\mathcal{N}_{\rm SPH}$ is the number of SPH particles used in the simulation, t_{ff} is the free fall time and $M_{\rm J}$ is the Jeans mass. For these test applications we limit the level of ray splitting to $\ell = 7$ so there is a maximum of $196,608$ rays arriving at the ionization front.

From the Jeans mass we see that all applications except §6.1 are gravitationaly unstable and provided that gravitational forces are taken into account and there is no contribution due to ionization they will free fall in an t_{ff} forming stars.

Table 5.1: This table is a summary of the parameters used in all test applications.

Application	$M\,(\mathrm{M}_\odot)$	$R\,(\mathrm{pc})$	$T_{\rm n}\,(\mathrm{K})$	X	Y	$\mu_{\rm n}$	$\mu_{\rm i}$	$\dot{\mathcal{N}}_{\rm LyC}\,(\mathrm{s}^{-1})$
§4.6	1000	1	10	0.7	0.3	2.35	0.678	10^{49}
§5.2	1000	1	10	0.7	0.3	2.35	0.678	10^{49}
§5.3	1.5×10^5	14.6	10	0.7	0.3	2.35	0.678	10^{49}
§7.1	300	1	100	0.7	0.3	2.35	0.678	10^{49}
§6.1	20	0.5	100	1	0	1	0.5	3.2×10^{48}

$D\,(\mathrm{pc})$	$R_{\rm St}\,(\mathrm{pc})$	Self-gravity	$\mathcal{N}_{\rm SPH}$	$t_{ff}\,\mathrm{Myr}$	$M_{\rm J}\,\mathrm{M}_\odot$
0	0.189	OFF	10^6	0.96	0.82
0	0.189	OFF	$3, 6, 10, 20\times10^5$	0.96	0.82
0	1.43	ON	10^7	4.4	3.75
0.4	0.42	OFF	10^6	1.76	45
3.5	–	ON	3×10^5	4.82	219

5.2 Spherically symmetric expansion of an Hii region in a non–self-gravitating uniform-density cloud

In this application, we create a uniform-density spherical cloud having mass $M = 1000\,\mathrm{M}_\odot$, initial radius $R = 1\,\mathrm{pc}$, and hence initial density $\rho_{\rm n} = 1.6\times10^{-20}\,\mathrm{g\,cm^{-3}}$. An ionizing source is placed at the centre of the cloud (see Fig. 5.2), and emits ionizing photons at a constant rate $\dot{\mathcal{N}}_{\rm LyC} = 10^{49}\,\mathrm{s^{-1}}$. Using Eqn.(2.12), the initial Strømgren radius is $R_{\rm St} = 0.189\,\mathrm{pc}$. The neutral gas is assumed to be at $T_{\rm n} = 10\,\mathrm{K}$. There are no gravitational forces. We need to calculate the radius $R_{\rm IF}$ of the ionization front

and the radius $R_{\rm SF}$ of the shock front to compare our algorithm with the theoretical expressions discussed in Chapter 2.

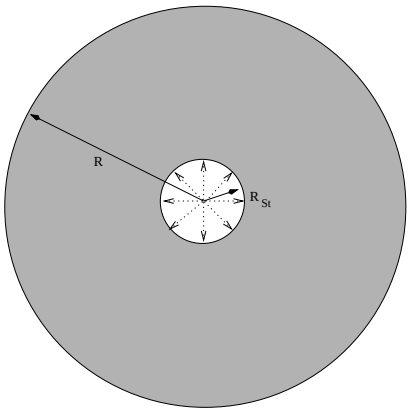

Figure 5.2: Profile of the model used in the tests described in §5.2 and §5.3

The radius $R_{\rm IF}$ is determined by finding the distance of the particles from the ionizing source which have temperatures in the range $\left(0.98T_{1/2},\, 1.02T_{1/2}\right)$, where $T_{1/2} = (T_{\rm i} + T_{\rm n})/2$. The radius $R_{\rm SF}$ is determined by finding the most distant particle from the source which has radial outward velocity $v_{\rm r} > 0.1\,{\rm km\,s^{-1}}$ and density $\rho > 1.1\rho_{\rm n}$. The second condition is necessary because particles near the edge of the cloud move outwards due to the thermal pressure gradient there, long before they are overrun by the shock front. The factor 1.1 is to accommodate numerical noise in the SPH estimate of the density of a particle.

In order to establish that our simulations are converged, we evolve this configuration using different numbers of SPH particles: $\mathcal{N}_{\rm SPH} = 3 \times 10^5,\ 6 \times 10^5,\ 10^6,$ and 2×10^6. We terminate the simulations when the ionization front reaches the edge of the cloud.

In Fig. 5.3a we plot the average radius of the ionization front, $R_{\rm IF}$, against time for all four simulations. We see that the curves converge for $\mathcal{N}_{\rm SPH} \gtrsim 10^6$. In Fig. 5.3b we plot the radius of the ionization front, $R_{\rm IF}$, and the radius of the shock front, $R_{\rm SF}$, against time, for the simulation performed with $\mathcal{N}_{\rm SPH} = 2 \times 10^6$ SPH particles. We also plot the numerical solution of the semi-analytic approximation for comparison. In Fig. 5.3c and Fig. 5.3d we plot the respective errors of Fig. 5.3a and Fig. 5.3b.

In general, we find that the Spitzer solution (Eqn.2.21) predicts the radius of the ionization front well, whereas the semi-analytic solution (Eqn.2.27) predicts the position of the shock front. The advantage of the semi-analytic solution is that it can also be used to treat situations in which the self-gravity of the gas is important, as we show

in §5.3.

Figure 5.4 shows four column density plots of the clouds simulated here with different numbers of SPH particles. The snapshots were taken at $t = 0.25\,\mathrm{Myr}$. The filamentary structures are attributable to a Vishniac-type instability and appear to be converged.

5.3 Spherically symmetric expansion of an Hii region in a self-gravitating uniform-density cloud

In this simulation self-gravity is taken into account, but with the following two modifications. First, once the radius of the shock front has been determined (as described in §5.2), we neglect the gravitational acceleration of all the SPH particles outside this radius. This is to prevent infall of the undisturbed neutral gas. Otherwise the outer parts of the cloud are already falling quite rapidly towards the centre by the time the shock front reaches them, and this complicates the interpretation of the dynamics. Secondly, we only take account of the radial component of the gravitational acceleration. We do this to suppress fragmentation of the shell, again in order to keep the dynamics of the shell as simple as possible (i.e. spherically symmetric).

In Fig. 5.5a we plot the position of the ionization front, the position of the shock front, and the semi-analytic approximation. In Fig. 5.5b we plot the difference between the radius of the shock front in the simulation, and the semi-analytic solution. We see that the position of the shock front agrees very well with the semi-analytic approximation. Finally, in Fig. 5.6 we plot a cross-section column density sequence of the evolution of the cloud.

5.4 Instabilities during the expansion of a spherically symmetric Hii region.

In order to reproduce, as closely as possible, the instabilities described in §2.4, we consider a non – self-gravitating uniform density cloud with mass $M = 1000\,\mathrm{M}_\odot$ and radius $R = 1\,\mathrm{pc}$. The density is therefore $\rho = 1.616 \times 10^{-20}\,\mathrm{g\,cm^{-3}}$. Beyond the

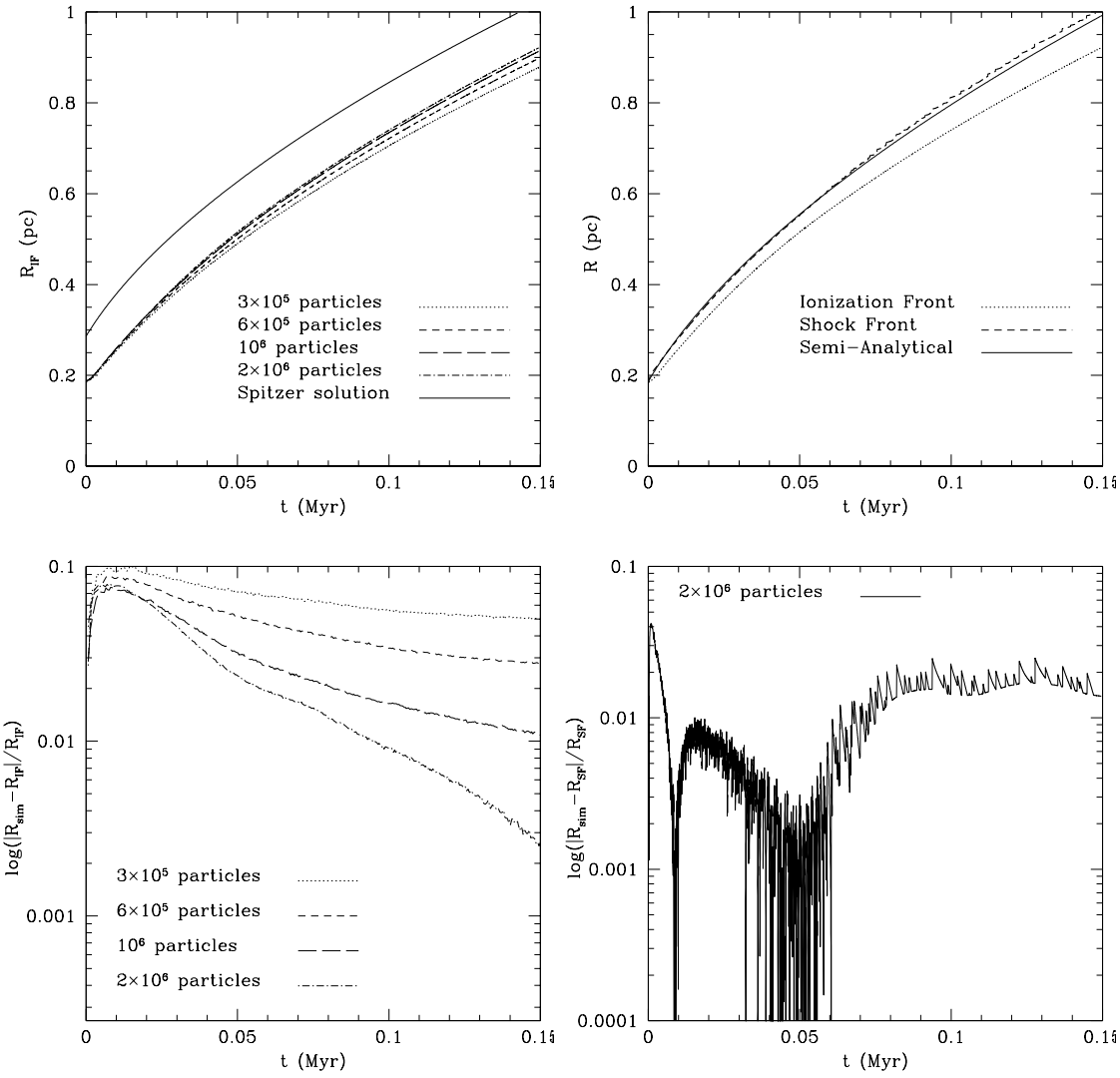

Figure 5.3: In the top left panel the radius of the ionization front is plotted against time for all four simulations in §5.2. The solid line is the Spitzer solution, displaced upwards by $R_{\rm IF} = 0.1\,{\rm pc}$ to avoid confusion. Convergence is achieved for $\mathcal{N}_{\rm SPH} > 10^6$. In the top right panel the radii of the ionization front and the shock front are plotted against time, for the simulation of §5.2 performed with $\mathcal{N}_{\rm SPH} = 2 \times 10^6$ SPH particles. The solid line is the semi-analytic solution described in Sec.2.3.2. In the bottom left panel the errors in determining the position of the ionization front between the simulation ($R_{\rm sim}$) and the Spitzer solution ($R_{\rm IF}$) are plotted. For $\mathcal{N}_{\rm SPH} > 10^6$ the average error is of order 1%. In the bottom right panel the error in determining the position of the shock front between the simulation and the semi-analytical approximation is plotted for $\mathcal{N}_{\rm SPH} = 2 \times 10^6$.

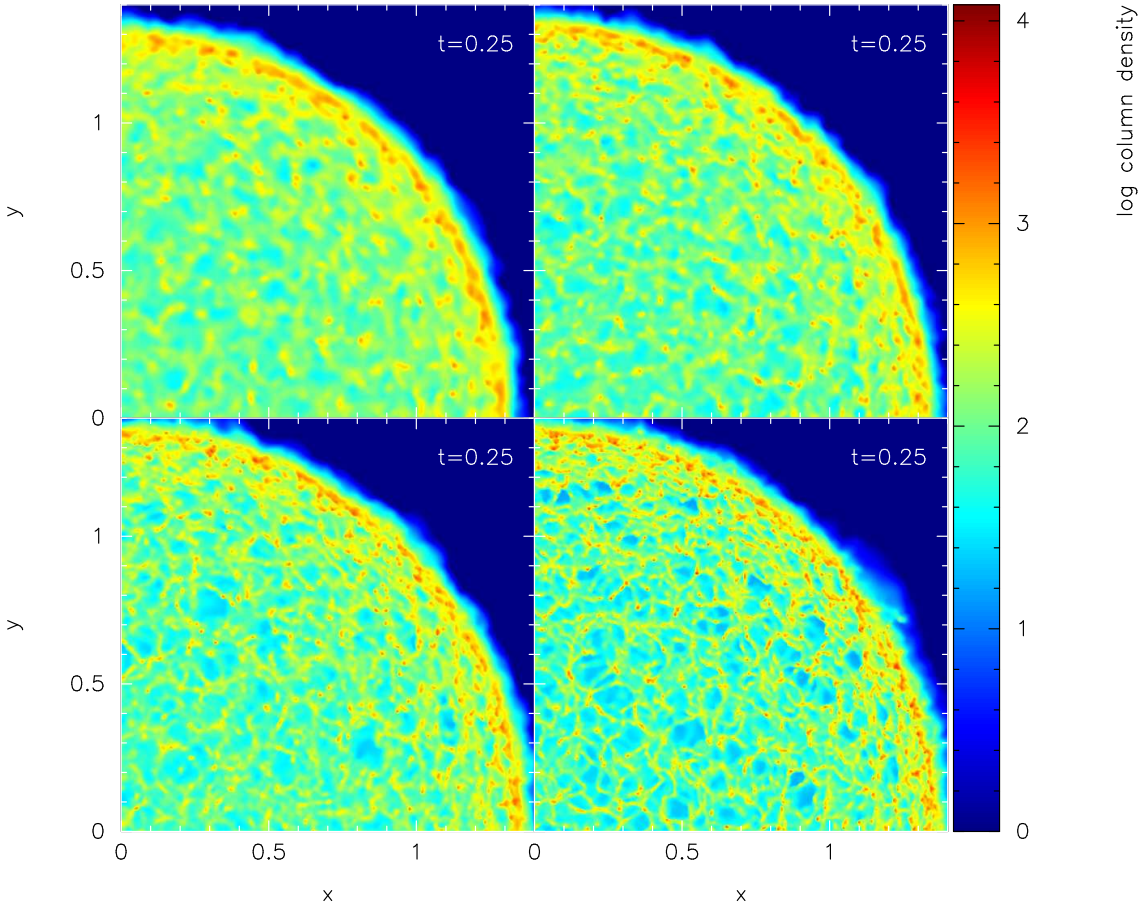

Figure 5.4: Column density plots of the clouds simulated with different numbers of particles: $\mathcal{N}_{\rm SPH} = 3 \times 10^5$ particles (top left), $\mathcal{N}_{\rm SPH} = 6 \times 10^5$ particles (top right), $\mathcal{N}_{\rm SPH} = 10^6$ particles (bottom left), $\mathcal{N}_{\rm SPH} = 2 \times 10^6$ particles (bottom right). The column density is in $\mathrm{M}_\odot\,\mathrm{pc}^{-2}$ $\left(\equiv 8.7 \times 10^{19}\,\mathrm{H}_2\,\mathrm{cm}^{-2}\right)$.

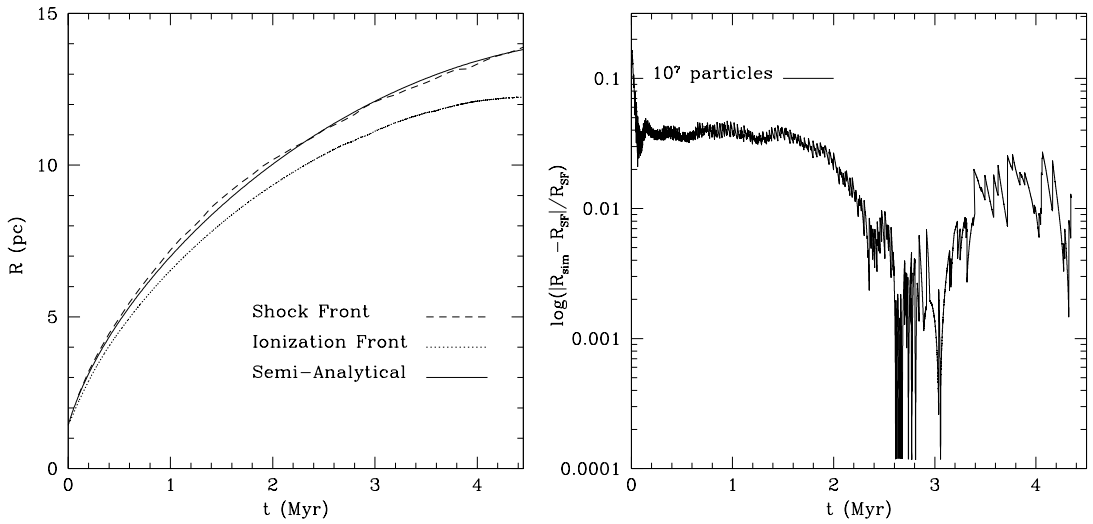

Figure 5.5: The left diagram shows the evolution of the shock front (dashed line) and the ionization front (dotted line) for the test described in §5.3. We plot Eqn.(2.27) for comparison (solid line). The evolution of shock front agrees with the prediction of our semi-analytical approximation. The right diagram shows the errors in calculating the position of the shock front between simulation ($R_{\rm sim}$) and semi-analytical approximation ($R_{\rm SF}$).

radius of the cloud there are no SPH particles. The cloud consists of pure molecular hydrogen which has temperature $T_{\rm n} = 10\,{\rm K}$. At its centre we switch on an ionizing star emitting $\dot{\mathcal{N}}_{\rm LyC} = 10^{49}$ photons per second. We consider that the temperature of the ionized gas is $T_{\rm i} = 10^4\,{\rm K}$, so the recombination coefficient into excited stages only is taken to be $\alpha_{\rm B} = 2.7 \times 10^{-13}\,{\rm cm^3\,s^{-1}}$.

From Eqn.(2.12) the initial Strømgren radius is $R_{\rm St} = 0.186\,{\rm pc}$. From Eqn.(2.21) the ionization front hits the edge of the cloud at $t_{\rm cl} = 0.17\,{\rm Myr}$. We evolve the HII region for $t = 0.32\,{\rm Myr}$, and we compare the structure of the shell for $t \leq t_{\rm cl}$ when it is prone to the Vishniac type instability, and $t > t_{\rm cl}$ when it is prone to the Rayleigh-Taylor type instability. Figure 5.7 shows the evolution of the mean radius of the ionization front along with Eqn.(2.21).

For $t \leq t_{\rm cl}$ the ionization front expands creating a dense shock front. At early times the shock front appears to be smooth. Soon, irregularities form which grow in time. Figure 5.8 shows a sequence of column density plots of the evolving HII region. The evolving shock front consists of oscillating peaks and valleys. Moreover, Fig. 5.9 which is a detailed image of Fig. 5.8d shows that the wavelength of these irregularities is

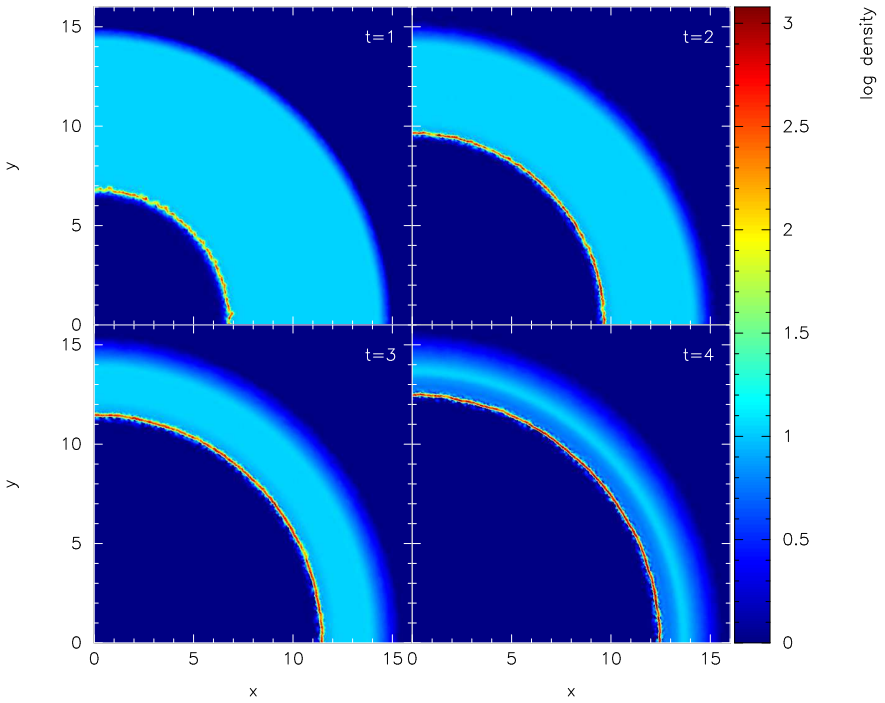

Figure 5.6: Cross section column density plots at times $t = 1\,\mathrm{Myr}$ (top left), $t = 2\,\mathrm{Myr}$ (top right), $t = 3\,\mathrm{Myr}$ (bottom left), $t = 4\,\mathrm{Myr}$ (bottom right). The column density is in $\mathrm{M_\odot\,pc^{-2}}$ $\left(\equiv 8.7 \times 10^{19}\,\mathrm{H_2\,cm^{-2}}\right)$.

comparable with the thickness of the shock front. The last two statements are good indicators of the Vishniac instability occurring.

For $t > t_{\mathrm{cl}}$ the ionization front hits the edge of the cloud, and since beyond this distance we have a vacuum, the expansion of the HII region accelerates. This is shown also in Fig. 5.7. We find that the density of the HII region is $\sim 10^{-21}\,\mathrm{g\,cm^{-3}}$, whereas the density of the shocked layer is $\sim 10^{-18}\,\mathrm{g\,cm^{-3}}$, i.e. about three orders of magnitude higher. Such a rarefied gas accelerating a denser gas can give rise to the Rayleigh-Taylor instability. Figure 5.10 continues the cross section column density sequence of Fig. 5.8. The pre-existing irregularities of the shock front are now magnified creating dense cometary knots which are being ionized at a slower rate than the rest of the medium (see also application §7.1). Behind these knots the material remains neutral creating either small fingers or small islands of molecular hydrogen (see Fig. 5.11). These are reminiscent of the cometary knots found in the Helix nebula (Fig. 2.7) and other so-called elephant trunks seen in the surroundings of OB stars.

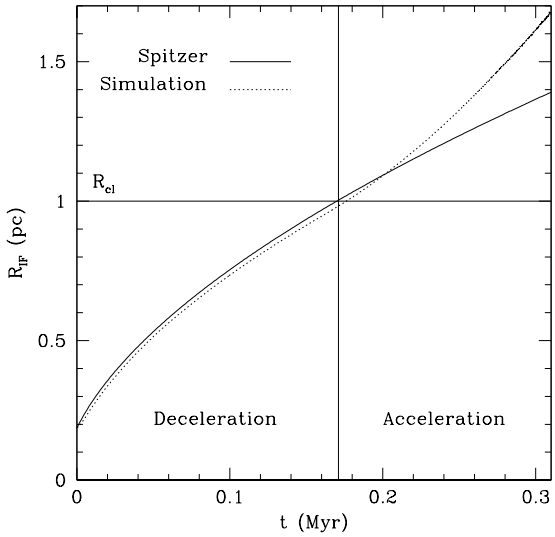

Figure 5.7: This figure shows the evolution of the position (pc) of the ionization front in time (Myr). The solid line is the Spitzer solution (Eqn.2.21) and the dotted line the simulation. For $t \leq 0.17\,\mathrm{Myr}$ the ionization front is decelerating whereas for $t > 0.17\,\mathrm{Myr}$ it is accelerating.

5.5 CHAPTER SUMMARY

In this chapter we have presented test applications in order to demonstrate the capabilities of the new algorithm. We have seen that in a spherically symmetric expansion of an HII region in a non–self-gravitating uniform density cloud the algorithm converges with increasing the total number of SPH particles. In addition, the Spitzer solution (Eqn.2.21) predicts the radius of the ionization front well, whereas the semi-analytic solution (Eqn.2.27) predicts the position of the shock front. We have also investigated the validity of (Eqn.2.27) when self-gravity is taken into account and we have found that the agreement with the simulation of an expanding HII region in an self-gravitating uniform-density cloud is very good. Finally, we explroed how the Vishniac and Rayleigh-Taylor instabilities develop and amplify in a spherically symmetric expanding HII region.

In the next chapter we will describe technical tests in modelling star formation triggered by radiation driven compression.

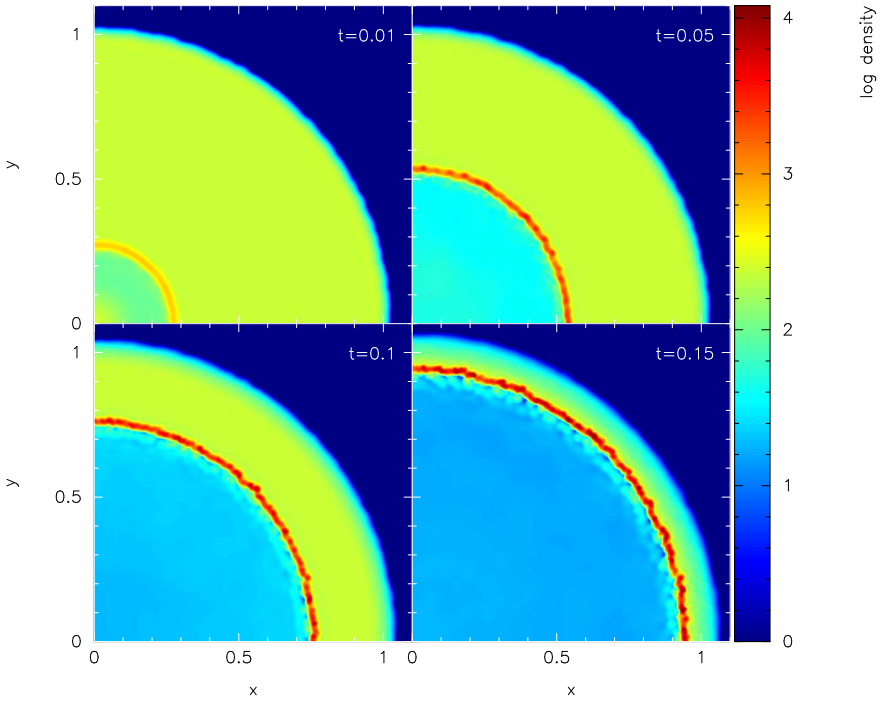

Figure 5.8: These column density cross section plots show the evolution of the ionization front for $t \leq 0.17\,\mathrm{Myr}$. The spatial coordinates are in pc. The column density is in $\mathrm{M}_\odot\,\mathrm{pc}^{-2}$ $\left(\equiv 8.7 \times 10^{19}\,\mathrm{H}_2\,\mathrm{cm}^{-2}\right)$. During the expansion oscillating "peaks" and "valleys" form suggesting that the Vishniac instability is occurring.

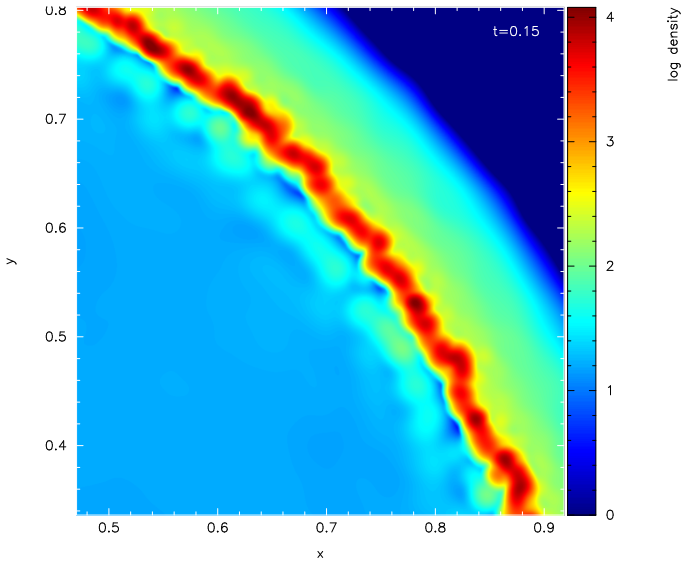

Figure 5.9: Detailed plot of Fig. 5.8d. The thickness of the shell is comparable with the wavelength of the irregularities.

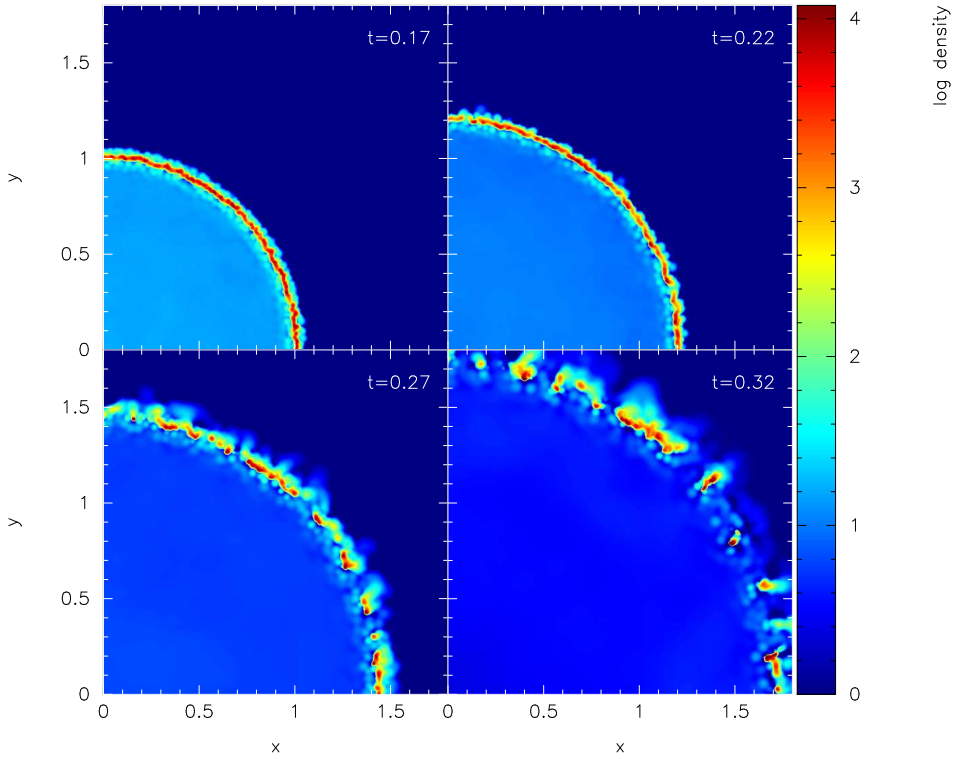

Figure 5.10: These column density cross section plots show the evolution of the ionization front for $t > 0.17\,\mathrm{Myr}$. The spatial coordinates are in pc. The column density is in $\mathrm{M}_\odot\,\mathrm{pc}^{-2}$ $\left(\equiv 8.7 \times 10^{19}\,\mathrm{H_2\,cm^{-2}}\right)$. In this accelerated phase the dense shell is being pushed by the rarefied medium resulting in the formation of the cometary knots.

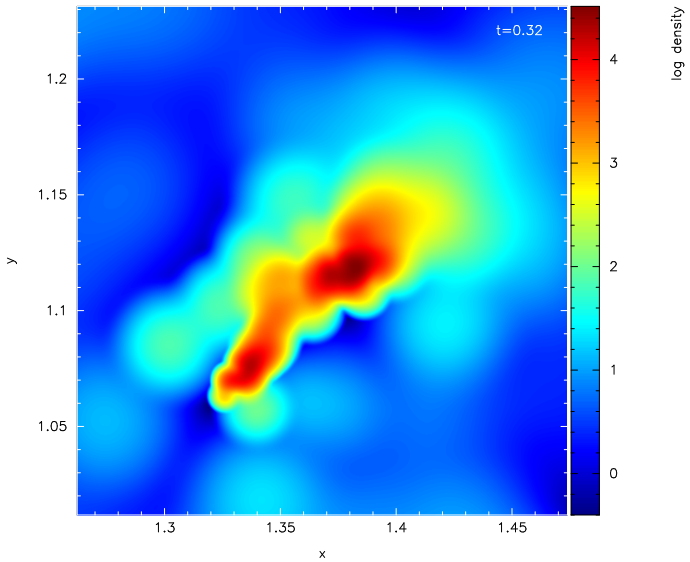

Figure 5.11: Detailed plot of Fig. 5.10d. Rayleigh-Taylor instability has created a dense knot which survives the passage of the ionization front. The material behind the head of the knot remains neutral. The ionizing star is at the origin of coordinates, i.e. beyond the bottom lefthand corner.

6 Radiation Driven Compression: technical tests

In the present chapter we perform a set of technical test simulations on the radiation driven compression mechanism and on the influence of the numerical noise in modelling triggered star formation. In particular, in §6.1 we repeat a simulation by Lefloch & Lazareff (1994) of a spherical clump as it is overrun by an expanding HII *region and we compare the results. In §6.2 we give a brief description of the properties of the spherical clumps and the initial conditions we use for the tests on the investigation of the numerical noise influence. These tests are discussed in §6.3. The results will be taken into account for the study of the mophological evolution of an isolated globule and to establish the conditions under which the globule can form stars, as it will be extensively discussed in the next chapter.*

6.1 RADIATION DRIVEN COMPRESSION

In this application we will attempt to repeat the simulation of radiation driven compression by Lefloch & Lazareff (1994 – hereafter LL94) and compare the results with those of our algorithm. The LL94 simulation is two dimensional and based on a grid code.

LL94 consider a uniform density spherical clump with mass $M = 20\,\mathrm{M}_\odot$ and radius $R = 0.5\,\mathrm{pc}$. They assume that it consists of pure atomic hydrogen (HI) which has temperature $T_\mathrm{n} = 100\,\mathrm{K}$ and sound speed $c_\mathrm{n} = 0.88\,\mathrm{km\,s^{-1}}$. This clump is surrounded by a warm neutral "intercloud" gas with temperature $T_\mathrm{w} = 10^4\,\mathrm{K}$ and sound speed $c_\mathrm{w} = 8.81\,\mathrm{km\,s^{-1}}$. A constant plane parallel flux $\Phi = 2.18 \times 10^9\,\mathrm{cm^{-2}\,s^{-1}}$ ionizes the cold gas, and the ionized particles have temperature $T_\mathrm{i} = 10^4\,\mathrm{K}$ and sound speed $c_\mathrm{i} = 12.5\,\mathrm{km\,s^{-1}}$.

In order to reproduce – as closely as possible – the LL94 simulation, we consider a uniform-density spherical clump, having mass $M = 20\,\mathrm{M}_\odot$, initial radius $R = 0.5\,\mathrm{pc}$, and hence initial density $\rho_\mathrm{n} \sim 2.6 \times 10^{-21}\,\mathrm{g\,cm^{-3}}$. We place an ionizing source a distance $D = 3.5\,\mathrm{pc}$ away from the centre of the cloud. The source emits ionizing photons at a constant rate $\dot{\mathcal{N}}_\mathrm{LyC} = 3.2 \times 10^{48}\,\mathrm{s^{-1}}$. Hence the number-flux of ionizing photons incident on the near side of the cloud is $\Phi \sim 2.18 \times 10^9\,\mathrm{cm^{-2}\,s^{-1}}$. Since $D \gg R$, the rays are approximately parallel (see Fig. 6.1).

Here, we also assume $X = 1$ instead of $X = 0.7$, i.e. pure hydrogen with $\mu_\mathrm{n} = 1$ and $\mu_\mathrm{i} = 0.5$. The neutral gas is assumed to be at $T_\mathrm{n} = 100\,\mathrm{K}$; therefore is sound speed is $c_\mathrm{n} = 0.9\,\mathrm{km\,s^{-1}}$. The simulation uses $\mathcal{N}_\mathrm{SPH} = 3 \times 10^5$ particles, $\ell_\mathrm{MAX} = 7$ levels of HEALPix refinement, and self-gravity is taken into account. The simulation is terminated at $t = 2.5\,\mathrm{Myr}$.

We note that from the outset the cloud is over-pressured, and left to its own devices would simply disperse on a timescale of $\sim 1\,\mathrm{Myr}$. As long as this timescale is much grater than the timescale of compression ($t \sim 0.2\,\mathrm{Myr}$) we do not include external medium in contrast with LL94. Including external medium would only support the rarefied material of the shadow of the cometary tail. In addition, it would increase the total computational cost of the simulation.

Figure 6.2 shows the evolution of the cloud. The ionizing flux propagates upwards and rapidly boils off the outer layers on the near side of the cloud. At $t \sim 0.036\,\mathrm{Myr}$

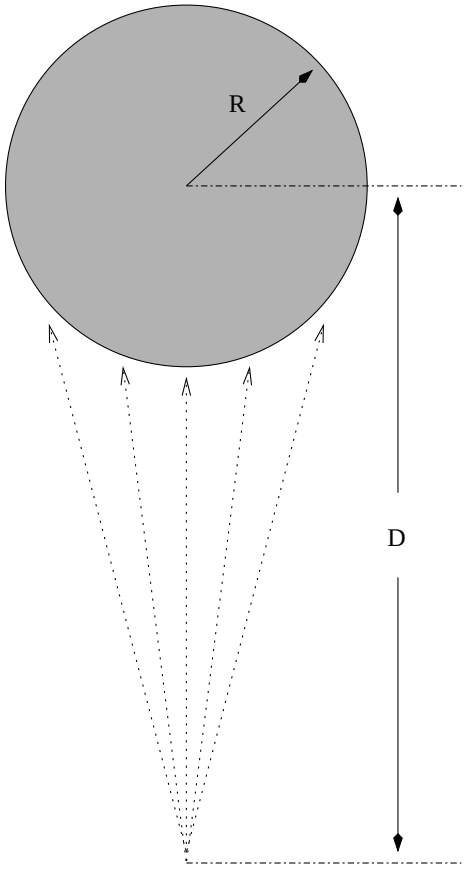

Figure 6.1: Profile of the model used in the test described in §6.1

(Fig. 6.2a) a shock front starts to compress the remaining neutral gas. At the same time, the north hemisphere starts to expand due to the thermal pressure of the atomic hydrogen. At $t \sim 0.13\,\mathrm{Myr}$ (Fig. 6.2b) a dense, prolate, approximately ellipsoidal core forms. By $t \sim 0.18\,\mathrm{Myr}$ (Fig. 6.2c), the prolate core has semi-major axis 0.08 pc and semi-minor axis 0.02 pc; its mass is $\sim 6\,\mathrm{M}_\odot$. It is therefore thermally sub-critical, and does not collapse to form a star. Instead it is steadily ablated by ionization. By $t \sim 0.21\,\mathrm{Myr}$ (Fig. 6.2d), the remnants of the cloud start to develop a cometary tail. By $t \sim 2.5\,\mathrm{Myr}$ (not shown on Fig. 6.2), the last vestiges of the cloud are ionized, and they are $\sim 28\,\mathrm{pc}$ from the ionizing star.

Figure 6.3 plots the total mass of neutral gas against time. The undulations seen at $t \sim 0.25\,\mathrm{Myr}$, and at $t \sim 0.5\,\mathrm{Myr}$ are acoustic oscillations, excited as the cloud responds to the increase in external pressure. At time $t > 1.1\,\mathrm{Myr}$ the dense head is more than 9 pc away from the star. At this distance the flux Φ arriving has dropped down to $3.3 \times 10^8\,\mathrm{cm^{-2}\,s^{-1}}$, which is about ten times weaker than the initial flux, whereas in LL94 it is constant everywhere. This means that the gas is evaporated

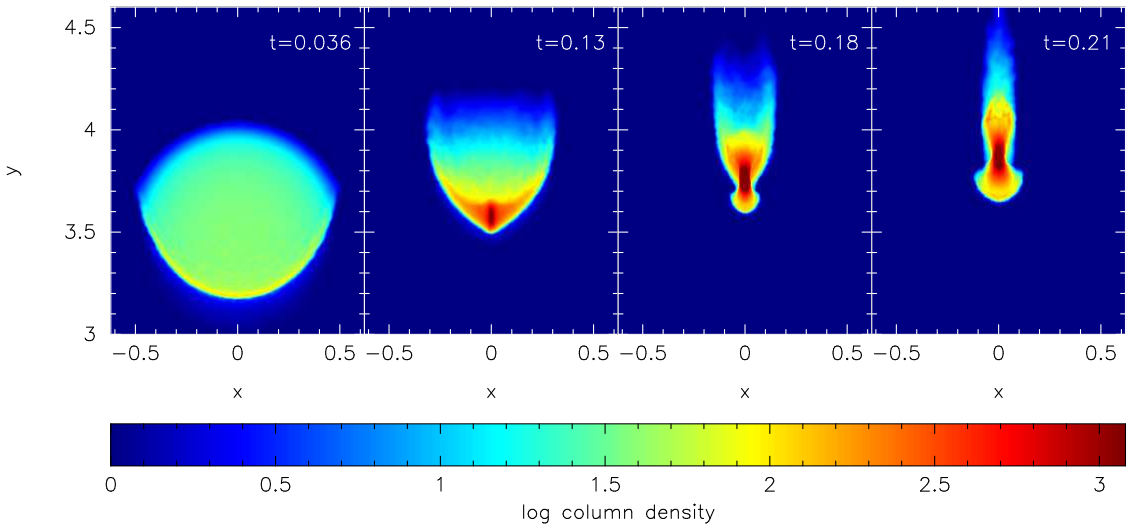

Figure 6.2: Column-density plots of radiation driven compression. Column-densities, Σ are measured in $M_\odot\,pc^{-2}$ $\left(\equiv 1.3\times10^{20}\,cm^{-2}\right)$. The spatial axes ($x$ and y) are labelled in parsecs, and times in Myr are given in the top right-hand corner of each frame.

at a slower rate than in LL94 and this results in the discrepancy between the two curves. Apart from this, the morphology of the curve in the simulations are reported here is very similar to the obtained by LL94.

This application shows that our algorithm is able to reproduce both the morphological structure and the evolution of the neutral mass in time very well comparing with the LL94 work. In the following section we describe the initial conditions used in test simulations to investigate the influence of the numerical noise in modelling triggered star formation during the radiation driven compression mechanism.

6.2 DESCRIPTION OF THE SIMULATIONS

6.2.1 THE BONNOR-EBERT SPHERE

The initial conditions we use are isothermal self-gravitating spheres in hydrostatic equilibrium, which are contained by external pressure. These spheres are known as "Bonnor-Ebert" spheres (hereafter 'BES') and were studied in detail by Bonnor (1956) and Ebert (1957). The density profile of a BES is a solution of the Lane-Emden equation (Lane 1870; Emden 1907). The main feature of this profile is that

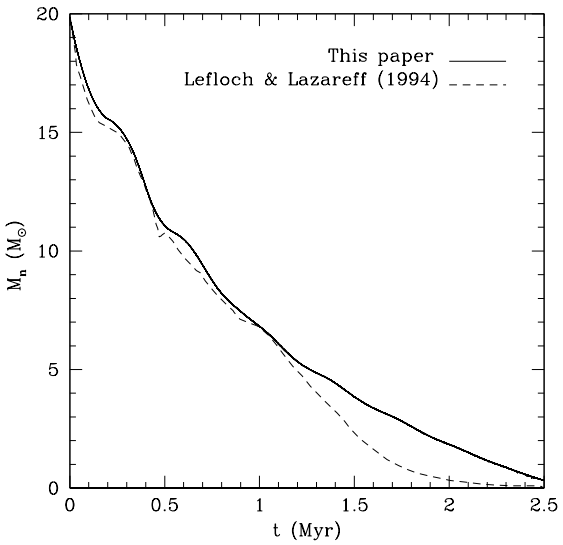

Figure 6.3: This diagram shows the mass of neutral gas as a function of time. The solid line represents the simulation discussed in §6.1, whereas the dash line is the simulation by Lefloch & Lazareff (1994). The discrepancy between our simulation and the simulation by Lefloch & Lazareff (1994) at time $t > 1.1$ Myr is due to the movement of the cloud further from the star, where the radiation flux drops in our model but stays constant in the Lefloch & Lazareff (1994) plane-parallel model.

as the distance from the centre of the BES increases, the density is approximately constant in the central region, and in the outer parts it decreases as $\rho \propto r^{-2}$.

We chose to use Bonnor-Ebert spheres as initial conditions due to their stability, and due to the existence of numerous observations of clumps with similar density profiles. These clumps are found in the interstellar medium and are embedded in HII regions. They are known as "Bok globules" (Bok & Reiley 1947) and are potential sites of star formation. An example of a well studied Bok globule is Barnard 68.

Consider an isothermal sphere in hydrostatic equilibrium. Its equation of state is

$$P = \rho \frac{k_{\rm B} T}{\mu m_p} = \rho c_{\rm s}^2 \,, \tag{6.1}$$

where P is the pressure, ρ is the density, $k_{\rm B}$ is the Boltzmann constant, T is the temperature, μ is the mean molecular weight, m_p is the proton mass, and $c_{\rm s}$ is the isothermal sound speed. In an isothermal sphere, $c_{\rm s}$ is assumed to be constant and uniform.

The mass $M(r)$ interior to radius r is given by

$$\frac{dM(r)}{dr} = 4\pi r^2 \rho(r)\,. \tag{6.2}$$

Since the sphere is in hydrostatic equilibrium,

$$\frac{dP}{dr} = -\rho(r)\frac{GM(r)}{r^2}\,, \tag{6.3}$$

where G is the gravitational constant. Rearranging Eqn.(6.3) for the mass $M(r)$, we obtain

$$M(r) = -\frac{r^2}{\rho G}\frac{dP}{dr} \tag{6.4}$$

or

$$\frac{dM(r)}{dr} = -\frac{1}{G}\frac{d}{dr}\left(\frac{r^2}{\rho}\frac{dP}{dr}\right)\,. \tag{6.5}$$

Combining Eqns.(6.1 - 6.3) and Eqn.(6.5) we obtain

$$\frac{1}{r^2}\frac{d}{dr}\left(\frac{r^2}{\rho}\frac{d\rho}{dr}\right) = -\frac{4\pi G\rho\mu m_p}{k_{\rm B}T}\,. \tag{6.6}$$

This is the Lane-Emden equation for an isothermal sphere.

We now introduce the dimensionless function $\psi(\xi)$ defined by

$$\rho = \rho_c e^{-\psi(\xi)}\,, \tag{6.7}$$

where ρ_c is the central density of the sphere. The function $\psi(\xi)$ is related to the gravitational potential (Banerjee et al. 2004). We also introduce the dimensionless radius ξ

$$\xi \equiv \frac{r}{R_c}\,, \tag{6.8}$$

where

$$R_c = \frac{c_s}{\sqrt{4\pi G\rho_c}}\,. \tag{6.9}$$

Using Eqns.(6.7-6.9), Eqn.(6.6) takes the dimensionless form

$$\frac{1}{\xi^2}\frac{d}{d\xi}\left(\xi^2\frac{d\psi}{d\xi}\right) = e^{-\psi(\xi)}\,. \tag{6.10}$$

To integrate Eqn.(6.10) we must impose the following boundary conditions

$$\psi(0) = 0 \tag{6.11}$$

$$\frac{d\psi(\xi)}{d\xi} = 0 \text{ at } \xi = 0\,. \tag{6.12}$$

Eqn.(6.11) follows immediately from Eqn.(6.7). Eqn.(6.12) follows from Eqn.(6.4) and the assumption that there is no central point mass (i.e. $M(0) = 0$).

Consider now that the sphere has a finite radius $R_{\rm B}$, where B denotes the bound. Therefore,

$$R_{\rm B} = \xi_{\rm B} R_{\rm c} \tag{6.13}$$

or

$$\xi_{\rm B} = \frac{R_{\rm B}}{R_{\rm c}}\,. \tag{6.14}$$

At $\xi_{\rm B}$ the pressure $P_{\rm B}$ is

$$P_{\rm B} = c_{\rm s}^2 \rho_{\rm B} = c_{\rm s}^2 \rho_{\rm c} e^{-\psi(\xi_{\rm b})}\,. \tag{6.15}$$

Since we require the cloud to be in hydrostatic equilibrium, we suppose that it is embedded in a medium which has pressure $P_{\rm ext} = P_{\rm B}$.

Bonnor (1956) examined the stability of a sphere whose density profile is a solution of Eqn.(6.10). He showed that for such a sphere there is a critical value of the dimensionless radius ξ, $\xi_{\rm CRIT}$, below which the sphere is stable. This value is $\xi_{\rm CRIT} = 6.451$. For $\xi_{\rm B} < \xi_{\rm CRIT}$ the cloud is stable while for $\xi_{\rm B} > \xi_{\rm CRIT}$ it is unstable.

To see how a Bonnor-Ebert sphere changes as $\xi_{\rm B}$ increases, we consider a BES with mass $M = 2\,{\rm M}_\odot$ consisting of molecular hydrogen with sound speed $c_{\rm s} = 0.19\,{\rm km\,s^{-1}}$. We solve Eqn.(6.10) numerically for different values of $\xi_{\rm B}$. Table 6.1 shows a summary of the results and Fig. 6.4 a plot of the solutions.

Table 6.1: Summary of the results for the BES with $M = 2\,{\rm M}_\odot$.

$\xi_{\rm B}$	$\frac{R_{\rm B}}{\rm (pc)}$	$\frac{P_{\rm ext}}{10^{-13}\,{\rm (Pa)}}$	$\frac{\rho_{\rm c}}{10^{-19}\,{\rm (g\,cm^{-3})}}$
5	0.105	4.77	1.01
6	0.099	5.13	1.66
6.451	0.097	5.16	1.99
7	0.096	5.13	2.42
8	0.094	4.94	3.25

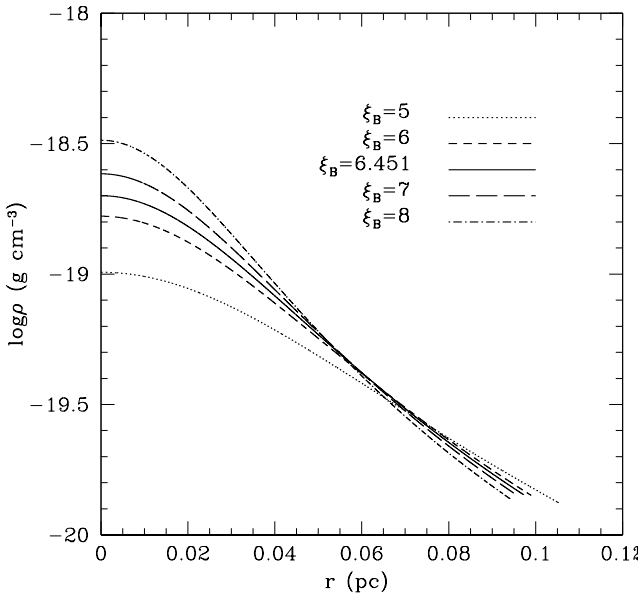

Figure 6.4: Density as a function of radius of a Bonnor-Ebert sphere with mass $M = 2\,\mathrm{M}_\odot$ for different values of ξ_B. The sound speed of the molecular hydrogen is $c_\mathrm{s} = 0.19\,\mathrm{km\,s^{-1}}$.

For $\xi_\mathrm{B} \ll \xi_\mathrm{CRIT}$ the external pressure is small and the cloud is extended. The density across the cloud is almost uniform and it is confined mainly by the external pressure. As ξ_B increases the external pressure increases. Its radius becomes smaller and its core density increases. For $\xi_\mathrm{B} = 6.451$ the external pressure has a maximum and the cloud is marginally stable. For values $\xi_\mathrm{B} > \xi_\mathrm{CRIT}$ it is unstable and collapses.

6.2.2 THERMODYNAMICS

When a clump is contracting its density increases. Its gravitational potential energy decreases and is converted into an increased kinetic and thermal energy. This implies an increase in the mean temperature of the clump which results in emission of radiation. During the collapse, the increase in temperature can be divided into two main phases.

In the *first phase* when the density is low, the clump is optically thin. Therefore cooling radiation (mainly from the dust) can escape and the gas stays approximately isothermal (at $T \sim 10\,\mathrm{K}$). In the *second phase*, the clump becomes optically thick and the cooling radiation is trapped. Therefore the gas heats up, approximately along an

adiabat. The transition between these two phases occurs when the density ρ of the cloud exceeds a critical value $\rho_{\rm CRIT}$.

In order to mimic the above processes and the corresponding change of thermal pressure, we use a barotropic equation of state of the form

$$P = c_{\rm s}^2 \rho \left[1 + \left(\frac{\rho}{\rho_{\rm CRIT}} \right)^{\gamma - 1} \right] . \tag{6.16}$$

Here P is the thermal pressure of the gas, ρ is the density of the gas, $\rho_{\rm CRIT}$ is the critical density above which the gas becomes approximately adiabatic, $c_{\rm s}$ is the isothermal sound speed at low density ($\rho \ll \rho_{\rm CRIT}$), and γ is the ratio of specific heats. From this equation we can calculate the corresponding temperature T using

$$T = T_{\rm iso} \left[1 + \left(\frac{\rho}{\rho_{\rm CRIT}} \right)^{\gamma - 1} \right] , \tag{6.17}$$

where $T_{\rm iso}$ is the temperature of the gas at low densities.

As an example, typical values are $\rho_{\rm CRIT} = 10^{-13}\,{\rm g\,cm^{-3}}$, $\gamma = 5/3$, and $c_{\rm s} = 0.19\,{\rm km\,s^{-1}}$ for molecular hydrogen at $T_{\rm n} = 10\,{\rm K}$ (see §2.1). When the gas becomes sufficiently dense ($\rho > 10^{-11}\,{\rm g\,cm^{-3}}$) and provided the densest particle and its neighbours are gravitationally bound, we consider that it will inevitably form a star (see §3.8). We therefore introduce a sink particle, to avoid following the dynamics further. Figure 6.5 shows a graphical display of Eqn.(6.17) using these typical values. Note that when a sink particle is created at $\rho \sim 10^{-11}\,{\rm g\,cm^{-3}}$ the temperature has only risen to $T \simeq 220\,{\rm K}$.

6.2.3 Initial conditions

The BES we will use in our tests in this chapter consists of molecular hydrogen. It has mass $M = 2\,{\rm M}_\odot$ and we choose $\xi_{\rm B} = 4$ so its radius is $R = 0.12\,{\rm pc}$. Since $\xi_{\rm B} < \xi_{\rm CRIT}$, this sphere is stable, and if it were not overrun by an HII region it would not change. The central density is $\rho_{\rm c} = 5.06 \times 10^{-20}\,{\rm g\,cm^{-3}}$ and the boundary pressure is $P_{\rm B} = 3.81 \times 10^{-13}\,{\rm Pa}$. Figure 6.6 shows the density as a function of radius for this BES.

To construct a BES we take a unit uniform density sphere ("parent" sphere) consisting

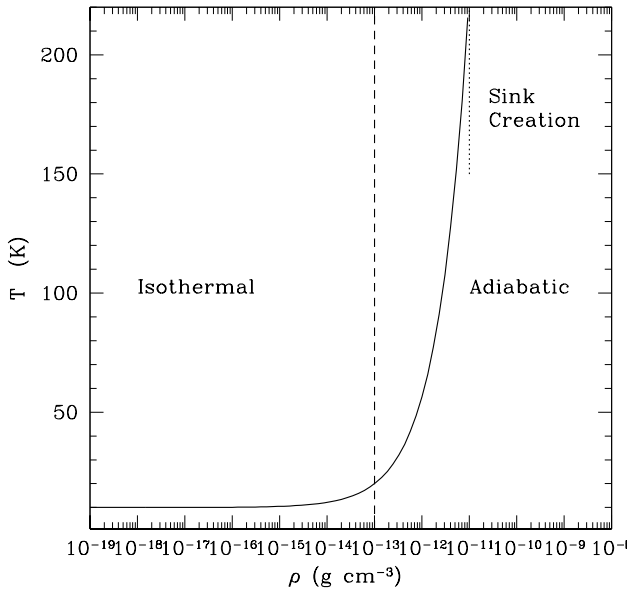

Figure 6.5: Plot of Eqn.(6.17). When $\rho > 10^{-11}\,\mathrm{g\,cm^{-3}}$ and provided the densest particle and its neighbours are gravitationally bound, we consider that stars will inevitably form.

of $\mathcal{N}_{\rm SPH}$ SPH particles and we solve numerically the Lane-Emden equation (Eqn.6.10) for the parent sphere. We then re-position the particles so as to reproduce as closely as possible the analytical density profile of the BES.

The BES in our tests is constructed with $\mathcal{N}_{\rm SPH} = 10^5$ SPH particles which correspond to 5×10^4 particles per solar mass or to $2 \times 10^{-5}\,\mathrm{M_\odot}$ per SPH particle. We use two different parent spheres: (i) with particles unsettled and (ii) with particles settled to form a "glass". We shall call the resultant Bonnor-Ebert spheres BES-u and BES-s, where u and s denote unsettled and settled respectively. Figure 6.7 shows the density as a function of radius of these two BES.

Furthermore, we introduce here the dimensionless parameter

$$\lambda \equiv \frac{D}{R} \tag{6.18}$$

where D is the distance of the centre of the BES from the source of ionizing radiation, and R is the radius of the BES (see Fig. 6.1).

In all tests, the incident flux at the core is initially $\Phi_{\rm D} = 1.45 \times 10^{11}\,\mathrm{cm^{-2}\,s^{-1}}$. We use the barotropic equation of state (Eqn.6.16) with $\rho_{\rm CRIT} = 10^{-13}\,\mathrm{g\,cm^{-3}}$. The sound

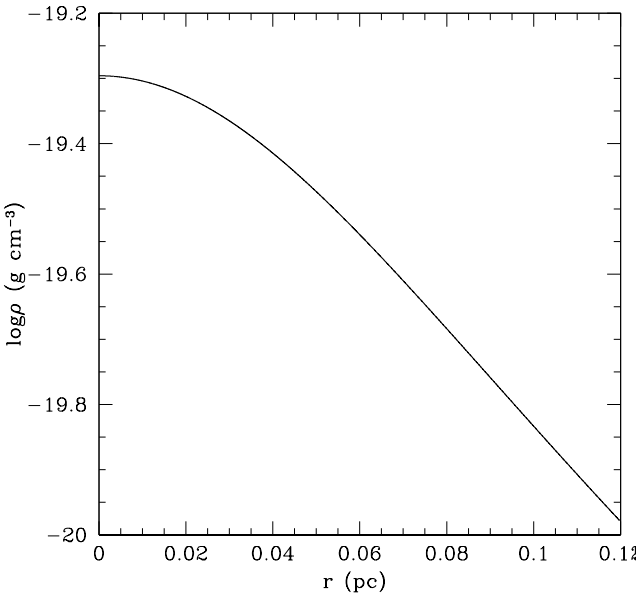

Figure 6.6: Density as a function of radius of the BES with $M = 2\,\mathrm{M}_{\odot}$ and $\xi_{\mathrm{B}} = 4$.

speed of the molecular hydrogen, c_{s}, for $\rho \ll \rho_{\mathrm{CRIT}}$ is taken to be $c_{\mathrm{s}} = 0.19\,\mathrm{km\,s^{-1}}$. This corresponds to a temperature of $T_{\mathrm{n}} = 10\,\mathrm{K}$. The temperature of the ionized gas is taken to be $T_{\mathrm{i}} = 10^4\,\mathrm{K}$. Self gravity is included. Sink particles are formed when the density reaches $\rho_{\mathrm{sink}} = 10^{-11}\,\mathrm{g\,cm^{-3}}$. The sink radius is $2h$, where h is the smoothing length of the sink particle.

6.3 Technical tests

In this section we present technical tests to explore the capabilities of our algorithm in modelling star formation in clumps ionized by an external source. In particular, we examine how the physical quantities of Bonnor-Ebert spheres, such as their morphological evolution and their star formation efficiency, are affected by the numerical noise of the calculations.

In contrast with the parameters of the simulations presented in the previous chapters, here we increase the maximum level of HEALPix refinement to $\ell_{\mathrm{max}} = 11$ which correspond to $\mathcal{N}_{\mathrm{RAYS}} \sim 5 \times 10^7$ rays. We also use $f_1 = 0.25$ and $f_2 = 0.5$ in order to have high accuracy in evaluating the integral of Eqn.(4.3) along each ray and high angular resolution, respectively. With these values the location and the morphological structure of the ionization front are captured very accurately.

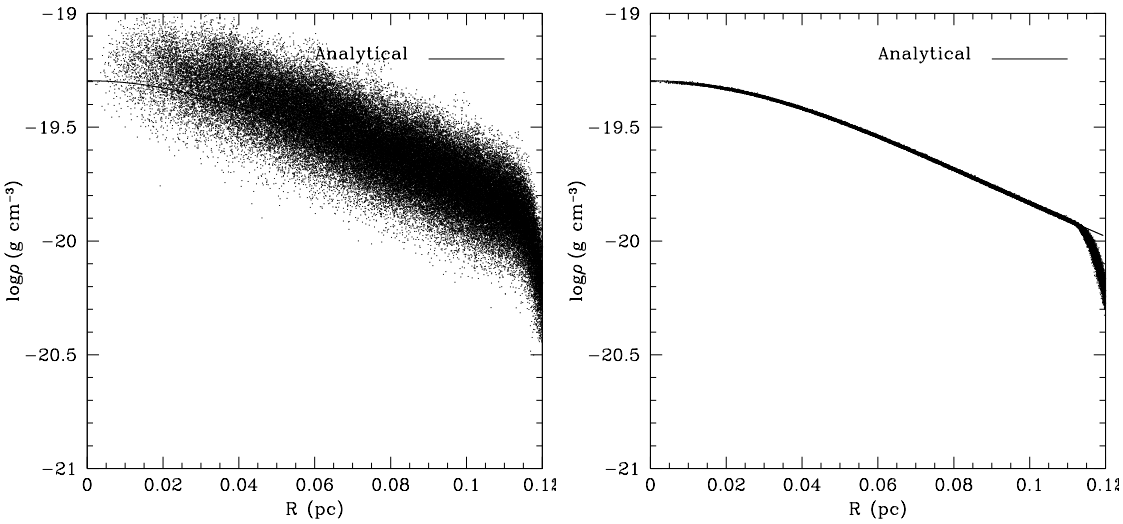

Figure 6.7: Density as a function of radius of the BES-u (left) and the BES-s (right). The solid line shows the analytical solution. The density of the central core is $\rho_{\rm c} = 5.06 \times 10^{-20}\,{\rm g\,cm^{-3}}$ and the sound speed of the molecular hydrogen is $c_{\rm s} = 0.19\,{\rm km\,s^{-1}}$.

In the following three sections we attempt to evaluate the influence of numerical artifacts on the results of our simulations. In §6.3.1 we consider a *settled* Bonnor-Ebert sphere and investigate how the outcome changes if the orientation of the Bonnor-Ebert sphere is changed (relative to the direction of the incident ionizing flux). In §6.3.2 we compare these results with these obtained using an *unsettled* Bonnor-Ebert sphere, but with the same total number of SPH particles ($\mathcal{N}_{\rm SPH} = 10^5$). Finally in §6.3.3 we present results obtained using an unsettled Bonnor-Ebert sphere with twice as many SPH particles ($\mathcal{N}_{\rm SPH} = 2 \times 10^5$).

Observations of the object B68 (Alves et al. 2001) show that the density profile of this clump fits very well the profile of a Bonnor-Ebert sphere with $\xi_{\rm B} \sim 6.9$. These observations also indicate small density fluctuations inside the globule. We note that the numerical noise seen in the case of the unsettled Bonnor-Ebert sphere cannot be compared with the true noise of the observations as long as the first one is not related with hydrodynamical fluctuations. In this regard a settled Bonnor-Ebert sphere reproduces a better astrophysical result compared with an unsettled Bonnor-Ebert sphere.

6.3.1 Numerical noise in settled Bonnor-Ebert spheres

In this test we consider a settled Bonnor-Ebert sphere ionized by an external source. To do this we use the BES-s described in §6.2.3. We create three additional settled Bonnor-Ebert spheres by rotating BES-s through three random angles about the $z-$, $x'-$, and $z''-$ axes with respect to the exciting star using Eqns.(4.3-4.8). We therefore have a set of four settled Bonnor-Ebert spheres, hereafter BES-s$_i$ where $i = 1, 2, 3, 4$. Thus any deviation in the results must be attributed to the discrete nature of the SPH particles representing the fluid.

As the clumps interact with the ionizing radiation, each one evolves in the following way. At early times the radiation erodes the borders of the hemisphere of the clump which faces towards the ionizing star. As the gas evaporates, the strong thermal pressure pushes the remains of this hemisphere and compresses it into a dense region inside the clump. When this region becomes sufficiently dense, it fragments and forms stars. We call this time the *sink creation time*, $t_{\rm SINK}$. The stars grow their masses rapidly until the ionization front passes through their vicinity, after which no more mass is accreted onto them. The remnants of the clump re-expand due to the thermal pressure of the neutral gas and then are ionized.

Table 6.2 is a summary of the results of these simulations. In this table $t_{\rm sink}$ is the time at which the first sink particle is formed, $M_{\rm n,s}$ is the neutral mass of the clump at the time $t_{\rm sink}$, $\mathcal{N}_{\rm s,tot}$ is the total number of sink particles formed, and $M_{\rm s,tot}$ is the total mass of all sink particles together. The valus of $M_{\rm s,tot}$ is measured at the end of each simulation ($t = 0.12\,$Myr.

Table 6.2: Summary of the results for the simulations of the BES-s$_i$

Simulation	$t_{\rm sink}$ (Myr)	$M_{\rm n,s}$ ($\rm M_\odot$)	$\mathcal{N}_{\rm s,tot}$	$M_{\rm s,tot}$ ($\rm M_\odot$)
BES-s$_1$	0.0455	1.54	3	0.59
BES-s$_2$	0.0475	1.52	5	0.7
BES-s$_3$	0.0461	1.53	3	0.82
BES-s$_4$	0.0462	1.52	9	0.64

From this table we see that $t_{\rm SINK}$ and $M_{\rm n,s}$ are approximately the same in all four simulations. Their values are $t_{\rm SINK} = 0.0465 \pm 0.001\,$Myr (2% variance), and $M_{\rm n,s} = 1.53 \pm 0.01\,\rm M_\odot$ (0.7% variance). On the other hand, the total number of sink particles formed varies significantly with $\mathcal{N}_{\rm s,tot} = 6 \pm 3$ (50% variance). Despite this, the total mass of the sink particles ($M_{\rm s,tot}$) remains relatively constant with $M_{\rm s,tot} =$

$0.7 \pm 0.11\,\mathrm{M}_\odot$ (16% variance). There is no correlation between the total number of sink particles formed ($\mathcal{N}_{\rm s,tot}$) and the total final mass ($M_{\rm s,tot}$) they gain.

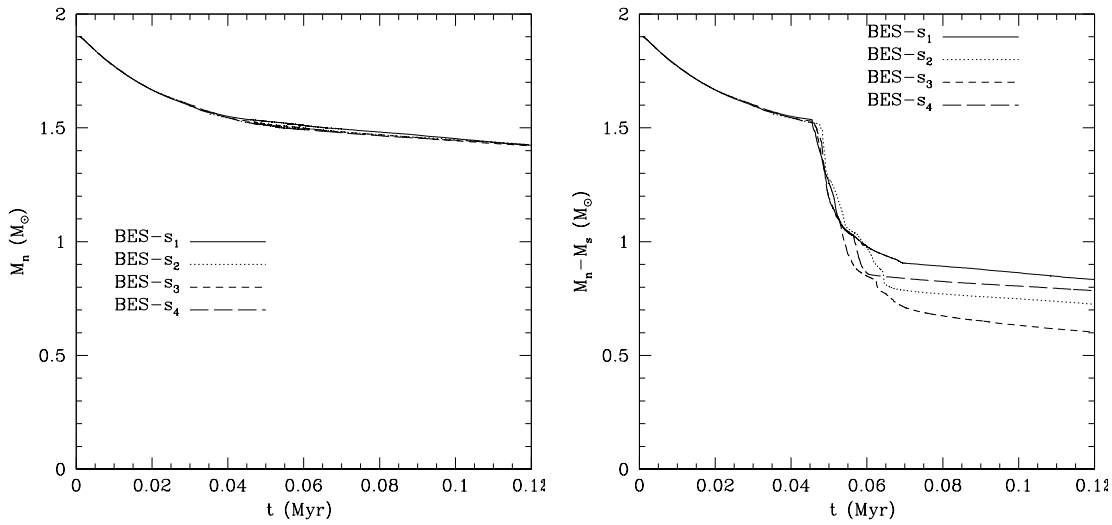

Figure 6.8: Left: Evolution of the neutral mass $M_{\rm n}$ versus time t for all BES-s$_i$. The curves are remarkably similar. Right: Evolution of the neutral mass of the clumps when account is taken of the contribution of the mass growth of sink particles. After the formation of sink particles, the curves start to differ between each other.

In the left graph of Fig. 6.8 we show how the neutral mass, $M_{\rm n}(t)$, decreases with time for each clump. We see that all four curves are remarkably similar. In the right graph we plot the same variable but when account is taken of the mass growth, $M_{\rm s}$, of sink particles, $M_{\rm n}(t) - M_{\rm s}(t)$. For $t < t_{\rm SINK}$ all four clumps start to collapse. At $t = t_{\rm SINK}$ sink particles are formed and evolved. Note that in all four cases the rate of growth of the sinks, once they form, is much greater than the rate at which neutral gas is ionized, until the ionization front passes at $t \sim 0.07\,\mathrm{Myr}$, when the rate of growth of the sinks falls to zero. The deviations between the curves of the right graph of Fig. 6.8 for $t > t_{\rm SINK}$ are due to differences in the evolution of the sink particles which are caused by numerical noise. To see why this is the case, we check the morphological evolution of the clumps, and more specifically the star forming region.

At $t \sim 0.03\,\mathrm{Myr}$ the ionizing radiation has compressed the borders of the clump which face towards the exciting star creating a flat shock front (see the top left panel of Fig. 6.9). The central region of the disk is dense and radially becomes more rarefied. As the radiation pushes it more (top right and bottom left panels of Fig. 6.9), the centre of the disk increases its density and fragments. In the borders of the disk, Rayleigh-Taylor instability occurs forming tentacles which point towards the exciting

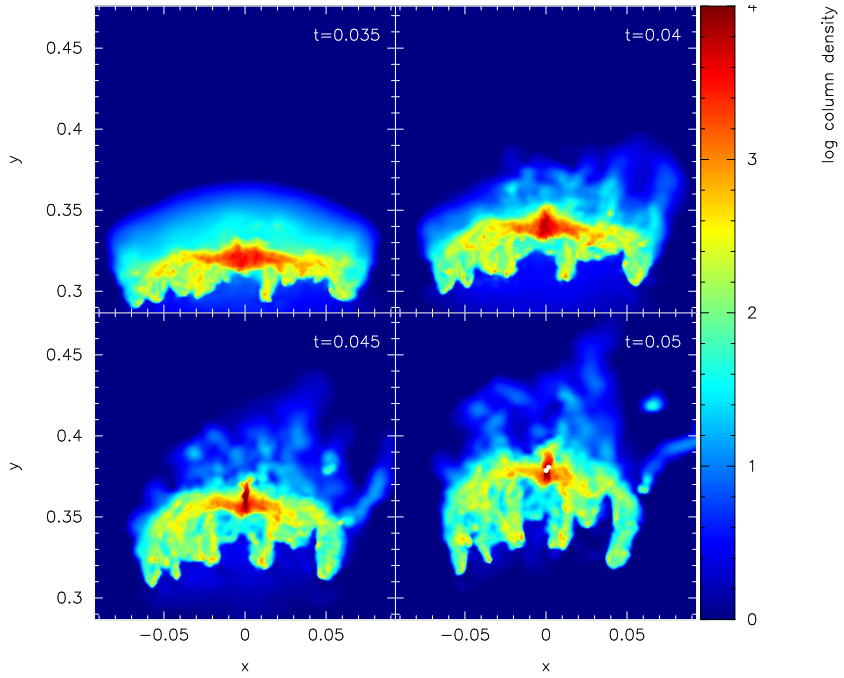

Figure 6.9: This column density plot shows a sequence for the BES-s_1 at t = 0.035, 0.04, 0.045, 0.05 Myr. At the centre of the head a dense column of neutral material forms which fragments and creates stars. The ionizing source is placed at the centre of the co-ordinate system, i.e. beyond the bottom of each snapshot.

star (bottom right panel of Fig. 6.9). Figure 6.10 shows column density plots of BES-s_i at $t = 0.048\,\mathrm{Myr} > t_{\mathrm{SINK}}$. The clumps all have very similar shapes, like a jelly-fish. However, a close-up of the central dense region shows how the numerical noise affects the star formation process. Figure 6.11 shows close-ups of these dense regions of Fig. 6.10. Here we see that although in all four clumps the star forming regions have the shape of a filament, they fragment differently in each case and this leads to differences in the sink particle creation and evolution. For example, at $t = 0.048\,\mathrm{Myr}$ one of them has formed a binary system (third snapshot from left to right in Fig. 6.11) whereas the rest of them have only formed a single star.

From this test we find that the total number of sink particles formed is very different in each Bonnor-Ebert sphere. However, their total final mass remains quite similar. We also find that the sink creation time, t_{SINK} and the jelly-fish morphology at t_{SINK} are very similar between all four clumps.

In the next two tests we will explore how these results are affected when the numerical noise is much higher.

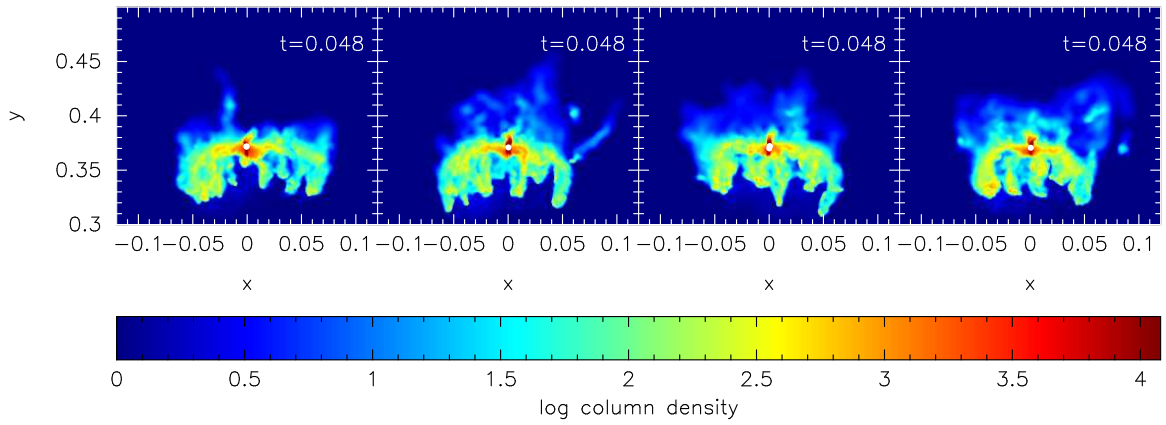

Figure 6.10: False-colour column-density plot of the BES-s$_i$ at $t \simeq t_{\rm sink}$. From left to write: BES-s$_{1,2,3,4}$. The morphologies between these spheres are remarkably similar. The ionizing star is located at the centre of the coordinate system, beyond the bottom of the frame.

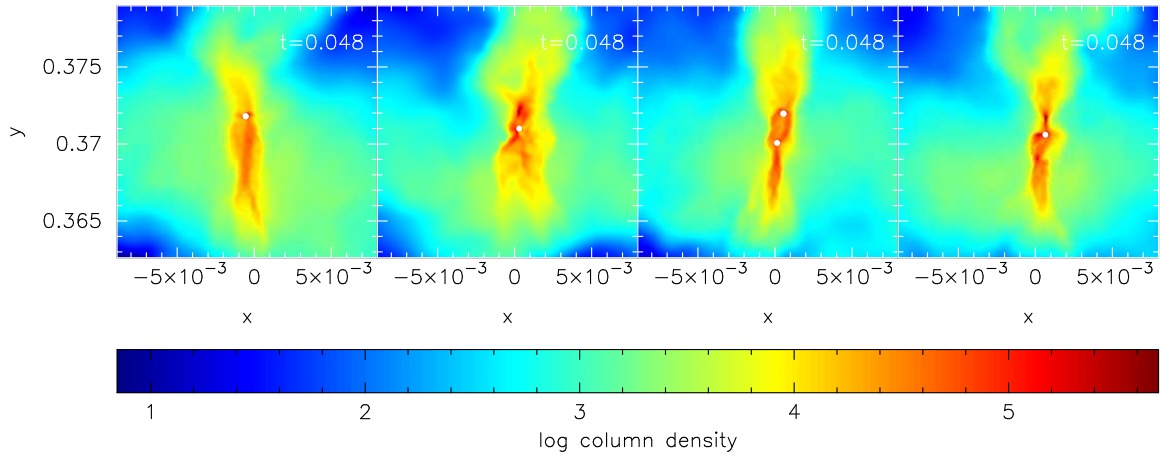

Figure 6.11: Close-ups of the star-forming regions in Fig. 6.10.

6.3.2 Comparison between a settled and an unsettled Bonnor-Ebert sphere

In this test we will compare our findings of the previous test described above with an unsettled Bonnor-Ebert sphere (hereafter BES-u). The numerical noise of an unsettled Bonnor-Ebert sphere is much higher than of a settled one. For instance, from Fig. 6.7 we see that at a given distance, R, from the centre of the clump, BES-u has $\log(\rho_{\rm max}/\rho_{\rm min}) \sim 0.8$, whereas BES-s has $\log(\rho_{\rm max}/\rho_{\rm min}) \sim 0.02$, where $\rho_{\rm max}$ and $\rho_{\rm min}$ are respectively the maximum and minimum values of the calculated SPH density at R. This simulation will show how our previous results are affected when the numerical noise is high.

In Table 6.3 we compare the key parameters obtained with BES-u against the means from runs BES-s$_i$ with $i = 1$ to 4. From Table 6.3 we see that the neutral mass remaining at $t_{\rm SINK}$, and the total mass of sinks at the end of the simulation, are both quite similar between BES-u and BES-s$_i$. However, the sink creation occurs significantly later in BES-u, relative to BES-s$_i$. In addition, Fig. 6.12 plots $M_{\rm n}(t)$ and $M_{\rm n}(t) - M_{\rm s}(t)$ between the simulations performed with BES-u and one of BES-s$_i$, namely BES-s$_1$.

Table 6.3: Comparison of the results for the simulations of BES-s$_i$ and the BES-u.

Simulation	$t_{\rm sink}$ (Myr)	$M_{\rm n,s}$ ($M_\odot$)	$M_{\rm s,tot}$ ($M_\odot$)
BES-s$_i$	0.0465 ± 0.001	1.53 ± 0.01	0.7 ± 0.11
BES-u	0.126	1.52	0.6

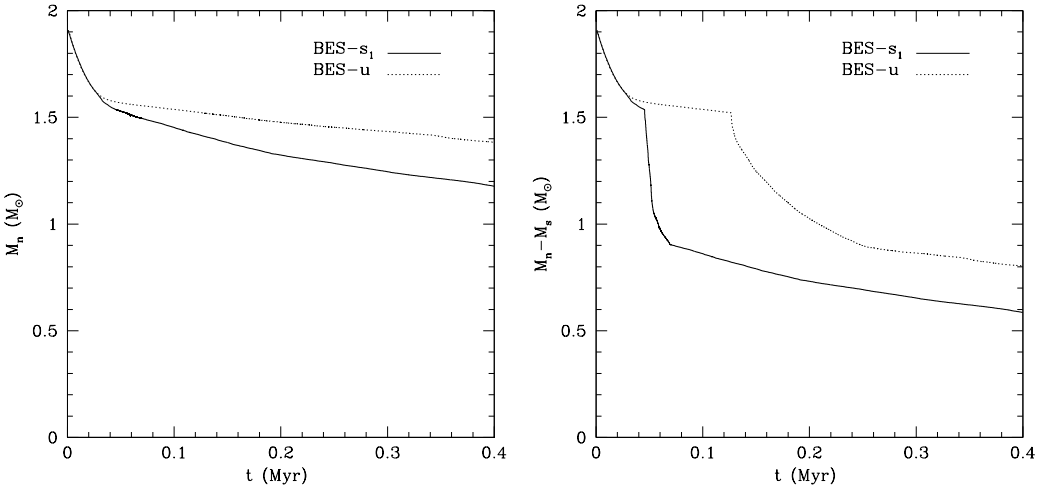

Figure 6.12: Mass of neutral diffuse gas against time for BES-s$_1$ and BES-u.

We note that the difference of the sink creation time between BES-u and BES-s$_i$ is *not* simply due to the contribution of extra turbulent pressure. We have calculated the effective sound speed, $c_{\rm s,eff}$ (Chandrasekhar 1951) of BES-u and then performed simulation with a settled BES (BES-s$_5$) having $c_{\rm s} = c_{\rm s,eff}$ for low densities. This simulation shows that both the evolution and the sink creation time of BES-s$_5$ are almost identical with the means of BES-s$_i$ and not with BES-u.

The numerical noise of BES-u prevents the SPH particles from arriving at the same time in the central region, and so the dense filamentary structure that we saw in §6.3.1 cannot be formed. Thus, the density behind the shock front in BES-u does not reach a sufficiently high value to create stars as early as in BES-s$_i$. To see why this is the case, in Fig. 6.13 we show a sequence of column density plots of BES-u with snapshots

taken at the same time as in Fig. 6.9. Here we see that the central region of BES-u at $t = 0.035, 0.04, 0.045$ Myr is more extended than of BES-s_1 and therefore more rarefied. The borders of BES-u are almost as dense as its centre and close to uniform density. The Rayleigh-Taylor instability here cannot form the tentacles and the jelly-fish structure that we saw in BES-s_1. At $t = 0.05$ Myr a growing dense condensation appears at the centre of the clump which eventually forms stars at $t = 0.126$ Myr.

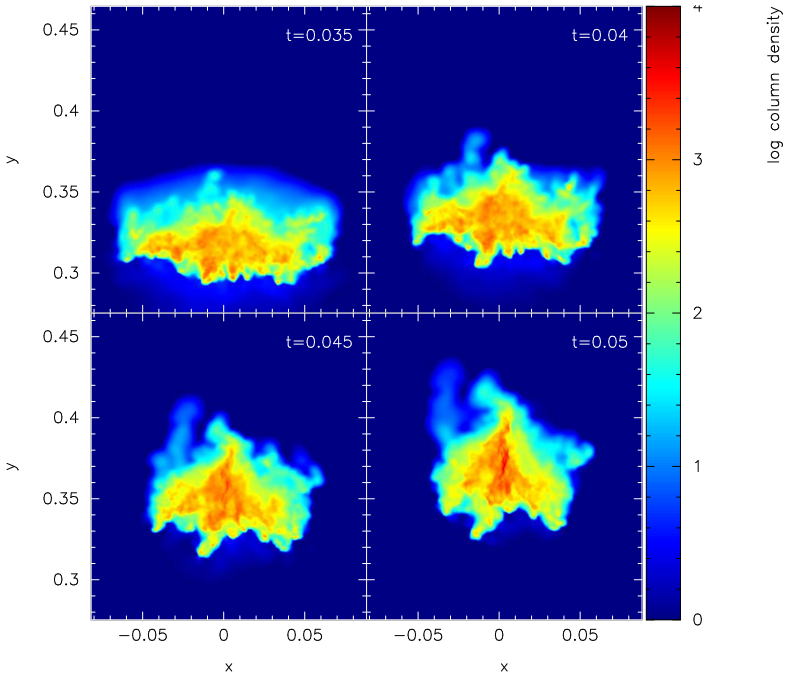

Figure 6.13: This column density plot shows a sequence for the BES-u at $t = 0.035, 0.04, 0.045, 0.05$ Myr. The numerical noise does not allow the particles to form a dense column in the centre. Increasing the particle resolution results in a jelly-fish shape (Fig.6.15).

From these simulations we see that $t_{\rm SINK}$ is significantly longer in BES-u and the morphological structure is significantly different from the means of BES-s_i. We suggest that all these deviations are due to the big difference between the numerical noise of the settled and unsettled Bonnor-Ebert spheres. We therefore expect to see a convergence between these physical quantities and characteristics if we increase the particle resolution of the BES-u and thus decrease its numerical noise. This test is described below.

6.3.3 Increasing the particle resolution

In this test we will compare the findings of the previous two tests with an unsettled Bonnor-Ebert sphere of higher particle resolution. As we saw in the last test above, the numerical noise of BES-u delays the sink particle formation by slowing down the increase in density at the centre of the clump. Here we perform a simulation with an unsettled Bonnor-Ebert sphere (BES-u_2) which has two times more resolution, thus 100,000 SPH particles/$M_\odot$ or $\mathcal{N}_{\rm SPH} = 2 \times 10^5$ particles in total. We evolve this clump until the first star is formed.

Figure 6.14 shows the evolution of neutral mass, $M_{\rm n}(t)$ of BES-s_1, BES-u, and BES-u_2 (left graph) as well as when account is taken of the mass growth of sink particles, $M_{\rm n}(t) - M_{\rm s}(t)$ (right graph). These plots show that the ionizing radiation erodes the same amount of neutral gas in time for BES-s_1 and BES-u_2. The quantity $t_{\rm SINK}$ is different between all three clumps. However, the difference of $t_{\rm SINK}$ between BES-s_1 and BES-u_2 is smaller than between BES-s_1 and BES-u. The mass of neutral gas of BES-u_2 at $t_{\rm SINK}$ is $M_{\rm n,s} = 1.42\,M_\odot$ which is quite similar with that of BES-s_i and BES-u.

Figure 6.15 shows a sequence of column density plots of BES-u_2 with snapshots taken at the same time as in Fig. 6.9 and Fig. 6.13. In this simulation, the SPH particles form a dense filament of neutral material at $t \sim 0.045\,$Myr, while the borders of the clump are more rarefied and are able to create tentacles similar to that of BES-s_1. Therefore, as we decrease the numerical noise the tendency to form a dense filamentary structure increases. The smaller the noise, the sooner this region reaches its maximum value. Eventually when a Bonnor-Ebert sphere is settled, the central density of this column is rapidly increased which leads to the formation of sink particles at early times.

6.4 Chapter summary

In this chapter we have repeated – as closely as possible – the simulation of radiation driven compression by Lefloch & Lazareff (1994) and we have found that our algorithm reproduced both the morphological structure and the evolution of the neutral mass in time very well.

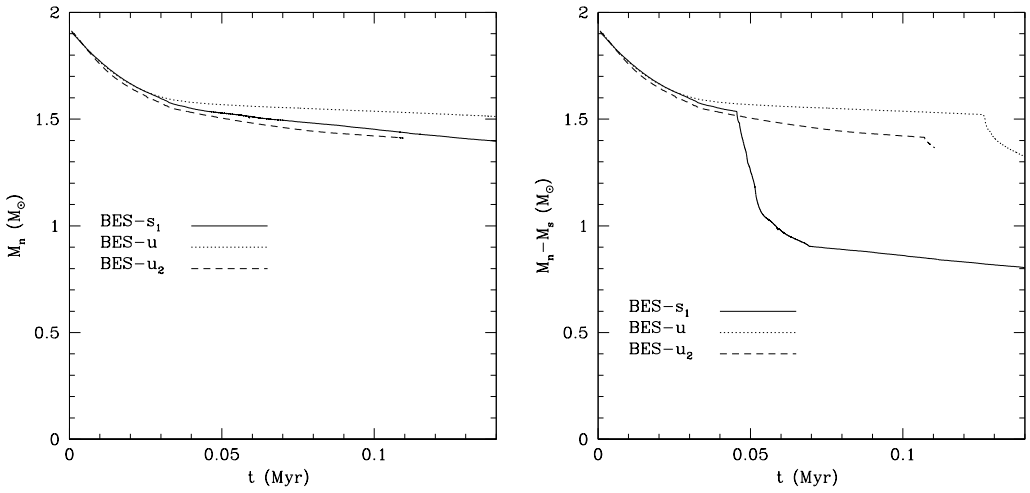

Figure 6.14: Left: Evolution of the neutral mass $M_{\rm n}$ versus time t for BES-s_1, BES-u, and BES-u_2. The high numerical noise of BES-u changes its evolution in comparison with the other two spheres where the noise is lower. Right: Evolution of the mass of each clump when account is taken of the mass growth of sink particles. Here we see that the difference of $t_{\rm SINK}$ between BES-s_1 and BES-u_2 is smaller than between BES-s_1 and BES-u.

We have also performed technical tests to explore how the behaviour of physical quantities depends on effects due to the numerical noise in simulations of a clump ionized by an external source. We did this in order to explore the ability of our algorithm to evaluate the star formation efficiency of the radiation driven compression mechanism, which is extensively discussed in the next chapter. Our findings can be summarized as follows:

The total number of sink particles formed, $\mathcal{N}_{\rm s,tot}$, depends strongly on the numerical noise of the calculations. This is because the dense star forming region, which appears during the compression of the clump, fragments differently even when the initial positions of the SPH particles are perturbed very little.

The sink creation time, $t_{\rm SINK}$, is altered only when the numerical noise is high, i.e. when the initial Bonnor-Ebert sphere is unsettled.

The total final mass of the sink particles formed, $M_{\rm s,tot}$, remains quite similar even when the initial Bonnor-Ebert sphere has not been settled.

The remaining neutral mass of the clump, $M_{\rm n,s}$, at $t_{\rm SINK}$ does not depend on the numerical noise.

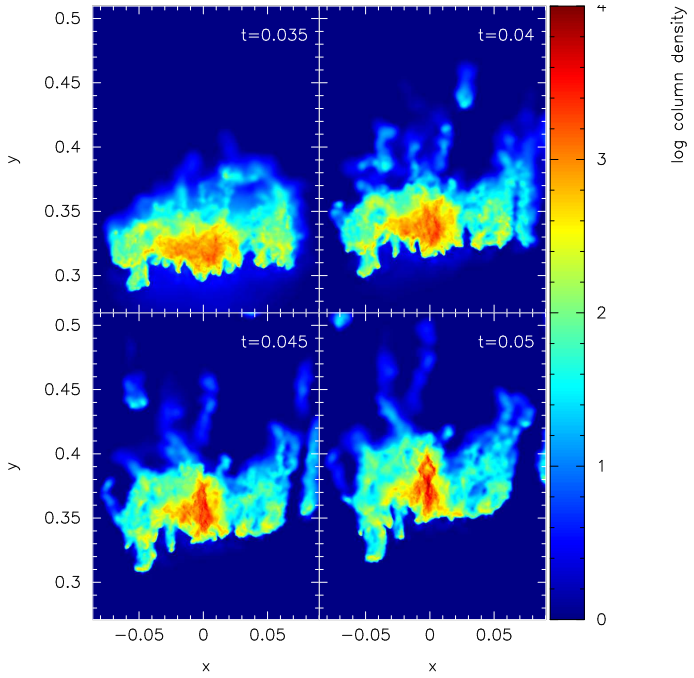

Figure 6.15: This column density plot shows a sequence for the BES-u_2 at t = 0.035, 0.04, 0.045, 0.05 Myr. As we increase the resolution the numerical noise decreases. Here the SPH gas particles create a dense column in the centre of the head. This area and at $t \sim 0.05$ Myr appears to be more compaque in contrast with Fig.6.13. Moreover, in this higher resolution simulation the sides of the cloud form tentacle-like structures similar to those seen in Fig.6.9

It is also interesting to note that when we increase the resolution in an unsettled Bonnor-Ebert sphere, as we saw in §6.3.3, its morphology converges to a settled Bonnor-Ebert sphere of lower particle resolution. Thus, with settled initial conditions we significantly reduce the calculation time and the total computational cost of our simulations leading to faster and more accurate results.

In the next chapter we will describe simulations of star formation triggered by radiation driven compression.

7 Astrophysical Simulations

In this chapter we present various astrophysical simulations including: i) the off-centre expansion of an HII region in a uniform-density medium (§7.1), ii) the expansion of an HII region in a fractal medium (§7.2), and iii) triggered star formation in the Radiation Driven Compression mechanism using stable Bonnor-Ebert spheres. In the particular case of the latter set of simulations, we extensively examine under what conditions the ionizing radiation can triggered star formation and we propose a diagram where the outcome of a simulation is determined by the incident flux and the initial mass of the Bonnor-Ebert sphere.

7.1 OFF-CENTRE EXPANSION OF AN HII REGION

In this application, we consider a uniform-density spherical cloud, having mass $M = 300\,\mathrm{M}_\odot$, initial radius $R = 1\,\mathrm{pc}$, and hence initial density $\rho_\mathrm{n} \sim 4.85\times10^{-21}\,\mathrm{g\,cm^{-3}}$. An ionizing source is placed at distance $D = 0.40\,\mathrm{pc}$ from the centre of the cloud, and emits ionizing photons at a constant rate $\dot{\mathcal{N}}_\mathrm{LyC} = 10^{49}\,\mathrm{s^{-1}}$ (see Fig. 7.1). The initial Strømgren sphere therefore has radius $R_\mathrm{St} = 0.42\,\mathrm{pc}$. The neutral gas is assumed to be at $T_\mathrm{n} = 100\,\mathrm{K}$. The simulation uses $\mathcal{N}_\mathrm{SPH} = 3\times10^5$ particles, and $\ell_\mathrm{MAX} = 7$ levels of HEALPix refinement. There are no gravitational forces. The simulation is terminated at $t = 0.5\,\mathrm{Myr}$.

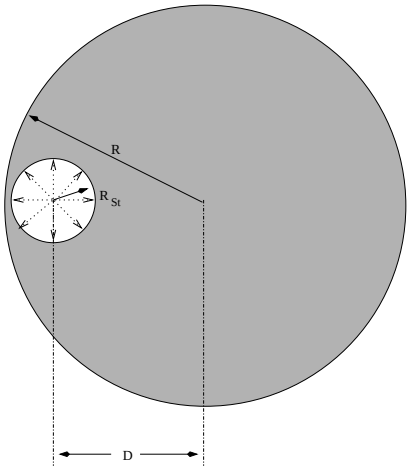

Figure 7.1: Schematic of the model used in the test described in §7.1

Figure 7.2 shows three stages in the evolution of the cloud. At $t \sim 0.018\,\mathrm{Myr}$ (Fig. 7.2a), the ionization front breaks through the edge of the cloud on the left-hand (near) side. From this moment on, the ionized gas can stream away freely on this side. However, on the right-hand side the ionization front continues to drive an approximately parabolic shock front into the interior of the cloud. By $t \sim 0.07\,\mathrm{Myr}$ (Fig. 7.2b), this shock has passed the centre of the cloud. At this stage the swept-up layer of neutral gas starts to break up into small "cometary knots". By $t \sim 0.14\,\mathrm{Myr}$ (Fig. 7.2c), the shock front has opened up into a more hyperbolic shape, and has reached the right-hand edge of the cloud. The shocked neutral gas has spawned even more cometary knots. Figure 7.3 shows a close-up of a few of the knots at $t \sim 0.38\,\mathrm{Myr}$. At $t \sim 0.50\,\mathrm{Myr}$, about 6 % of the gas remains neutral. All this neutral gas is contained in hundreds of small cometary knots, which are steadily being ablated by the ionizing flux.

In the early stages, the shell is subject to the Vishniac instability (Vishniac 1983); and

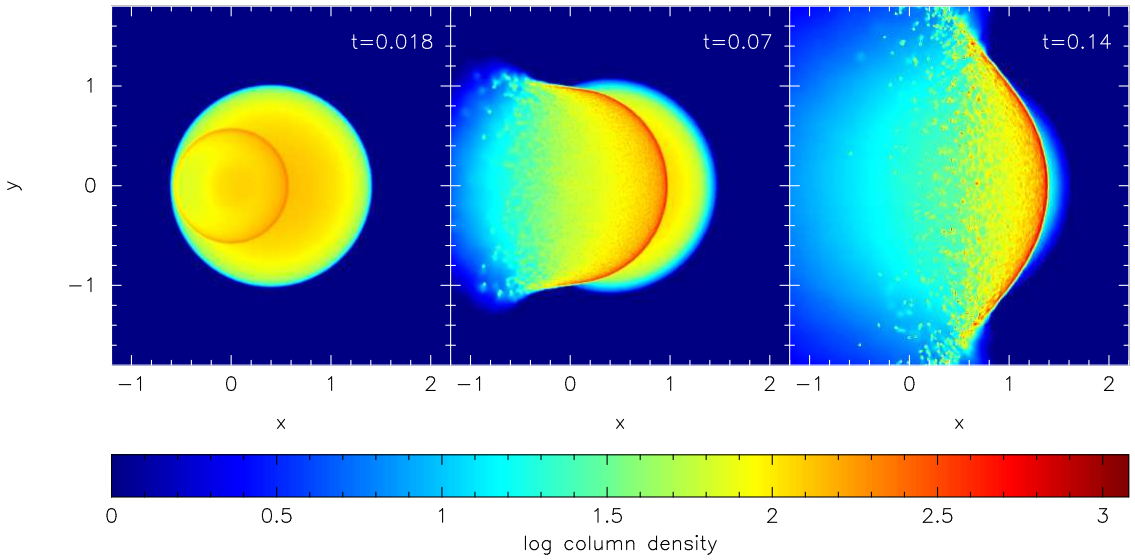

Figure 7.2: Column-density plots of the off-centre expansion of the HII region. Column-densities, Σ are measured in $\mathrm{M_\odot\,pc^{-2}}$ $\left(\equiv 8.7\times10^{19}\,\mathrm{H_2\,cm^{-2}}\right)$. The spatial axes ($x$ and y) are labelled in parsecs, and times in Myr are given in the top right-hand corner of each frame.

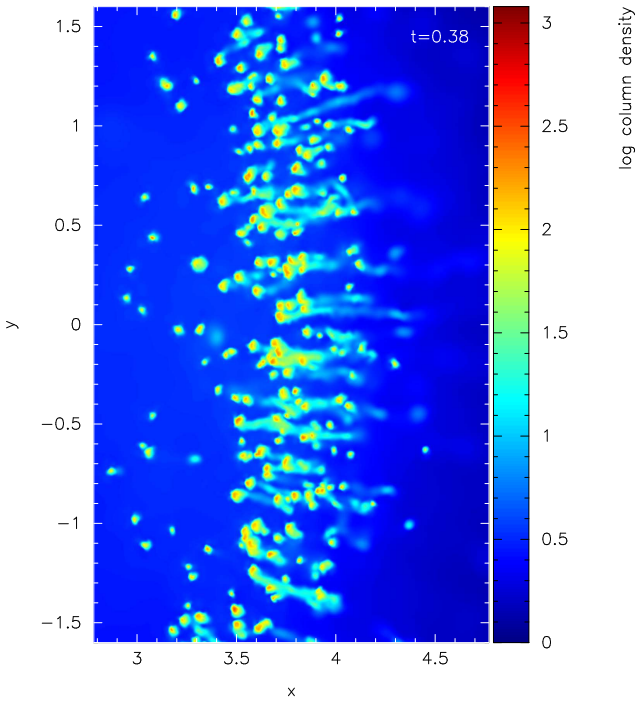

Figure 7.3: Detail of the off-centre expansion of the HII region. This column density plot shows some of the cometary knots formed at $t\sim0.38\,\mathrm{Myr}$. Column density, Σ, is measured in $\mathrm{M_\odot\,pc^{-2}}$ $\left(\equiv 8.7\times10^{19}\,\mathrm{H_2\,cm^{-2}}\right)$. The spatial axes ($x$ and y) are labelled in parsecs.

later on, when all the gas has been swept up into the shell and is being accelerated, it is prone to the Rayleigh-Taylor instability. Therefore we expect the shell to break up into small knots. However, the size of the resulting knots here is just larger than the resolution limit of the code, i.e. individual knots contain ~ 100 SPH particles, and therefore have masses $\sim 0.1\,\mathrm{M}_\odot$ and diameters $\sim 0.03\,\mathrm{pc}$. We do not have sufficient computational resources to establish the reality of the knots by performing convergence tests. However, we note that these knots are very reminiscent of those seen in the Helix Nebula (Capriotti 1973; O'Dell & Burkert 1996; O'Dell & Handron 1996; Capriotti & Kendall 2006).

7.2 EXPANSION OF AN HII REGION IN A FRACTAL MEDIUM

In this section we present an example of an expanding HII region in a fractal medium. We construct a spherical cloud with fractal dimension $d_f = 2.3$. The cloud consists of molecular hydrogen with fraction $X = 0.7$. We include no turbulent velocity. The total mass of the fractal cloud is $M = 1000\,\mathrm{M}_\odot$ and we use $\mathcal{N}_{\mathrm{SPH}} = 10^6$ particles. Its radius is $R = 1\,\mathrm{pc}$. The Jeans mass is $M_{\mathrm{J}} \sim 0.82\,\mathrm{M}_\odot$, so the cloud is gravitationaly unstable. The free fall time is $t_{\mathrm{ff}} \sim 0.96\,\mathrm{Myr}$.

At the centre of the cloud we place an exciting source emitting ionizing photons at a constant rate of $\dot{\mathcal{N}}_{\mathrm{LyC}} = 10^{49}\,\mathrm{s}^{-1}$. We use the barotropic equation of state described in §6.2.2 with $\rho_{\mathrm{CRIT}} = 10^{-13}\,\mathrm{g\,cm}^{-3}$. For $\rho \ll \rho_{\mathrm{CRIT}}$ the sound speed of the molecular hydrogen is $c_{\mathrm{s}} = 0.19\,\mathrm{km\,s}^{-1}$ which corresponds to a temperature of $T_{\mathrm{n}} = 10\,\mathrm{K}$. Self-gravity is included and the sink creation density is taken to be $\rho_{\mathrm{SINK}} = 10^{-11}\,\mathrm{g\,cm}^{-3}$. The maximum level of HEALPix refinement is taken to be $\ell_{\mathrm{max}} = 11$ which corresponds to $\mathcal{N}_{\mathrm{RAYS}} \sim 5 \times 10^7$ rays. The integration and angular resolution parameters are $f_1 = 0.25$ and $f_2 = 0.5$ respectively.

We evolve this fractal cloud for $t = 0.24\,\mathrm{Myr}$. Figure 7.4 shows the neutral mass versus time, and the same quantity when account is taken of the contribution of the mass growth of sink particles. Sink particles start to form at $t_{\mathrm{SINK}} \sim 0.11\,\mathrm{Myr}$. At the end of the simulation there are 192 sink particles formed and their total mass is $M_{\mathrm{s,tot}} = 110\,\mathrm{M}_\odot$ which is $\sim 11\%$ of the total initial mass. We find also that the highest mass that has been reached by a single sink particle is $M = 3\,\mathrm{M}_\odot$. It is interesting to note that the fraction of the cloud with $t_{ff} < 0.11\,\mathrm{Myr}$ is negligible. On the other hand for $t_{ff} < 0.24\,\mathrm{Myr}$ it is $\sim 53\,\mathrm{M}_\odot$, which is about a half of the total

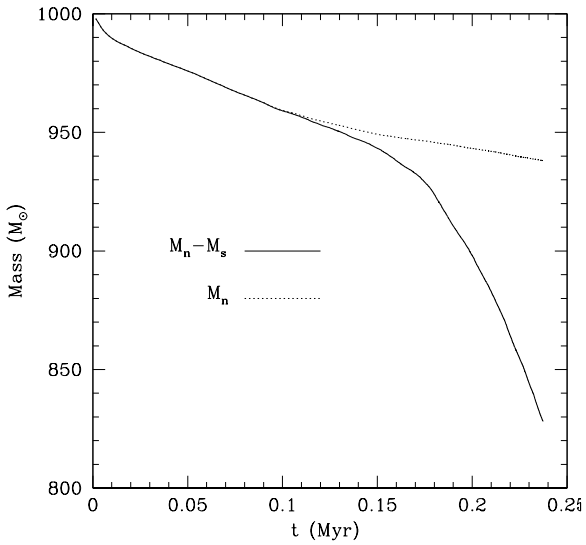

Figure 7.4: This figure shows the evolution of the neutral mass of the fractal cloud (solid line) and when account is taken of the contribution of the mass growth of sink particles (dash line)

mass of all sink particles. This shows that the ionizing radiation has played a crucial role in triggering star formation.

Figure 7.5 shows a sequence of column density plots of the fractal cloud at different times during its evolution. Black dots indicate sink particles. At the beginning of the simulation and for $t < 0.1\,\mathrm{Myr}$ the ionizing radiation starts to erode the medium and to compress parts of the cloud. This compression creates dense regions which fragment and eventually form stars, as seen in the figure for $t \gtrsim 0.1\,\mathrm{Myr}$. The sink particles appear to be formed at the borders of the neutral medium which face towards the exciting star. This strongly supports the idea that the ionizing radiation acts as a triggering mechanism for star formation.

Figure 7.6 shows a closeup sequence of column density plots of Fig. 7.5. In this figure we see that dense pre-existing clumps inside the neutral medium are squeezed as the ionization front wraps around this region. These dense clumps survive the passage of the ionization front and they appear to protude inside the Hii region creating cometary tails. At the heads of these tails, which are the regions pointing towards the exciting star, sink particles are likely to form. The sequence described here is very reminiscent of the evolutionary scenario discussed in §1.3.2 (elephant trunks, EGGs, proplyds).

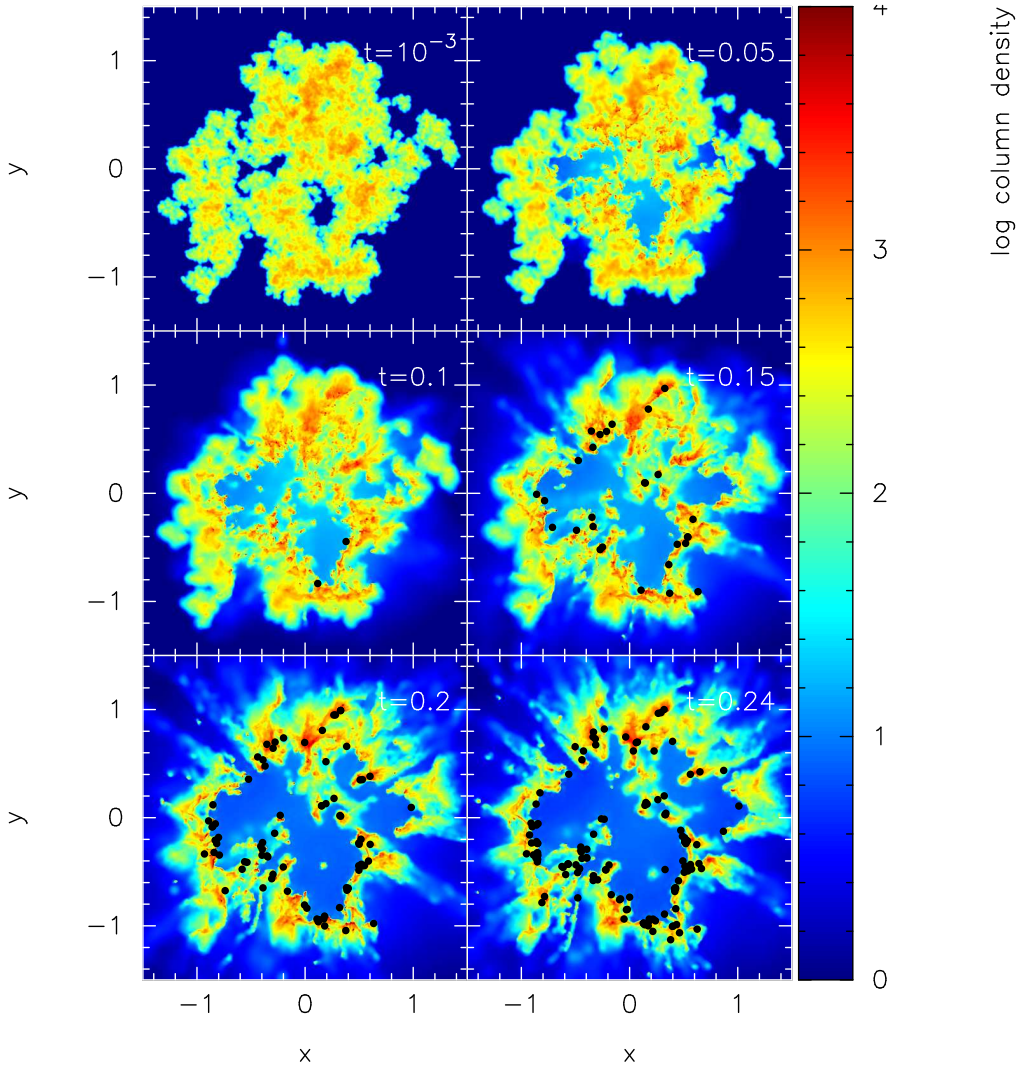

Figure 7.5: This figure shows a sequence of column density plots of the fractal medium described in §7.2. The snapshots were taken at the beginning of simulation ($t \sim 10^{-3}$ Myr) and at $t = 0.05$, 0.1, 0.15, 0.2, 0.24 Myr. Black dots indicate sink particles. The ionizing star is placed in the centre of each snapshot.

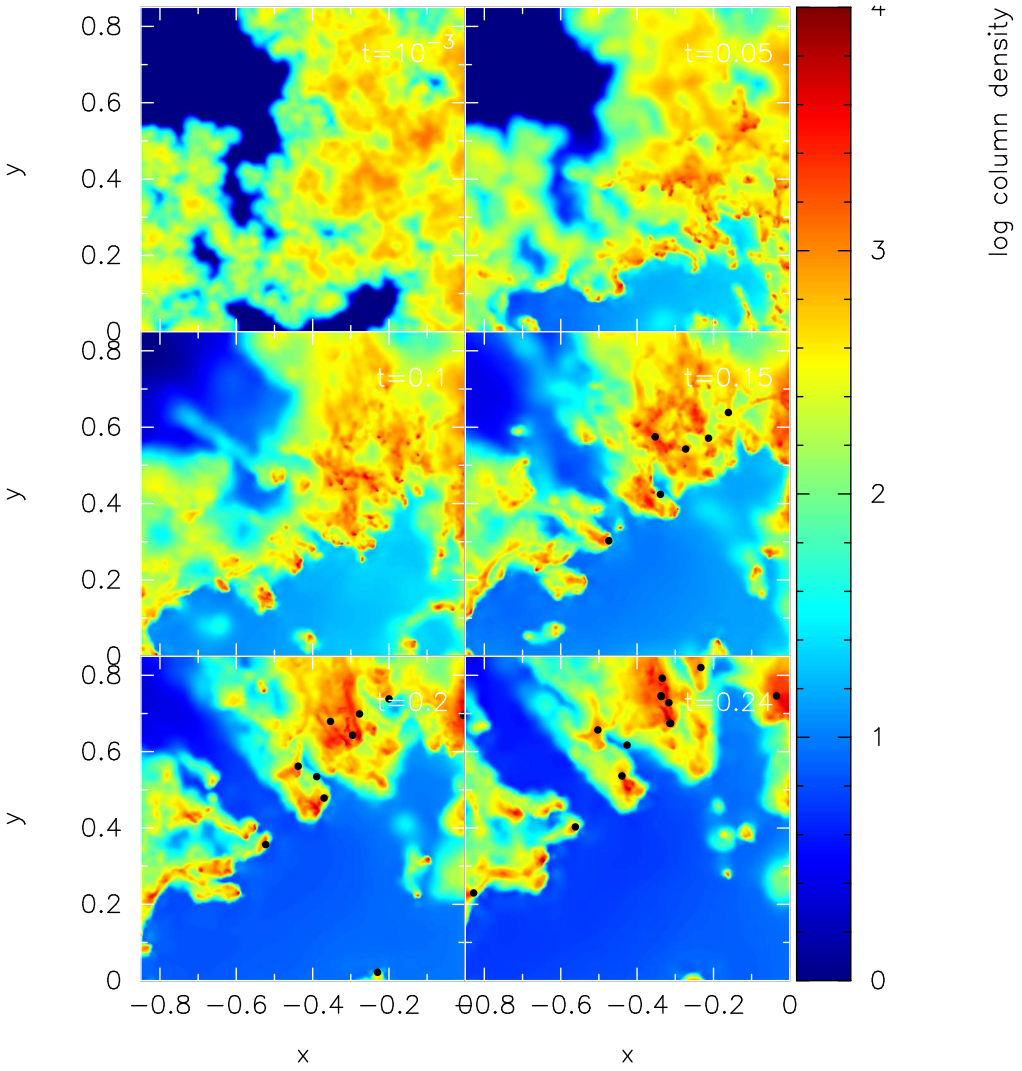

Figure 7.6: This figure shows a closeup sequence of column density plots of Fig. 7.5. Each snapshot is taken at the same time as in Fig. 7.5. Here we can see how pre-existing clumps of the neutral medium are squeezed as the ionization front overruns them, which result in the formation of EGGs and sink particles. The exciting star is placed in the bottom right corner of each snapshot.

From this short example of the evolution of an HII region inside a fractal medium, we can see how interesting this study is as it combines many different effects occurring during the expansion of ionized regions. We have plans to perform simulations using a wide range of different initial conditions such as the fractal dimension, the total initial mass, and to include turbulent velocity in the cloud. By analyzing the mass spectrum, the velocity distribution, and the statistics of the sink particles formed, we can gain insights into star formation in ionized regions. For instance, it would be very interesting to explore the maximum mass a star can reach as an expanding HII region triggers its formation, and compare our results with observations and theoretical approximations of other workers.

7.3 RADIATION DRIVEN COMPRESSION AND TRIGGERED STAR FORMATION

As we described in §1.3.1, radiation driven compression is one of the mechanisms for triggering star formation when an expanding HII region interacts with a nearby molecular cloud. Observations (Lefloch & Lazareff 1995; Lefloch et al. 1997; Morgan et al. 2008) provide evidence which strongly supports a connection between the formation of young stellar objects and the effect of ionizing radiation. Sugitani et al. (1999; 2000) point out that YSOs are mainly found on the axis of each globule aligned along the direction towards the ionizing star. In addition, Ikeda et al. (2008), Chauhan et al. (2009), and others, observe that the youngest stars are found to be deeply embedded inside bright-rimmed clouds while the older ones are close to the periphery or have emerged into the HII region.

Simulations of the radiation driven compression process including self-gravity have been presented by various authors. For example, Kessel-Deynet & Burkert (2003) show that gravitational forces increase suddenly the maximum density of a clump at the moment of its maximum compression, which may lead to the formation of new stars. Gritschneder et al. (2009) show that stable Bonnor-Ebert spheres are driven into gravitational collapse, and the final mass and the age of the collapsed core depend on the intensity of the incident flux. Miao et al. (2009) find that the morphological evolution of a clump is much more sensitive to its initial self-gravitational state than to other physical conditions. However, as mentioned earlier by Deharveng et al. (2005) "no model explains *where* star formation takes place (in the core or at its periphery)

or *when* (during the maximum compression phase, or earlier)".

In this chapter we will perform simulations of triggered star formation via the process of radiation driven compression. While the quoted statement by Deharveng et al. (2005) is still true, we will attempt to find a connection between the initial physical parameters of the simulations and the resultant evolution.

7.3.1 Description of the simulations

In these simulations, we use three settled Bonnor-Ebert spheres (see §6.2.3) of different masses $M = 2,\, 5,\, 10\,\mathrm{M}_{\odot}$ consisting of molecular hydrogen. All these spheres have $\xi_{\mathrm{B}} = 4$ and they are therefore stable. The particle resolution we use is taken to be 5×10^4 SPH particles per solar mass. We introduce here the dimensionless parameter

$$\lambda \equiv \frac{D}{R}\,, \tag{7.1}$$

where D is the distance of the centre of the clump from the source of ionizing radiation, and R is the radius of the clump (see Fig. 6.1). For each sphere we run simulations with $\lambda = 2,\, 5,\, 10$, and for each λ we use three different exciting stars with $\dot{\mathcal{N}}_{\mathrm{LyC}} = 10^{48},\, 10^{49},\, 10^{50}\,\mathrm{s}^{-1}$. We therefore have 27 different simulations whose properties are summarized in Table 7.1. In this table, M is the mass of the Bonnor-Ebert sphere, R is its radius, ρ_c is the central density, $\mathcal{N}_{\mathrm{SPH}}$ is the total number of SPH particles used in the simulation, $\dot{\mathcal{N}}_{\mathrm{LyC}}$ is the rate at which the star emits ionizing photons, and the last column is an identifier for each simulation.

We use the barotropic equation of state (Eqn.6.16) with $\rho_{\mathrm{CRIT}} = 10^{-13}\,\mathrm{g\,cm}^{-3}$. The sound speed of the molecular hydrogen, c_{s}, for $\rho \ll \rho_{\mathrm{CRIT}}$ is taken to be $c_{\mathrm{s}} = 0.19\,\mathrm{km\,s}^{-1}$. This corresponds to a temperature of $T_{\mathrm{n}} = 10\,\mathrm{K}$. The temperature of the ionized gas is taken to be $T_{\mathrm{i}} = 10^4\,\mathrm{K}$. Sink particles are formed when the density reaches $\rho_{\mathrm{sink}} = 10^{-11}\,\mathrm{g\,cm}^{-3}$. The sink radius is $2h$, where h is the smoothing length of the sink particle.

We use $\ell_{\mathrm{max}} = 11$ levels of HEALPix refinement which corresponds to $\mathcal{N}_{\mathrm{RAYS}} \sim 5 \times 10^7$ rays. The dimensionless tolerance parameter f_1 which controls the integration resolution of Eqn.(4.3) along a ray is taken to be $f_1 = 0.25$. The parameter f_2 which controls the angular resolution is taken to be $f_2 = 0.5$. With these parameters we achieve high resolution in simulating the structure and the location of the ionization

front.

As we already discussed in §6.1 and in §6.3, the incident flux emitted by an external source compresses the clump. Due to the internal thermal pressure of the neutral gas, the clump re-expands. The evolution can be followed until the clump is completely evaporated. It is important at this point to define the terminology we will use in our discussion below related with the evolution of the Bonnor-Ebert spheres. We call

- *Star Formation* (SF) when the clump creates sink particles.
- *Acceleration* (A) when the clump evolves through the sequence compression – expansion – evaporation without any sink particle formation.
- *Evaporation* (E) when the clump is fully evaporated before the incident flux compresses it.

7.3.2 The divergence of incident flux delays fragmentation

Since we place the Bonnor-Ebert spheres at various distances from the source, it is interesting at this point to explore how the divergence of the incident flux affects their evolution. To do this we perform a set of three simulations where we use the BES-s discussed in §6.2.3 . In each test we increase the distance D of the centre of BES-s from the source in order to have $\lambda = 2, 5, 10$ while we keep constant the initial incident flux

$$\Phi_{\rm D} = \frac{\dot{\mathcal{N}}_{\rm LyC}}{4\pi D^2} = 1.45 \times 10^{11}\,{\rm cm^{-2}\,s^{-1}}\,. \tag{7.2}$$

Thus, the exciting star for the $\lambda = 2$ clump emits $\dot{\mathcal{N}}_{\rm LyC,2} = 10^{48}\,{\rm s^{-1}}$, for $\lambda = 5$ it emits $\dot{\mathcal{N}}_{\rm LyC,5} = 6.26 \times 10^{48}\,{\rm s^{-1}}$, and for $\lambda = 10$ it emits $\dot{\mathcal{N}}_{\rm LyC,10} = 2.6 \times 10^{49}\,{\rm s^{-1}}$.

The left graph of Fig. 7.7 shows the evolution of neutral mass with time, $M_{\rm n}(t)$, for all three clumps, and the right graph shows the same plot when account is taken of the mass going into sinks, $M_{\rm n}(t) - M_{\rm s}(t)$. In addition, Table 7.2 shows a summary of these results. We see that the values $t_{\rm SINK}$ and $M_{\rm n,s}$ between the clumps with $\lambda = 5$ and 10 are quite similar. The total mass of sink particles formed is $M_{\rm s,tot} = 0.7 \pm 0.1\,{\rm M_\odot}$

Table 7.1: Summary of the BESs used in the simulations

$M\,(\mathrm{M}_\odot)$	$R\,(\mathrm{pc})$	$\rho_\mathrm{c}\,(\mathrm{g\,cm^{-3}})$	$\mathcal{N}_\mathrm{SPH}$	$D\,(\mathrm{pc})$	$\dot{\mathcal{N}}_\mathrm{LyC}\,\mathrm{s}^{-1}$	Simulation
2	0.12	5.06×10^{-20}	10^5	0.24	10^{48}	1
					10^{49}	2
					10^{50}	3
				0.6	10^{48}	4
					10^{49}	5
					10^{50}	6
				1.2	10^{48}	7
					10^{49}	8
					10^{50}	9
5	0.3	8.01×10^{-21}	2.5×10^5	0.6	10^{48}	10
					10^{49}	11
					10^{50}	12
				1.5	10^{48}	13
					10^{49}	14
					10^{50}	15
				3	10^{48}	16
					10^{49}	17
					10^{50}	18
10	0.6	2.02×10^{-21}	5×10^5	1.2	10^{48}	19
					10^{49}	20
					10^{50}	21
				3	10^{48}	22
					10^{49}	23
					10^{50}	24
				6	10^{48}	25
					10^{49}	26
					10^{50}	27

for all three clumps. However, the sink creation time, t_SINK, for the $\lambda = 2$ clump is somewhat later than the other two, and therefore $M_\mathrm{n,s}$ is somewhat lower.

To see why the divergence of the incident flux delays the fragmentation, we plot in Fig. 7.8 the column density of the clumps with $\lambda = 2$ and with $\lambda = 10$ as seen from the star ($z - x$ axes) at $t = 0.025\,\mathrm{Myr}$. Observe that the surface density of the shocked core is lower for lower λ, and therefore the self-gravitational forces in the core are weaker. In addition, the velocity field in the shocked material has a greater tangential divergence for lower λ. Both these factors act to delay fragmentation, and hence also sink creation, when λ is small, i.e. when the ionizing flux is more divergent.

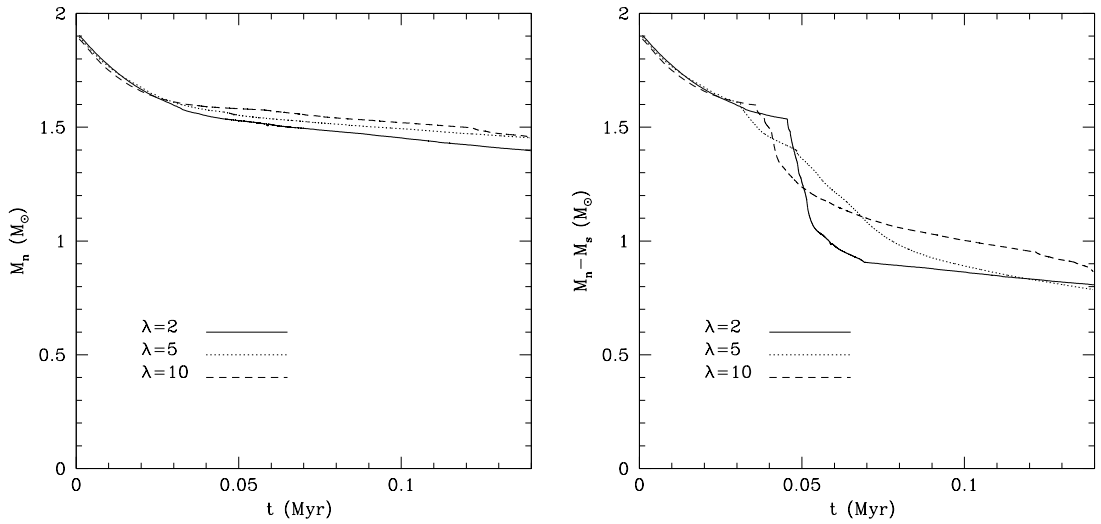

Figure 7.7: Left graph shows the evaporation of neutral mass versus time for all clumps. The right graph shows the evaporation of neutral mass when account is taken of the mass growth of sink particles. The divergence of the incident flux delays fragmentation.

Table 7.2: Summary of the results of the simulations described in §7.3.2.

λ	$t_{\rm sink}$ Myr	$M_{\rm n,s}$ ($\rm M_\odot$)	$M_{\rm s,tot}$ ($\rm M_\odot$)
2	0.0455	1.536	0.59
5	0.0311	1.603	0.75
10	0.0358	1.597	0.77

7.3.3 OUTCOMES

As we saw from the technical tests described in Chapter 6, numerical noise affects the physical quantities of the clump during its evolution. However, there are quantities which are independent of this noise; these include the sink creation time, $t_{\rm SINK}$, the total final mass of the sink particles formed, $M_{\rm s,tot}$, and the remaining neutral mass of the clump, $M_{\rm n,s}$, at $t_{\rm SINK}$. These are the values that will be taken into account in examining the results of the simulations in this section. Table 7.3 summarizes the results of the 27 simulations performed. In this table, $\Phi_{\rm D}$ is the incident flux at D, the column 'Evolution' characterizes whether the clump forms stars, accelerates or evaporates, and the rest of the columns have already been defined above.

In §7.3.3 we examine the morphological structure of all clumps at sink creation time. In §7.3.3 we present a diagram where we map regions corresponding to the evolutionary outcomes of all the simulations. In §7.3.3 we study in which part of each

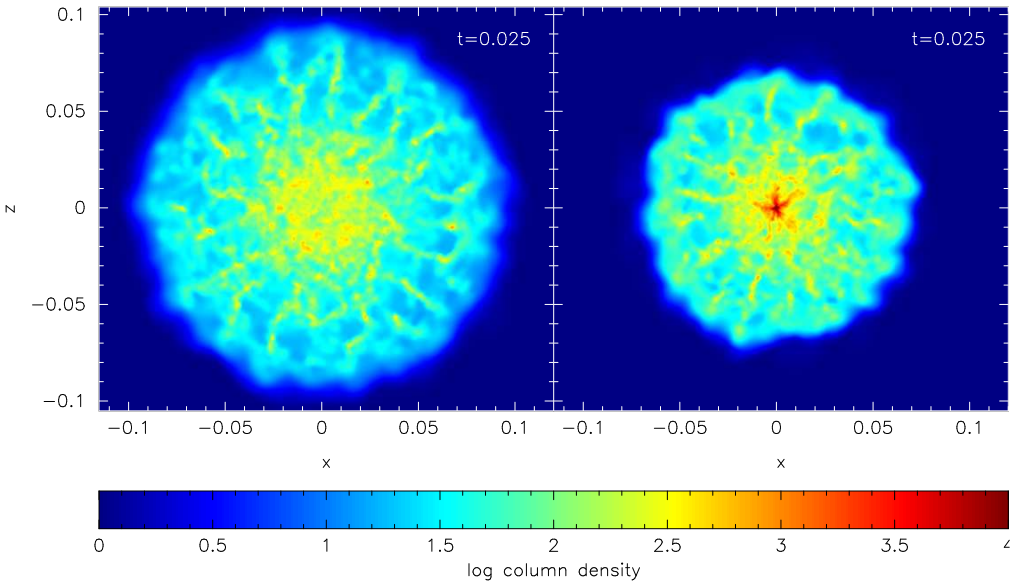

Figure 7.8: Column density plots of the clumps with $\lambda = 2$ (left) and with $\lambda = 10$ (right) as seen from the star at $t = 0.025\,\mathrm{Myr}$. Observe that in the right image the surface density is higher.

Bonnor-Ebert sphere star formation occurs and in §7.3.3 we study in which phase during the compression it occurs. Finally, in §7.3.3 we examine the final total mass of all sinks formed and we see how it correlates with the initial parameters of the simulations.

Morphological structure at t_{SINK}

In this subsection we will describe the morphological structure of each Bonnor-Ebert sphere at t_{SINK}. Figures 7.11, 7.12, and 7.13, show column density plots of $M = 2, 5, 10\,\mathrm{M}_{\odot}$ spheres respectively for different values of the incident flux Φ. Clumps that are either accelerated or evaporated are marked with 'A' and 'E' respectively and no snapshot is taken. Note also that for $M = 2\,\mathrm{M}_{\odot}$ the fluxes for simulations 1 and 9 (of Table 7.3) are the same but λ is different; hence the morphology is very different at t_{SINK} due to the divergence of the incident flux as discussed in §7.3.2.

In general, at t_{SINK} each clump has a well defined morphological structure, and the star formation is concentrated in a particular part of this structure, as described below. However, in simulations 1, 10 and 19 (see Fig. 7.11f, Fig. 7.12d, and Fig. 7.13d) the relation between the pricipal location of star formation and the overall

Table 7.3: Results of the simulations

Simulation	λ	$\Phi_{\rm D}$ ($\rm cm^{-2}\,s^{-1}$)	Evolution	$t_{\rm SINK}$ (Myr)	$M_{\rm n,s}$ ($\rm M_\odot$)	$M_{\rm s,tot}$ ($\rm M_\odot$)
1	2	5.8×10^{11}	SF	0.046	1.54	0.59
2		5.8×10^{12}	SF	0.022	1.05	0.67
3		5.8×10^{13}	A	–	–	–
4	5	2.3×10^{10}	SF	0.066	1.8	0.66
5		2.3×10^{11}	SF	0.028	1.51	0.73
6		2.3×10^{12}	SF	0.014	0.98	0.38
7	10	5.8×10^{9}	SF	0.129	1.86	1.33
8		5.8×10^{10}	SF	0.044	1.74	0.38
9		5.8×10^{11}	SF	0.02	1.35	0.43
10	2	2.3×10^{10}	SF	0.079	3.4	1.66
11		2.3×10^{11}	SF	0.034	1.8	0.35
12		2.3×10^{12}	E	–	–	–
13	5	3.7×10^{9}	SF	0.108	4.3	0.94
14		3.7×10^{10}	SF	0.047	3.34	0.86
15		3.7×10^{11}	A	–	–	–
16	10	9.3×10^{8}	SF	0.168	4.6	3.19
17		9.3×10^{9}	SF	0.069	4	0.89
18		9.3×10^{10}	SF	0.036	2.75	1.1
19	2	5.8×10^{9}	SF	0.123	6.07	2.69
20		5.8×10^{10}	SF	0.057	2.28	0.2
21		5.8×10^{11}	E	–	–	–
22	5	9.3×10^{8}	SF	0.137	8.1	2.35
23		9.3×10^{9}	SF	0.077	5.7	1.6
24		9.3×10^{10}	A	–	–	–
25	10	2.3×10^{8}	SF	0.231	8.9	3.65
26		2.3×10^{9}	SF	0.097	7.3	2.15
27		2.3×10^{10}	SF	0.055	4.25	1.14

structure of the clump is less clear, and therefore we omit these simulations from the following discussion.

When the incident ionizing flux is low, the shock front driven into the front side of the clump is quite weak and it sweeps up matter rather slowly. Consequently, long before the shock front reaches the centre of the clump, the disc-shaped layer of swept-up gas becomes sufficiently massive to contract laterally, due to its own self-gravity; as the material in the layer converges on the axis of symmetry, the increase in pressure deflects the inward flow towards the centre of the clump, creating a dense filament down the axis of symmetry, and it is in this filament that star formation first occurs, usually at a point away from the ionization front and towards the centre of the clump (i.e. away from the periphery of the clump – see Fig. 7.9).

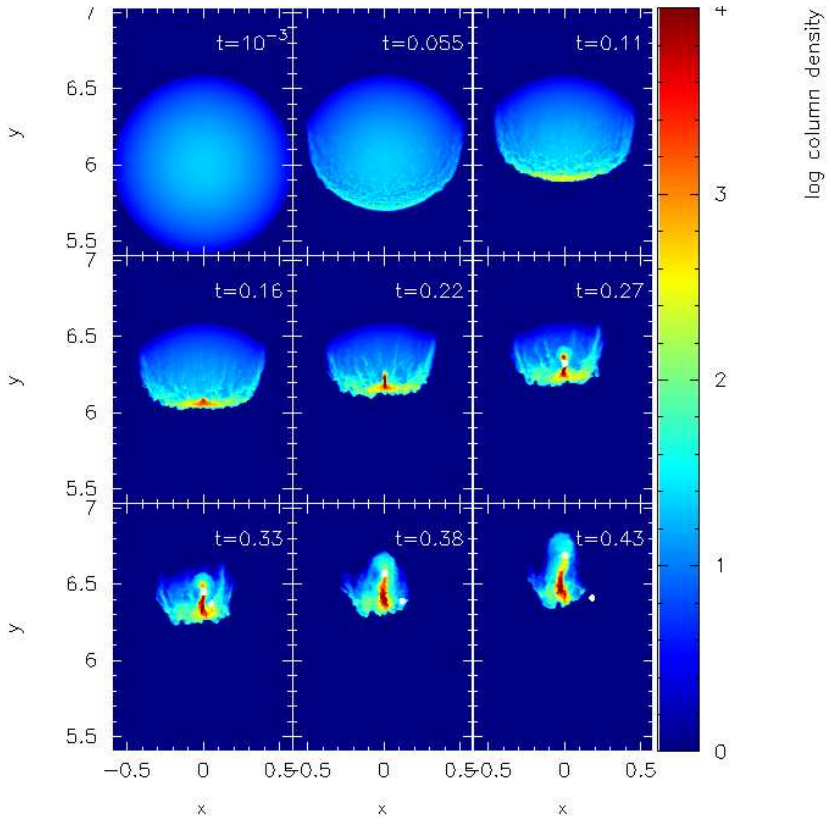

Figure 7.9: This figure shows a sequence of the formation of the filamentary structure in the Bonnor-Ebert sphere of simulation 25. In this low-flux simulation, star formation occurs in the innermost part of the dense filament.

When the incident ionizing flux is high, the shock front driven into the front side of clump is quite strong and it sweeps up matter rather rapidly. As a result the swept-up layer becomes sufficiently massive to fragment, before it has had time to undergo much lateral contraction under its own self-gravity (and therefore before there has been time to form an axial filament). Consequently star formation first occurs near the centre of the swept-up layer, and close to the ionization front (i.e. close to the periphery of the clump – see Fig. 7.10).

The flux-mass diagram

In Fig. 7.15 we introduce the flux-mass diagram. The logarithmic x-axis of this diagram is the incident flux ($\log \Phi$) and the y-axis is the initial mass M of the clump. We mark with a triangle when the clump forms stars, with a square when the clump is accelerated, and with a hexagon when it is evaporated. Hence we are able to define

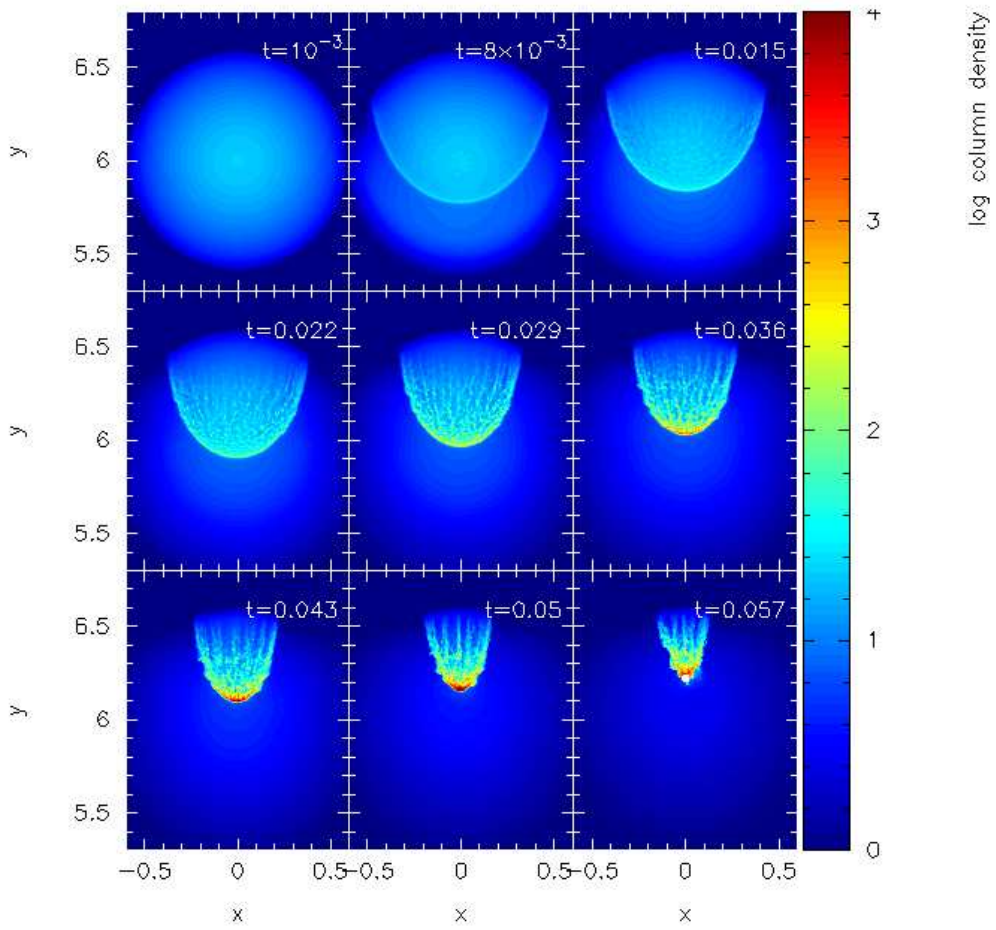

Figure 7.10: This figure shows a sequence of the evolution of the Bonnor-Ebert sphere of simulation 27. In this high-flux simulation, star formation occurs at the periphery of the **V**-shaped clump.

the zones where the outcome is 'Star Formation', 'Acceleration' and 'Evaporation'.

We perform an additional simulation for the BES-s with $M = 2\,\mathrm{M}_\odot$ and $\lambda = 2$ to have a more complete picture of the zone of Evaporation, since for this clump mass none of the ionizing fluxes explored is able to evaporate the clump instantaneously. In this extra simulation, the ionizing star emits photons at a rate $\dot{\mathcal{N}}_{\mathrm{LyC}} = 10^{51}\,\mathrm{s}^{-1}$ which corresponds to $\Phi_{\mathrm{D}} = 5.8 \times 10^{14}\,\mathrm{cm}^{-2}\,\mathrm{s}^{-1}$. This flux evaporates the whole clump immediately (E) and thus we mark it in the diagram with a hexagon.

This flux-mass diagram can be divided into three zones which correspond to the evolutionary result of each simulation. The two big zones SF and E on the left and on the right of the diagram respectively, are separated by the thinner zone A. From

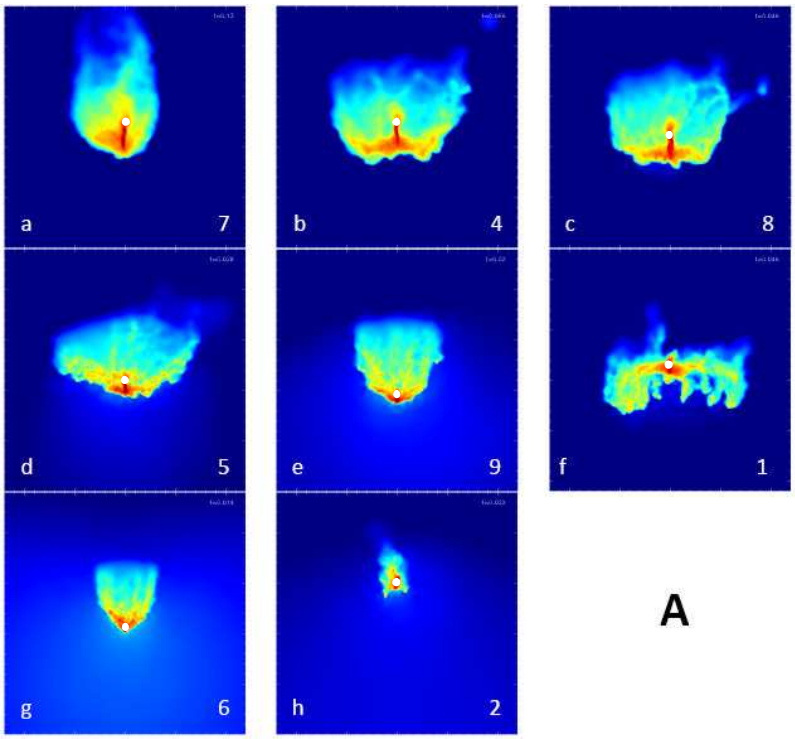

Figure 7.11: In this figure, we plot column density snapshots of all clumps with $M = 2\,\mathrm{M}_{\odot}$ in order of increasing flux Φ_{D}. The direction of the flux is from bottom to top. Each snapshot is taken at $t = t_{\mathrm{SINK}}$. The sink particles are marked with small white dots. The number at the bottom right of each snapshot is the identifier of the simulation from Table 7.3. The size of each box is $0.12\,\mathrm{pc} \times 0.12\,\mathrm{pc}$.

these simulations it is not possible to define the exact location of the transition from one zone to another. Therefore, we cannot demonstrate how the thickness of zone A depends on the flux Φ_{D} and the initial mass M of the clumps. However, it is clear that as the masses M of these Bonnor-Ebert spheres decrease, they appear to survive more in higher fluxes. This is because the central density, ρ_{c}, of the spheres increases with decreasing initial mass (for constant ξ_{B}), and therefore more ionizing radiation is needed to erode them.

Stars form closer to the periphery with increasing flux

A common feature amongst the morphological structures of all clumps at t_{SINK} is that stars form close to the symmetry axis joining the centre of the clump to the exciting star. This is in agreement with the observations by Sugitani et al. (1999). We define here as d_{t} the distance of the first sink particle formed from the ionization front. The

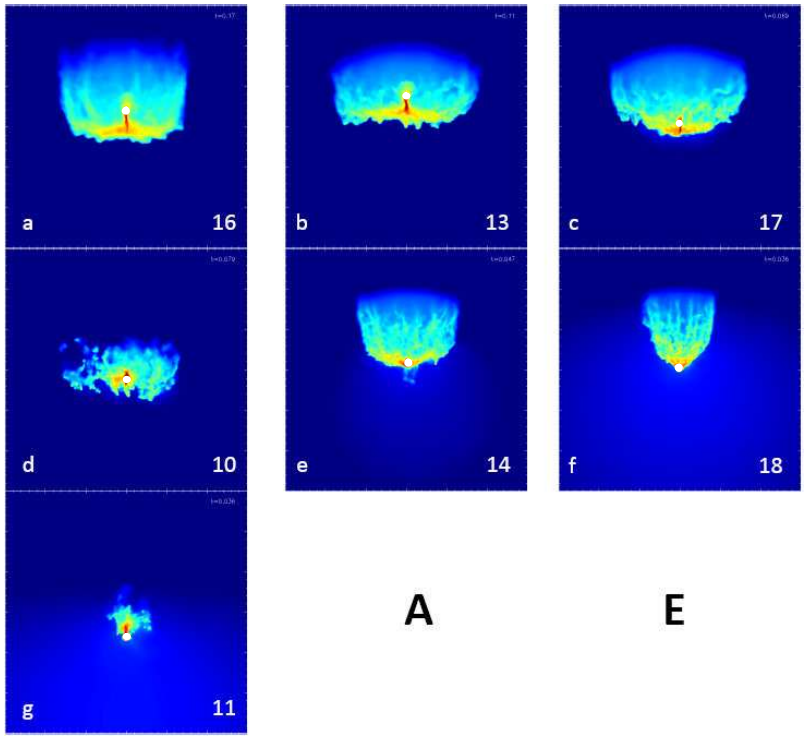

Figure 7.12: As in Fig. 7.11 for $M = 5\,\mathrm{M}_\odot$. The size of each box is $0.3\,\mathrm{pc} \times 0.3\,\mathrm{pc}$

error in measuring d_t is given by the error in determination of the boarders of each cloud from the column density plots, which is $0.03R$, where R is the initial radius of the BES.

In the left graph of Fig. 7.16 we plot d_t, normalized to the radius R of the clump, d_t/R, for all SF spheres versus the flux Φ. It is useful – if somewhat arbitrary – to divide each curve into three parts, and hence the diagram is divided into three zones. In the right graph of Fig. 7.16 we map these three zones onto the flux-mass diagram.

The first zone (1) corresponds to low fluxes. Here, stars tend to form along the filamentary structure and particularly at its innermost part. The second zone (2) corresponds to intermediate fluxes. Here, the filament becomes smaller and therefore stars tend to form closer to the periphery. Finally, the third zone (3) corresponds to high fluxes. The filamentary structure here does not have time to develop and therefore stars are formed *at* the periphery.

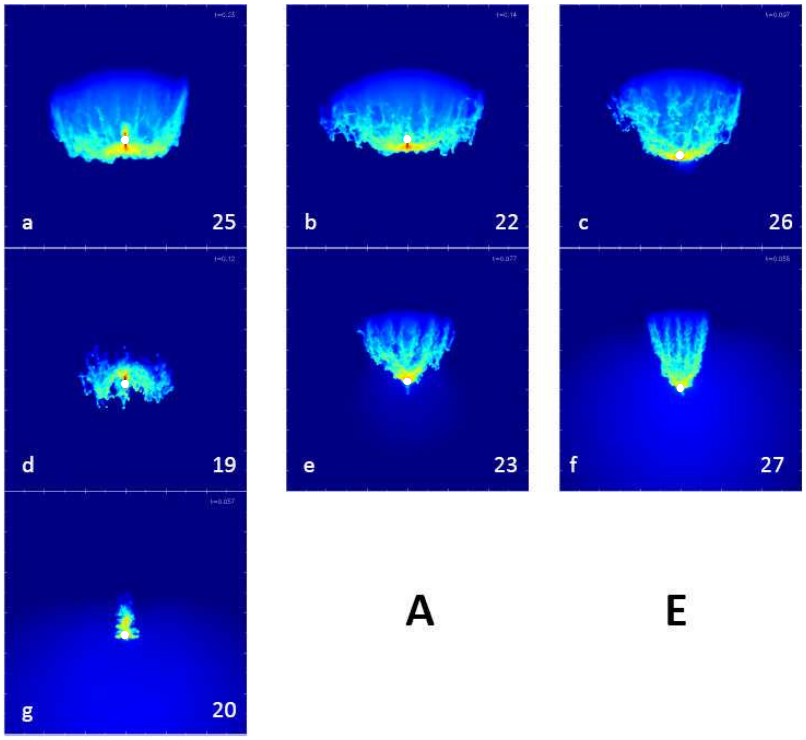

Figure 7.13: As in Fig. 7.11 for $M = 10\,\mathrm{M}_{\odot}$. The size of each box is $0.6\,\mathrm{pc} \times 0.6\,\mathrm{pc}$

Stars form during maximum compression with increasing the flux

From Figs. 7.11 - 7.13 we see that the lateral compression of each clump at t_{SINK} (i.e. the compression perpendicular to the axis of symmetry) is connected with the incident flux Φ; for low fluxes it is weak whereas for high fluxes it is strong. We define w_{d} as the separation of the two opposite compressed sides of each clump and we normalize it with the initial radius of the Bonnor-Ebert sphere, w_{d}/R. This value represents a measure of lateral compression. The error in measuring w_{d}/R is the same as discussed in §7.3.3.

In the left graph of Fig. 7.17 we plot w_{d}/R versus the flux Φ. These curves show that for high fluxes, stars are formed when w_{d}/R is small which means that the clumps are very compressed. However, w_{d}/R appears to have a maximum value for intermediate fluxes. This is most clearly seen in the $2\,\mathrm{M}_{\odot}$ curve. Here, w_{d}/R has the same value for both fluxes $\Phi = 5.8 \times 10^{9}\,\mathrm{cm}^{-2}\,\mathrm{s}^{-1}$ and $\Phi = 5.8 \times 10^{11}\,\mathrm{cm}^{-2}\,\mathrm{s}^{-1}$. These fluxes correspond to simulations 7 & 9 of Table 7.3 respectively. If we also check their morphological structure in Fig. 7.11a,e, we will observe that the filament in the low-flux simulation (7) is much more extended than in the higher flux simulation (9). Given that the respective sink creation times satisfy $t_{\mathrm{SINK},7} > t_{\mathrm{SINK},9}$, this extended

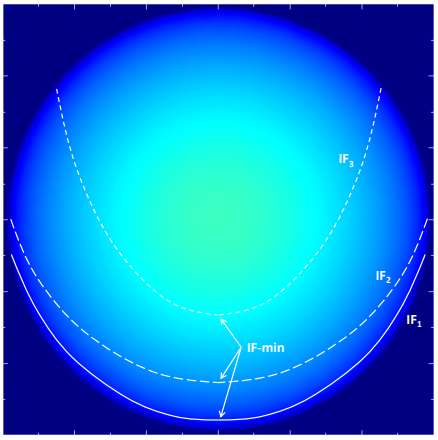

Figure 7.14: This figure shows the positions of the ionization front in a settled Bonnor-Ebert sphere at the beginning of a simulation with: i) low-flux (IF_1), ii) intermediate flux (IF_2), and iii) high flux (IF_3). The position of the IF-min point is drawn for each case.

filament reflects the fact that in the low-flux simulation there has been more time for lateral contraction of the swept-up layer.

To see this, in Fig. 7.18 we plot the gravitational acceleration, $a_{\rm grav}$, of all neutral SPH particles versus the distance D from the source, where

$$a_{\rm grav} = \sqrt{a_{\rm grav,x}^2 + a_{\rm grav,y}^2 + a_{\rm grav,z}^2} \tag{7.3}$$

and $a_{\rm grav,x}$, $a_{\rm grav,y}$, $a_{\rm grav,z}$ are the x, y, z, components of the gravitational acceleration respectively. In the left graph we plot $a_{\rm grav}$ for simulation 7 and in the right graph for simulation 9. This figure shows that in the first clump only, the SPH particles well inside it are gravitationally attracted. The peaks of $a_{\rm grav}$ in both graphs correspond to the most dense parts of the filamentary structure, where star formation is happening.

In the right graph of Fig. 7.17, we identify the simulations corresponding to the maximum values of $w_{\rm d}/R$ in the flux-mass diagram. Therefore, this line defines the transition between the left region where gravity forces play an additional role in compressing the clump, and the right region where the compression is mainly the result of the ionizing radiation.

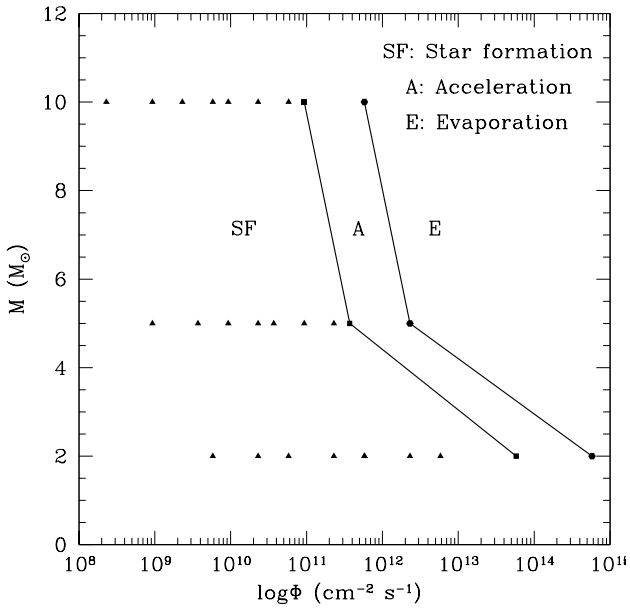

Figure 7.15: The flux-mass diagram.

Low fluxes increase the total mass of sinks

As we saw in §7.3.3, stars tend to form in the interior of the Bonnor-Ebert sphere at low fluxes and close to the periphery at high fluxes. Therefore, low fluxes increase the total final mass of the sink particles, since the latter are embedded in the neutral gas for longer periods of time. To see this, in the left graph of Fig. 7.19 we plot $M_{\rm s,tot}/M$ versus $M_{\rm n,s}/M$. The first term represents the total final mass of sink particles normalized with the initial mass of the clump, and the second the neutral mass of each clump remaining at $t_{\rm SINK}$ normalized in the same way. The right graph of this figure, plots $M_{\rm n,s}/M$ versus the incident flux Φ. The two big undulations in the $2\,{\rm M}_\odot$ curve, and the two smaller ones in the $5\,{\rm M}_\odot$ and the $10\,{\rm M}_\odot$ curves, correspond to simulations with low λ. They are therefore caused by the divergence of the incident flux.

These two graphs are divided into three zones. In the first zone (1), which corresponds to low fluxes, the radiation has ionized $\sim 20\%$ of the initial mass of each clump before the first star is formed. As we saw in §7.3.3, at these fluxes the mutual gravitational forces of the clump play an additional role in the compression. This factor acts to increase rapidly $M_{\rm s,tot}/M$ as we see in the left graph. The second zone (2) corresponds to intermediate fluxes. Here the ionizing radiation has eroded 20 to 40% of the initial gas at $t_{\rm SINK}$, and the value of $M_{\rm s,tot}/M$ remains relatively constant. Finally, the third

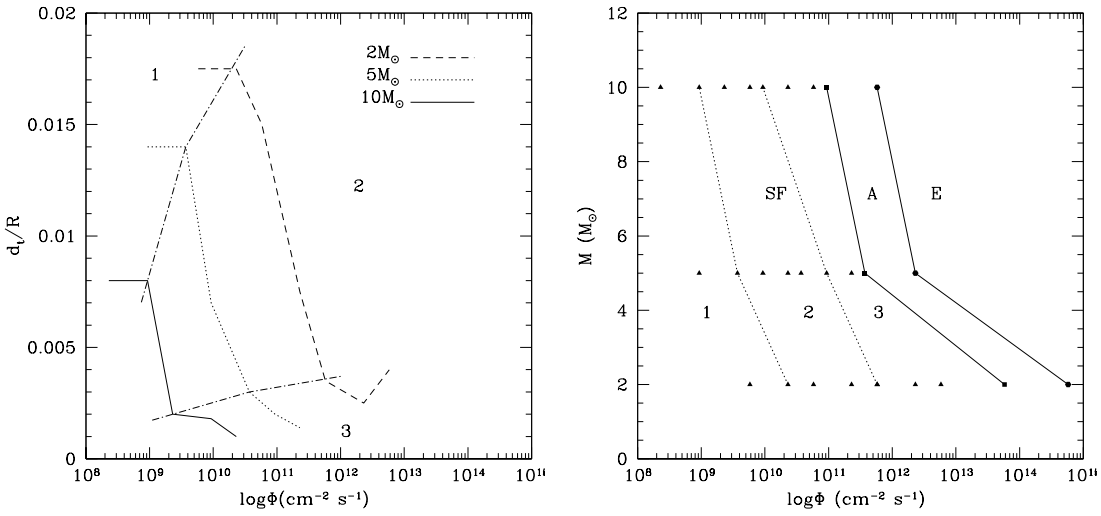

Figure 7.16: The left diagram plots d_t/R versus $\log\Phi$. Zones 1,2,3 are separated with dash-dotted lines. The right diagram maps these zones which are separated with dotted lines.

zone (3) corresponds to higher fluxes and $> 40\%$ of the initial sphere has been ionized at t_{SINK}. Star formation occurs at the periphery of the clump which results in a low value of $M_{\mathrm{s,tot}}/M$, since sinks escape into the interior of the HII region quite early and therefore cease accreting. The bottom graph of Fig. 7.19 maps these three regions onto the flux-mass diagram.

7.3.4 SUMMARY OF THE OUTCOMES

From these simulations we see how the ionizing radiation interacts with stable Bonnor-Ebert spheres and triggers star formation in the radiation driven compression mechanism. We have examined clumps of various masses and fluxes of various intensities. In general we find a connection between the incident flux (with respect of the initial mass of the Bonnor-Ebert sphere) and the corresponding star formation efficiency. Our results can be summarized as follows:

For low fluxes, an extended filamentary structure develops during the compression of the Bonnor-Ebert sphere along its axis towards the exciting star. Stars tend to form in the inner part of this structure and away from the periphery of the clump. This is in agreement with observations by Sugitani et al. (1999), and Beltrán et al. (2009). In addition, they claim that younger stars are observed in the innermost part of the

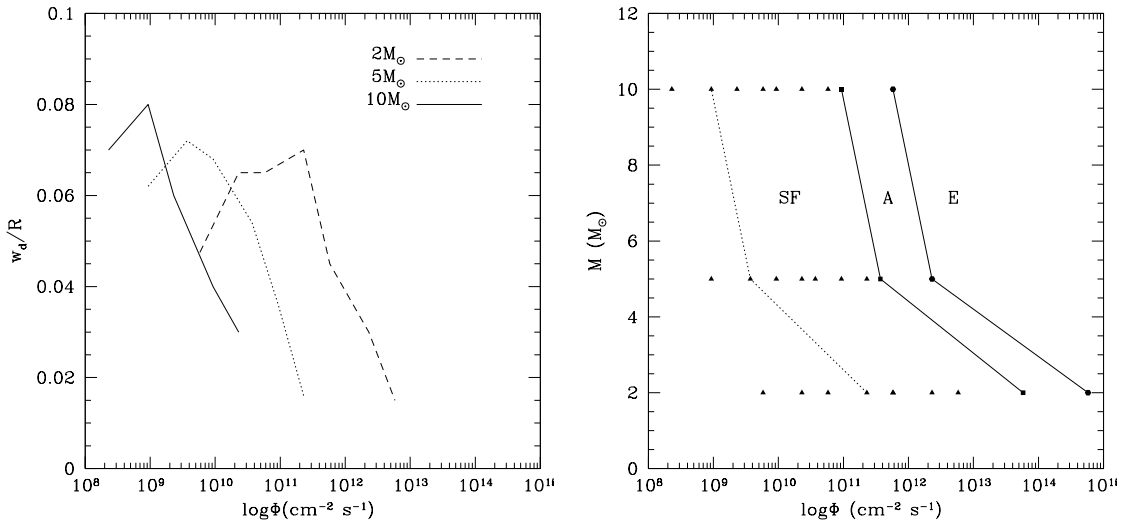

Figure 7.17: The left graph shows the connection between $w_{\rm d}/R$ with the flux Φ at $t_{\rm SINK}$. The dotted line on the right graph maps the maximum values of the curves in the flux-mass diagram.

globules. This outcome cannot be reproduced from these simulations.

Moreover, the central filament increases the mutual gravity forces which play an additional role driving the compression of the clump. The total final mass of the forming sink particles is high compared with the initial mass of each Bonnor-Ebert sphere.

For intermediate fluxes the length of the filamentary structure is smaller at $t_{\rm SINK}$ and the sink particles form closer to the periphery. At these fluxes radiation starts to play the dominant role in the compression of the clump. The total final mass of stars corresponds to $\sim 30\%$ of the initial mass of the Bonnor-Ebert sphere.

For high fluxes, the evolved clump at sink creation time has a **V**-shape structure. Here stars form at the periphery and the development of the filament is suppressed. The total mass of sink particles is low and they form during the maximum compression phase.

Increasing the incident flux further leads to no star formation and the clumps are accelerated and evaporated.

We also find that the time at which stars are formed ($t_{\rm SINK}$) depends on the incident

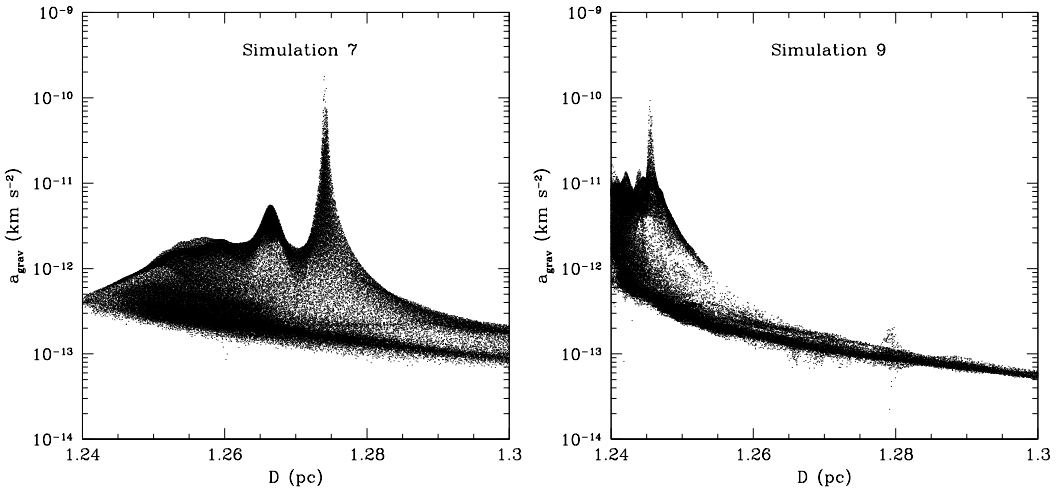

Figure 7.18: These figures plot $a_{\rm grav}$ versus D for simulation 7 (left) and for simulation 9 (right). The peaks correspond to the parts where star formation is occurring.

flux; the higher the flux, the sooner stars form. This is in agreement with simulations by Gritschneder et al. (2009).

We propose a semi-logarithmic flux-mass diagram, where we correlate the intensity of the incident flux and the initial mass of the Bonnor-Ebert spheres. On this diagram we map regions were star formation, acceleration and evaporation occur, as well as regions where the properties of the clumps at $t_{\rm SINK}$ are different.

Finally, we find that the divergence of the incident flux decreases the surface density of the shock front leading to weaker gravitational forces which in turn act to delay fragmentation.

In these simulations we used the basic hydrodynamical and gravitational equations. The berotropic equation of state is a good approximation for these simulations as we concentrate on the statistical analysis of triggered star formation. In this regard the results presented from these simulations are quite realistic. However, we cannot unambiguously demonstrate that including more complicated physics the outcomes will be significantly altered.

7.4 Chapter summary

In this chapter we presented several astrophysical simulations of expanding HII regions in different media. We examined the case of the off-centre expansion where we have showed that the formed cometary knots are very reminiscent of those seen in the Helix Nebula. We examined also the case of an expanding HII region in a fractal medium and we showed that our code can reproduce the sequence of triggered star formation as it was described in §1.3.2.

In this chapter our attention was particularly drawn in modelling the impact of the ionizing radiation in the Radiation Driven Compression mechanism. In these simulations we examinced several stable Bonnor-Ebert spheres, all with $\xi_{\rm B} = 4$ and of different masses, as they where eroded by the UV radiation emitted by the exciting source. We propose a flux-mass diagram where we map regions where the outcome is: i) Star Formation, ii) Acceleration, or iii) Evaporation.

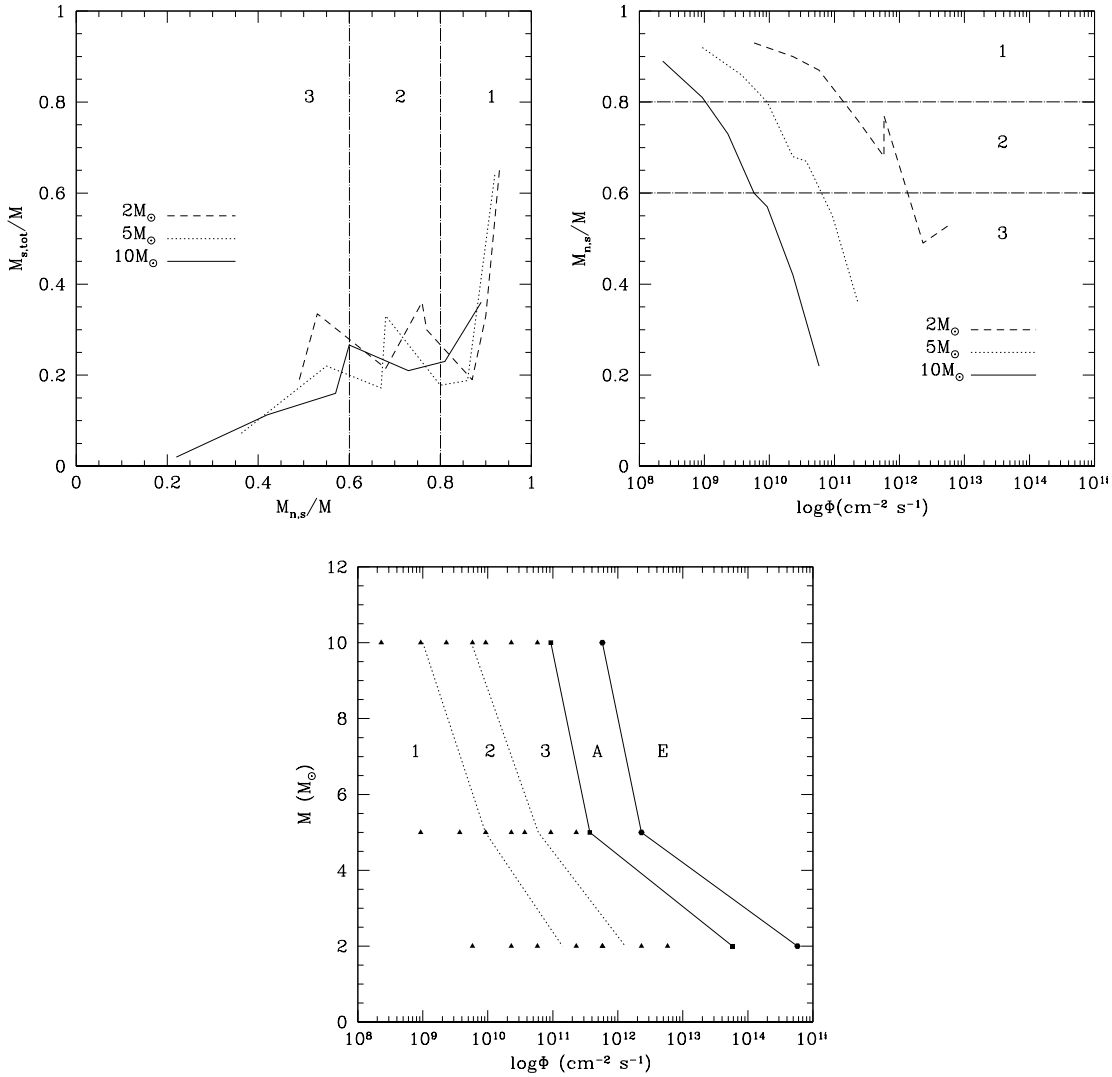

Figure 7.19: The top left diagram plots $M_{\rm s,tot}/M$ versus $M_{\rm n,s}/M$. The top right diagram plots $M_{\rm n,s}/M$ versus the incident flux Φ. Zones 1,2,3 are mapped in the flux-mass diagram, which is the bottom graph. Low fluxes favour the mass growth of sinks and hence increase $M_{\rm s,tot}$.

8 Conclusions & Future Prospects

In this thesis we present a new three dimensional SPH algorithm for including the propagation of ionizing radiation in the interstellar medium. We performed several tests to calibrate and explore the efficiency of the new algorithm. In particular we examined the D-type expansion of an HII *region where the ionizing star is placed (i) at the centre of a spherically symmetric cloud presenting also a new semi-analytic approximation for the propagation of the shock front, (ii) at the edge of a spherical cloud, exploring the rocket effect, and (iii) outside a spherical cloud studying the radiation driven compression mechanism. In addition, we mapped the evolution of a clump ionized by an external source and we defined whether it is able to fragment and form stars or not.*

In this chapter we summarize the main results, and we present our future plans.

8.1 THE NEW 3D SPH ALGORITHM FOR SIMULATING THE PROPAGATION OF IONIZING RADIATION

We implement a three dimensional SPH algorithm to simulate the propagation of ionizing radiation as it is emitted by an exciting star. This new algorithm creates a set of emanating rays from the star to its surrounding medium. The rays are created using the HEALPix algorithm (Górski et al. 2005) which allows the generation of levels of refinement achieving significant speed-up in comparison with uniform ray tracing (cf. Abel & Wandelt 2002). Each level ℓ creates $\mathcal{N}_{\rm RAYS} = 12 \times 4^{\ell}$ rays with $\ell = 0$ the basic level. During the generation of a level, HEALPix splits each ray of the previous level (mother-ray) into four new rays (child-rays). We split a ray as soon as its linear separation from neighbouring rays exceeds a fraction (defined by the user) of the local smoothing length h. With this scheme, we create families of rays along which the ionizing radiation propagates.

In order to simulate this propagation, we define a set of discrete points along the ray families where we evaluate the integral

$$I(r_j) = \int_{r=0}^{r=r_j} \rho^2(\mathbf{r}) r^2 dr \tag{8.1}$$

using the trapezium method. Here r is the distance of the j evaluation point from the source, and $\rho(\mathbf{r})$ its density. The resolution of this integration along a ray is defined by the user. The maximum value of Eqn.(8.1), $I_{\rm MAX}$, defines the position $R_{\rm IF}$ of the ionization front and it is given by

$$I(R_{\rm IF}) = \frac{\dot{\mathcal{N}}_{\rm LyC} m^2}{4\pi\alpha_{\rm B}} \equiv I_{\rm MAX}\,, \tag{8.2}$$

where $\dot{\mathcal{N}}_{\rm LyC}$ is the rate at which the exciting star emits ionizing photons, m is the mass of an hydrogen atom when account is taken of the contribution of helium, and $\alpha_{\rm B}$ is the recombination coefficient into excited stages only.

At each evaluation point we check the value of Eqn.(8.1). If it is $I(r) < I_{\rm MAX}$, then this evaluation point is in the interior of the HII region and further criteria are applied to see which SPH particles can be flagged as ionized. If it is $I(r) \geq I_{\rm MAX}$ we stop the integrations, we apply a binary chop subroutine to locate the exact position of the ionization front, and we smooth the temperature (in a region defined by the user) to

avoid high pressure gradients.

Finally, we rotate the entire ensemble of HEALPix rays through three random angles to avoid numerical artefacts due to discretization in the direction of a ray (see Krumholz et al. 2007).

8.2 Spherical symmetric expansion of an Hii region

We present numerical solutions, and have tried to find an analytical solution to the equation of motion for the accreting thin shell accelerated by the thermal pressure of an Hii region (Hosokawa & Inutsuka 2006), including the effects of the gravity

$$\frac{d}{dt}(M_{\rm sh}\dot{R}_{\rm sh}) = 4\pi R_{\rm sh}^2 P_{\rm i} - \frac{GM_{\rm sh}M_{\rm i}}{R_{\rm sh}^2} - \frac{GM_{\rm sh}^2}{2R_{\rm sh}^2}\,. \tag{8.3}$$

Here $P_{\rm i} = \rho_{\rm i} c_i^2$, $M_{\rm i} = (4\pi R_{\rm sh}^2 \rho_{\rm i})/3$, and $\rho_{\rm i} = \left(\frac{3m^2 \dot{\mathcal{N}}_{\rm LyC}}{4\pi a_{\rm B} R_{\rm sh}^2}\right)^{1/2}$ are the pressure, the mass and the density of the ionized gas, respectively. We find that this equation predicts the position of the shock front in contrast with the Spitzer solution (Spitzer 1978) which predicts the position of the ionization front. In addition, since it includes the effects of gravity (second and third term of the RHS), it is of more general nature.

For our purposes we use the SEREN SPH code (Hubber et al. in preparation). We perform two sets of simulations with spherically symmetric expanding Hii regions in a uniform-density cloud. In the first set, we do not include self-gravity and we perform a set of convergence tests with an increasing number of SPH particles. We calculate the position of the ionization front and we compare the results both with the Spitzer solution and Eqn.(8.3). We find that both simulations and expressions agree very well.

In the second set, we consider a much heavier cloud and we switch on self-gravity but with two modifications in order to prevent the infall of the undisturbed neutral gas, and to suppress the fragmentation of the shell. We locate the position of the shock front and we check the validity of Eqn.(8.3) and in particular the gravity terms. The comparison shows that the position of the shock front is very well predicted both by the semi-analytical approach and the simulation itself.

8.3 The rocket effect

We use our algorithm to simulate an off-centred expansion of an HII region. We perform a simulation with a uniform density spherical cloud with the ionizing star placed close to the edge of the cloud. We include no self gravity. The simulation shows that the ionization front expanding away from the centre of the cloud breaks out of the cloud and the ionized gas can stream away freely, while from the side towards the centre of the cloud, an approximately parabolic shock front forms. When this shock front passes through the entire cloud, it breaks up forming thousands of small cometary knots which are very reminiscent of those seen for example in the Helix Nebula.

We propose but cannot unambiguously demonstrate that during the early stages of the evolution, the shock front is subject to the Vishniac instability (Vishniac 1983) and later on when it is being accelerated, it is prone to the Rayleigh-Taylor instability.

8.4 Radiation Driven Compression

The algorithm is used to model the radiation driven compression mechanism in which a clump is ionized by an external source. In this mechanism, the radiation causes the clump to collapse. As it collapses, its internal thermal pressure increases and this leads to its re-expansion, and the formation of a cometary structure extending away from the ionizing source. We test our algorithm by reproducing as closely as possible the simulation of radiation driven compression by Lefloch & Lazareff (1994). The agreement in this comparison is very good.

Since our algorithm creates rays emanating spherically from the source, which is therefore of more general nature than of a plane-parallel propagation of the flux, we explore how the curvature of the incident flux affects the evolution of a clump during its ionization. We find that the curvature decreases the surface density of the formed shock front and this acts to slow down the evolution of the clump, in contrast with a plane-parallel incident flux.

We extend our study of this mechanism by performing a set of simulations to explore triggered star formation from clumps ionized by an external source. We construct settled Bonnor-Ebert spheres and we place them at various distances away from the

source. We also use various rates of emission of ionizing radiation which in turn result in various intensities of incident fluxes. We find a connection between the intensity of the incident flux, the initial mass of the Bonnor-Ebert sphere, and the star formation efficiency. In particular, we find that low fluxes favour the mass growth of sink particles, which are formed away from the periphery of the clump. At these fluxes, self-gravity plays an additional role in compressing the clump. On the other hand, high fluxes result in the formation of sink particles at the periphery of the clump and with low total mass. Here, the compression of the clump is a mainly caused by the ionizing radiation. Increasing further the incident flux prevents star formation and leads to the clump being accelerated and evaporated.

All these findings are mapped in a new semi-logarithmic diagram, which correlates the intensity of the incident flux and the initial mass of each Bonnor-Ebert sphere (flux-mass diagram). This diagram encapsulates the patterns of star formation triggered by radiation driven compression, and will be used in future modelling of this mechanism.

8.5 Future plans

Expanding HII regions are important for the study of star formation. Despite the significant effort that has been made so far by various workers in simulating the evolution of these regions, the mechanisms of how ionized radiation triggers star formation are not well understood. The 3D SPH algorithm presented in this thesis can contribute to understanding the influence of radiation from an O or B star on its surrounding neutral interstellar medium. Our plans in using this algorithm involve the study of:

- *The Collect and collapse model.* In this project we will examine the collect and collapse model (Elmegreen & Lada, 1977) in spherically symmetric expanding HII regions and we will study the mechanism of fragmentation of the dense shell (Whitworth et al. 1994a,b). We will also try to reproduce the observed regions that appear to be dominated by this mechanism (Deharveng et al. 2003; 2005, Zavagno et al. 2007) and investigate where star formation is likely to take place.
- *Pre-existing clumps in the neutral medium.* Here we will explore the contribution of pre-existing irregularities inside the neutral cloud in the evolution of an expanding HII region. As the ionization and shock front will pass these areas,

they will create elephant trunks, EGGs, YSOs and even proplyds as we described in §1.3.2. Our plan is to create a parameter space diagram and to map the conditions for triggered star formation as well as to explore their physical properties during their evolution.

- *Cometary knots in Helix Nebula.* In this project we will extend our study of the Radiation Driven Compression mechanism in modelling the evolution of the cometary knots observed in the Helix Nebula. For example, recently Matsuura et al. (2009) presented high resolution images of these knots observing their irregular structure. Our target is to simulate them as closely as possible, to reproduce their morphological structures.

- *Fractal clouds.* Simulating expanding HII regions in a fractal medium is of great interest since their structure is the closest possible to observed clouds. They are therefore realistic and thus important tools in modelling triggered and sequential star formation.

References

[1] Abel, T., & Wandelt, B. D. 2002, MNRAS, 330, L53

[2] Abel, T., Wise, J. H., & Bryan, G. L. 2007, ApJ, 659, L87

[3] Alvarez, M. A., Bromm, V., & Shapiro, P. R. 2006, ApJ, 639, 621

[4] Alves, J. F., Lada, C. J., & Lada, E. A. 2001, Nature, 409, 159

[5] Andre, P., Ward-Thompson, D., & Barsony, M. 2000, Protostars and Planets IV, 59

[6] Balick, B., Gammon, R. H., & Hjellming, R. M. 1974, PASP, 86, 616

[7] Balick, B. 1987, AJ, 94, 671

[8] Balick, B., & Frank, A. 2002, ARA&A, 40, 439

[9] Balsara, D. S. 1995, Journal of Computational Physics, 121, 357

[10] Banerjee, R., Pudritz, R. E., & Holmes, L. 2004, MNRAS, 355, 248

[11] Barnes, J., & Hut, P. 1986, Nature, 324, 446

[12] Bate, M. R., Bonnell, I. A., & Price, N. M. 1995, MNRAS, 277, 362

[13] Beltrán, M. T., Massi, F., López, R., Girart, J. M., & Estalella, R. 2009, A&A, 504, 97

[14] Bertoldi, F. 1989, ApJ, 346, 735

[15] Black, D. C., & Bodenheimer, P. 1975, ApJ, 199, 619

[16] Blackman, E. G., Frank, A., & Welch, C. 2001, ApJ, 546, 288

[17] Bok, B. J., & Reilly, E. F. 1947, ApJ, 105, 255

[18] Bonnor, W. B. 1956, MNRAS, 116, 351

[19] Burn, B. J. 1973, MNRAS, 165, 421

[20] Burkert, A., & O'dell, C. R. 1996, Bulletin of the American Astronomical Society, 28, 1402

[21] Capriotti, E. R. 1973, ApJ, 179, 495

[22] Capriotti, E. R., & Kendall, A. D. 2006, ApJ, 642, 923

[23] Chandrasekhar, S. 1951, Royal Society of London Proceedings Series A, 210, 26

[24] Chauhan, N., Pandey, A. K., Ogura, K., Ojha, D. K., Bhatt, B. C., Ghosh, S. K., & Rawat, P. S. 2009, MNRAS, 396, 964

[25] Courant, E., Friedrichs, K., & Lewy, H., 1967, IBJ Journal (March), 215

[26] Dale, J. E., Bonnell, I. A., Clarke, C. J., & Bate, M. R. 2005, MNRAS, 358, 291

[27] Dale, J. E., Ercolano, B., & Clarke, C. J. 2007, MNRAS, 382, 1759

[28] Dale, J. E., Clark, P. C., & Bonnell, I. A. 2007, MNRAS, 377, 535

[29] Davidson, K., & Fesen, R. A. 1985, ARA&A, 23, 119

[30] De Marco, O., O'Dell, C. R., Gelfond, P., Rubin, R. H., & Glover, S. C. O. 2006, AJ, 131, 2580

[31] Deharveng, L., Lefloch, B., Zavagno, A., Caplan, J., Whitworth, A. P., Nadeau, D., & Martín, S. 2003, A&A, 408, L25

[32] Deharveng, L., Zavagno, A., & Caplan, J. 2005, A&A, 433, 565

[33] Deharveng, L., Lefloch, B., Kurtz, S., Nadeau, D., Pomarès, M., Caplan, J., & Zavagno, A. 2008, A&A, 482, 585

[34] Ebert, R. 1957, Zeitschrift fur Astrophysik, 42, 263

[35] Elmegreen, B. G., & Lada, C. J. 1977, ApJ, 214, 725

[36] Elmegreen, B. G. 1994, ApJ, 427, 384

[37] Elmegreen, B. G. 1998, Origins, 148, 150

[38] Field, G. B., Goldsmith, D. W., & Habing, H. J. 1969, ApJ, 155, L149

[39] Garcia-Segura, G., & Franco, J. 1996, ApJ, 469, 171

[40] Gingold, R. A., & Monaghan, J. J. 1977, MNRAS, 181, 375

[41] Gordon, K. D., et al. 2000, ApJ, 544, 859

[42] Górski, K. M., Hivon, E., Banday, A. J., Wandelt, B. D., Hansen, F. K., Reinecke, M., & Bartelmann, M. 2005, ApJ, 622, 759

[43] Gritschneder, M., Naab, T., Burkert, A., Walch, S., Heitsch, F., & Wetzstein, M. 2009, MNRAS, 393, 21

[44] Henney, W. J., Arthur, S. J., de Colle, F., & Mellema, G. 2009, MNRAS, 398, 157

[45] Henry, R. B. C., Kwitter, K. B., & Dufour, R. J. 1999, ApJ, 517, 782

[46] Hernquist, L. 1987, ApJS, 64, 715

[47] Hester, J. J., et al. 1996, ApJ, 456, 225

[48] Hester, J. J., et al. 1996, AJ, 111, 2349

[49] Hester, J. J., et al. 2002, ApJ, 577, L49

[50] Hester, J. J., & Desch, S. J. 2005, Chondrites and the Protoplanetary Disk, 341, 107

[51] Hillenbrand, L. A. 1997, AJ, 113, 1733

[52] Hora, J. L., Latter, W. B., Allen, L. E., Marengo, M., Deutsch, L. K., & Pipher, J. L. 2004, arXiv:astro-ph/0405614

[53] Hosokawa, T., & Inutsuka, S.-i. 2006, ApJ, 646, 240

[54] Ikeda, H., et al. 2008, AJ, 135, 2323

[55] Indebetouw, R., Robitaille, T. P., Whitney, B. A., Churchwell, E., Babler, B., Meade, M., Watson, C., & Wolfire, M. 2007, ApJ, 666, 321

[56] Jeans, J. H. 1902, Royal Society of London Philosophical Transactions Series A, 199, 1

[57] Jones, E., Oliphant, T., Peterson, P. et al., 2001, SciPy: Open source scientific tools for Python, http://www.scipy.org/

[58] Kahn, F. D. 1954, Bull. Astron. Inst. Netherlands, 12, 187

[59] Kessel-Deynet, O., & Burkert, A. 2000, MNRAS, 315, 713

[60] Kessel-Deynet, O., & Burkert, A. 2003, MNRAS, 338, 545

[61] Krumholz, M. R., Stone, J. M., & Gardiner, T. A. 2007, ApJ, 671, 518

[62] Krumholz, M. R., & Bonnell, I. A. 2007, arXiv:0712.0828

[63] Krumholz, M. R., Klein, R. I., McKee, C. F., Offner, S. S. R., & Cunningham, A. J. 2009, Science, 323, 754

[64] Kwok, S., Purton, C. R., & Fitzgerald, P. M. 1978, ApJ, 219, L125

[65] Leene, A., & Pottasch, S. R. 1987, A&A, 173, 145

[66] Lefloch, B., & Lazareff, B. 1994, A&A, 289, 559

[67] Lefloch, B., & Lazareff, B. 1995, A&A, 301, 522

[68] Lefloch, B., Lazareff, B., & Castets, A. 1997, A&A, 324, 249

[69] Linsky, J. L., Gagné, M., Mytyk, A., McCaughrean, M., & Andersen, M. 2007, ApJ, 654, 347

[70] López-Martín, L., Raga, A. C., Mellema, G., Henney, W. J., & Cantó, J. 2001, ApJ, 548, 288

[71] Lucy, L. B. 1977, AJ, 82, 1013

[72] Lyubarsky, Y. E. 2002, MNRAS, 329, L34

[73] MacAlpine, G. M., & Satterfield, T. J. 2008, AJ, 136, 2152

[74] Makino, J., & Aarseth, S. J. 1992, PASJ, 44, 141

[75] Matsuura, M., et al. 2009, ApJ, 700, 1067

[76] McCaughrean, M. J., & Andersen, M. 2002, A&A, 389, 513

[77] McKee, C. F., & Ostriker, J. P. 1977, ApJ, 218, 148

[78] Meaburn, J., Clayton, C. A., Bryce, M., Walsh, J. R., Holloway, A. J., & Steffen, W. 1998, MNRAS, 294, 201

[79] Meaburn, J., Boumis, P., López, J. A., Harman, D. J., Bryce, M., Redman, M. P., & Mavromatakis, F. 2005, MNRAS, 360, 963

[80] Menten, K. M., Reid, M. J., Forbrich, J., & Brunthaler, A. 2007, A&A, 474, 515

[81] Miao, J., White, G. J., Nelson, R., Thompson, M., & Morgan, L. 2006, MNRAS, 369, 143

[82] Miao, J., White, G. J., Thompson, M. A., & Nelson, R. P. 2009, ApJ, 692, 382

[83] Monaghan, J. J., & Lattanzio, J. C. 1985, A&A, 149, 135

[84] Monaghan, J. J. 1992, ARA&A, 30, 543

[85] Monaghan, J. J. 2002, MNRAS, 335, 843

[86] Morgan, L. K., Thompson, M. A., Urquhart, J. S., & White, G. J. 2008, A&A, 477, 557

[87] Morris, J. P. & Monaghan, J.J., 1997, JCompPhys, 136, 41

[88] O'dell, C. R., Wen, Z., & Hu, X. 1993, ApJ, 410, 696

[89] O'Dell, C. R., & Burkert, A. 1997, *IAU Symposium 180, Planetary Nebulae* (Eds. H. J. Habing & H. J. G. L. M, Lamers; Kluwer) 332

[90] O'Dell, C. R., & Handron, K. D. 1996, AJ, 111, 1630

[91] O'Dell, C. R., McCullough, P. R., & Meixner, M. 2004, AJ, 128, 2339

[92] Oort, J. H., & Spitzer, L. J. 1955, ApJ, 121, 6

[93] Osterbrock, D. E. 1974, *Astrophysics of gaseous nebulae* (W. H. Freeman and Co., San Francisco)

[94] Palla, F., & Stahler, S. W. 1999, ApJ, 525, 772

[95] Peters, T., Banerjee, R., & Klessen, R. S. 2008, Phys.Scr., T132, 014026

[96] Price, D. J., & Monaghan, J. J. 2004, MNRAS, 348, 139

[97] Price, D. 2005, arXiv:astro-ph/0507472

[98] Price, D. J. 2007, Publications of the Astronomical Society of Australia, 24, 159

[99] Price, D. J. 2008, JCompPhys, 227, 10040

[100] Salmon, J. K., Warren, M. S. & Winckelmans, G. S. 1994, Intl. J. Supercomputer Appl., 8, 129

[101] Salpeter, E. E. 1971, ARA&A, 9, 127

[102] Sandford, M. T., II, Whitaker, R. W., & Klein, R. I. 1982, ApJ, 260, 183

[103] Schoenberner, D. 1981, A&A, 103, 119

[104] Shu, F. H. 1992, Physics of Astrophysics, Vol. II, by Frank H. Shu. Published by University Science Books, ISBN 0-935702-65-2, 476pp, 1992.,

[105] Spitzer, L. 1978, *Physical Processes in the Interstellar Medium* (New York: Wiley-Interscience)

[106] Springel, V., Yoshida, N., & White, S. D. M. 2001, New Astronomy, 6, 79

[107] Stahler, S. W., & Palla, F. 2005, The Formation of Stars, by Steven W. Stahler, Francesco Palla, pp. 865. ISBN 3-527-40559-3. Wiley-VCH , January 2005.,

[108] Strømgren, B. 1939, ApJ, 89, 526

[109] Sugitani, K., Tamura, M., & Ogura, K. 1999, Star Formation 1999, Proceedings of Star Formation 1999, held in Nagoya, Japan, June 21 - 25, 1999, Editor: T. Nakamoto, Nobeyama Radio Observatory, p. 358-364, 358

[110] Sugitani, K., Matsuo, H., Nakano, M., Tamura, M., & Ogura, K. 2000, AJ, 119, 323

[111] Thomas, P. A., & Couchman, H. M. P. 1992, MNRAS, 257, 11

[112] Vishniac, E. T. 1983, ApJ, 274, 152

[113] Weiler, K. W., & Sramek, R. A. 1988, ARA&A, 26, 295

[114] Whitworth, A. P., Bhattal, A. S., Chapman, S. J., Disney, M. J., & Turner, J. A. 1994, A&A, 290, 421

[115] Whitworth, A. P., Bhattal, A. S., Chapman, S. J., Disney, M. J., & Turner, J. A. 1994, MNRAS, 268, 291

[116] Whitworth, A. P., 2000, Private communication

[117] Whitworth, A. P., & Francis, N. 2002, MNRAS, 329, 641

[118] Whitworth, A. P., & Zinnecker, H. 2004, A&A, 427, 299

[119] Zavagno, A., Pomarès, M., Deharveng, L., Hosokawa, T., Russeil, D., & Caplan, J. 2007, A&A, 472, 835